

THESIS FOR THE DEGREE OF LICENTITATE OF ENGINEERING

Analysis of High-Frequency Electrical Transients in Offshore Wind Parks

TARIK ABDULAHović



Department of Energy and Environment
Division of Electric Power Engineering
CHALMERS UNIVERSITY OF TECHNOLOGY
Göteborg, Sweden 2009

Analysis of High-Frequency Electrical Transients in Offshore Wind Parks
TARIK ABDULAHOVIC

©TARIK ABDULAHOVIC, 2009

Licentiate Thesis at the Chalmers University of Technology

Department of Energy and Environment
Division of Electric Power Engineering
SE-412 96 Göteborg
Sweden
Telephone +46(0)31-772 1000

Chalmers Bibliotek, Reproservice
Göteborg, Sweden 2009

Abstract

In this thesis, a study of high frequency electromagnetic transient phenomena is performed. Models of various components needed for simulations of high frequency transients, such as transformers, cables and breakers are developed. Also, measurements of high frequency transients are performed in the cable laboratory in ABB Corporate Research in Västerås, Sweden for the purpose of parameter estimation of models and for verification of simulations. Some critical cases where the voltage surges of the magnitude and/or rise time above basic lightning impulse voltage level appear, are identified. Also, some transient protection schemes are analyzed and the performance of different transient mitigation devices is studied. Furthermore, the energizing transient of the Utgrunden wind park is analyzed and the simulation model is verified using the measurements.

The energizing transient simulation predicted accurately the magnitude and the frequency of the transient voltages and currents. Simulations of the high frequency transients are in a very good agreement with the measurements obtained in the cable lab. Simulations predicted accurately critical surges with the highest magnitude and matched with good accuracy surge waveform recorded during the measurements. During the testing and simulations, surges which exceed the basic lightning impulse voltage level of dry-type transformers specified by IEEE standards, both in magnitude and rise time are observed even when surge arresters are used. It is confirmed both in simulations and measurements that use of additional transient protections devices such as surge capacitors and RC protection, decreased the magnitude of surges below the critical level.

Index Terms: very fast transient, breaker, surge, surge protection, transient overvoltage, prestrikes, restrikes, voltage escalation.

Acknowledgements

This work has been carried out at the Division of Electric Power Engineering, Department of Energy and Environment at Chalmers University of Technology, Göteborg, Sweden and ABB Corporate Research, Västerås, Sweden. The financial support provided by Vindforsk, for the last two and half years, is gratefully acknowledged.

I would like to thank my supervisors Professor Torbjörn Thiringer and Docent Ola Carlson for their patience, encouraging, stimulating and critical comments regarding the work, and revising the thesis manuscript extensively to give it a better shape. In addition, I acknowledge support from my examiner Tore Undeland.

I express my sincere appreciation to Ambra Sannino and Lars Gertmar from ABB Corporate Research, Michael Lindgren and David Söderberg from Vattenfall, Sture Lindahl and Andreas Petersson from Gothia Power, Professor Stanislaw Gubanski from Chalmers and Philip Kjaer from Vestas for constructive discussions and suggestions during the reference group meetings.

I acknowledge the support from my dear colleagues at the division. I also acknowledge the support from Yuriy for Comsol simulations.

I would like to thank colleagues from ABB Corporate Research in Västerås, Lars Liljestrand, Henrik Breder, Dierk Bormann and especially Muhamad Reza for their support and very nice discussions.

Last, but certainly not least, heartfelt thanks go to my parents Agan and Zejna, brother Zijad, wife Esmeralda and my daughter Merjem for their kindness, love, support and patience.

*Tarik,
Göteborg,
April, 2009*

Contents

1	Introduction	1
1.1	Problem Overview	1
1.2	Aim/purpose	2
1.3	Thesis structure	3
2	Background Theory on Surge Propagation	4
2.1	Electromagnetic Wave Traveling and Reflection	4
2.2	Surge propagation	9
3	Modeling in PSCAD/EMTDC	11
3.1	Vacuum Circuit Breaker Modeling	11
3.1.1	Current chopping	12
3.1.2	Dielectric withstand and current quenching capability	14
3.1.3	Multiple reignitions and voltage escalation	18
3.1.4	Prestrikes	20
3.2	Modeling of Underground Cables	23
3.2.1	Cable Modeling in PSCAD/EMTDC	27
3.3	Transformer Modeling	32
3.3.1	Transformer Modeling for Low Frequency Transient Analysis	33
3.3.2	Transformer Modeling for High Frequency Transient Analysis	36
4	Practical Case Studies	38
4.1	Utgrunden Wind Park Cable Energizing	38
4.1.1	Resonance in the Utgrunden wind park	40

4.1.2	Measurements and analysis of cable energizing in Utgrunden	40
4.2	The Cable Lab	47
4.2.1	Layout of the Three Phase Test Setup	47
4.2.2	Measurement Setup	49
4.2.3	Measurement Results and Analysis	50
5	Conclusions and Future Work	97
5.1	Conclusions	97
5.2	Future Work	98

Chapter 1

Introduction

1.1 Problem Overview

For many years, the lightning was the only phenomenon that could create pulses with very steep fronts in order of micro seconds (μs). These wave pulses can be reflected from junctions in the system producing high overvoltages. High overvoltages produced by lightning are prevented from damaging insulation of the equipment by using surge arresters that are able to keep the voltage limited within the range that is not harmful to the protected equipment. This protection proved to be sufficient for the protection of the equipment and the failures were kept on an acceptable level.

Further research in this area was not needed until increased failures of the insulation of the equipment were detected again even on the low voltage level. These failures occurred more and more often with the development and improvements of the equipment used in electric power, especially in motor drives. Two areas of the development are very important for this matter.

One of them is the development of semiconductors used in power electronics. The appearance of the fast switching insulated gate bipolar transistors (IGBT's) led to very short rise times of the pulses that were produced by IGBT's in pulse-width modulated (PWM) inverters that are often used with induction machines (IM) for variable speed drives. The rise time of the pulses could be as low as or even below $0.1 \mu s$ [1]. This is more than ten times quicker compared to the rise time of the lightning pulse. These fast switching IGBT's brought two major improvements to the inverters. At first, lower switching losses and secondly reducing the total harmonic distortion (THD) given a similar filter.

Another one is the development of the breakers used in the electric grid. Breakers used in grids can have a strong negative influence on insulation. The appearance of the vacuum circuit breaker (VCB) brought a switching device with excellent interruption and dielectric recovery characteristics [2]. Vacuum circuit breakers have low maintenance costs, good durability and provide the best breaker solution for medium voltage below $24 kV$ [3]. However, it was reported worldwide that many transformer insulation failures have occurred possibly by switching operations of VCBs, although those transformers have previously passed all the standard tests and complied to all quality requirements [4]-[5]. However, another study showed that it is not only the vacuum breaker that can create surges potentially dangerous

to the transformers, but also SF6 insulated breakers and disconnectors [6]. The breakdown in SF6 medium can have a typical rise time between $2 - 20ns$ and SF6 interrupters and re-strikes and pre-strikes can be generated during operation [6]. A 10 years long study which included investigation of failures of thousands of the transformers conducted by Hartford Steam Boiler Earlier shows that the high frequency transients are the major cause of the transformer failure [7]. The transformer failures caused by the high frequency transients reaches the level of 33.9% according to this study and it is the most likely cause of the transformer insulation failure [7]. Although, the direct proof of the negative impact of the high frequency transients on the transformer insulation is not yet found [6], some studies give description of the phenomenon that produces high overvoltages internally in the transformer winding [8] potentially responsible for the transformer insulation failure during the high frequency transients. A problem of the transformer insulation failure developed also in the wind parks(WP) Middelgrunden and Hornsrev where almost all transformers had to be replaced with new ones due to the insulation failure [9], [10]. It is suspected that the fast switching breakers caused the insulation failures in these WP's.

During studies of the insulation failures of the motors caused by the switching phenomenon, it is found that the surges generated during switching of the air magnetic circuit breakers are very similar to the vacuum devices [11]-[13]. According to one of these studies, surges generated by air magnetic circuit breakers generated surges $4.4pu$ in magnitude with the rise times of $0.2\mu s$ where the vacuum breaker generated surges with $4.6pu$ in magnitude but with longer rise times of $0.6\mu s$ [11]. An important finding of this study is that although the vacuum breaker generates more surges, the magnitude and the rise time of the surges generated by these two types of breakers are very similar [11].

Another factor that contributed to the failures caused by the fast switching operations of the IGBT's and VCB's is the use of the cables both in low and medium voltage systems. The characteristic impedance of the cables is approximately ten times smaller than the characteristic impedance of a transmission line resulting in ten times higher derivative of the transient overvoltage (TOV). The transient phenomenon is thus even more difficult to analyze since cables longer than approximately $50 m$ behave like transmission lines where the wave traveling phenomenon and the wave reflection phenomenon can be observed. This means that a proper high frequency transient analysis advanced cable model is required, which makes the transient phenomenon analysis fairly complicated. In order to perform calculations of the propagation of high frequency transients an appropriate modeling and an appropriate software tool is needed

1.2 Aim/purpose

The aim of this thesis is to analyze the generation and the propagation of high frequency transients in the wind parks (WP's) and to present analysis as well as key results. In order to successfully achieve this goal the modelling of the important components as well as their implementation is to be investigated. The treated components will be:

- Circuit breaker
- Cable

- Transformer.

The best way of carrying out such an analysis of the high frequency transients is to use the computer aided design (CAD) software like PSCAD/EMTDC. PSCAD/EMTDC is one of the most widely used software for power system simulations. It has a good base structure, a large model library and also the capability to run simulations of the power systems using a very small time step which makes it suitable for high frequency transient analysis. Furthermore, during this study the measurements of the voltages and currents at critical points in the system and the verification of the model developed in PSCAD/EMTDC are conducted.

The goal is to identify cases in which the transient voltages with its rise time and magnitude exceed the basic lightning impulse voltage level (BIL) for the transformer used in the test. Moreover, the generation of multiple pre-strikes and re-strikes is studied and analyzed. As some studies for induction motors showed, the appearance of repetitive strikes is dangerous for the induction motors [14],[15] and is of the highest interest to identify when and under which conditions the repetitive strikes are generated in the system.

Furthermore, this study includes analysis of high frequency transients when the transient protection devices are used to protect the critical apparatus. The impact of the protection devices on the magnitude and the rise time of the voltage surges is observed.

1.3 Thesis structure

The structure of the thesis is the following:

Chapter 2 - Background Theory on Surge Propagation

Chapter 3 - Modeling in PSCAD/EMTDC

Chapter 4 - Practical Case Studies

Chapter 5 - Conclusions and Future Work.

Chapter 2

Background Theory on Surge Propagation

The phenomena of traveling waves on long transmission lines and cables is known since a long time. The waves that travel over the conductor at the speed of light are transverse waves, and the behavior of these waves is the same as the behavior of other transverse waves. Reflection of the waves we experience in everyday's life when we hear echo or look to the reflection in the mirrors or on the surface of water. The same phenomena occurs at the end of the transmission lines or cables and can produce very high overvoltages at transmission line or cable ends in some cases.

2.1 Electromagnetic Wave Traveling and Reflection

Transverse electromagnetic waves are mathematically described by Maxwell's equations in the 19th century. These equations describes the dynamical properties of the electromagnetic field. These equations are based on experimental results and are written in the following form

$$\nabla \cdot \mathbf{E} = -\frac{\rho(t, x)}{\varepsilon} \quad (2.1)$$

$$\nabla \times \mathbf{E} = -\frac{\partial \mathbf{B}}{\partial t} \quad (2.2)$$

$$\nabla \cdot \mathbf{B} = 0 \quad (2.3)$$

$$\nabla \times \mathbf{B} = \mu \mathbf{j}(t, x) + \varepsilon \mu \frac{\partial \mathbf{E}}{\partial t} \quad (2.4)$$

where \mathbf{E} is the vector of electric field, \mathbf{B} is the magnetic flux density, $\rho(t, x)$ is the charge distribution, $\mathbf{j}(t, x)$ is the magnetic current density, μ is the permeability and ε permittivity

of the material.

These four non-coupled partial differential equations, can be rewritten as two non-coupled second order partial equations for \mathbf{E} and \mathbf{D} . These two equations are called the wave equations. Let us start deriving the wave equation for \mathbf{E} . Since the waves propagating in air or vacuum are considered, these equations are derived using vacuum permeability and permittivity μ_0 and ε_0 . First, let us take the curl of (2.2) and then insert (2.4) to obtain

$$\nabla \times (\nabla \times \mathbf{E}) = -\frac{\partial}{\partial t}(\nabla \times \mathbf{B}) = -\mu_0 \frac{\partial}{\partial t}(\mathbf{j}(t, x) + \varepsilon_0 \frac{\partial \mathbf{E}}{\partial t}). \quad (2.5)$$

To solve this, we are going to use the operator triple product "bac-cab" rule given by

$$\nabla \times (\nabla \times \mathbf{E}) = \nabla(\nabla \cdot \mathbf{E}) - (\nabla^2 \mathbf{E}). \quad (2.6)$$

Furthermore, the electrical charges are not present $\rho(t, x) = 0$ in the medium yielding a simplified form of (2.1)

$$\nabla \cdot \mathbf{E} = 0. \quad (2.7)$$

Considering (2.6) and (2.7), and taking into account Ohm's law given by

$$\mathbf{j}(t, x) = \sigma \mathbf{E} \quad (2.8)$$

(2.5) is rearranged and written in the form of

$$\nabla^2 \mathbf{E} - \mu_0 \frac{\partial}{\partial t} \left(\sigma \mathbf{E} + \varepsilon_0 \frac{\partial \mathbf{E}}{\partial t} \right) = 0. \quad (2.9)$$

Finally, taking into account

$$\varepsilon_0 \mu_0 = \frac{1}{c^2} \quad (2.10)$$

where c is the speed of light, the homogeneous wave equation for \mathbf{E} is obtained

$$\nabla^2 \mathbf{E} - \mu_0 \sigma \frac{\partial \mathbf{E}}{\partial t} - \frac{1}{c^2} \frac{\partial^2 \mathbf{E}}{\partial t^2} = 0. \quad (2.11)$$

In a similar fashion, the homogeneous wave equation for \mathbf{B} is derived. This equation is given by

$$\nabla^2 \mathbf{B} - \mu_0 \frac{\partial}{\partial t} \left(\sigma \mathbf{B} + \varepsilon_0 \frac{\partial \mathbf{B}}{\partial t} \right) = 0. \quad (2.12)$$

Inserting the relation for the speed of light into (2.12), the homogeneous wave equation for \mathbf{B} is obtained.

$$\nabla^2 \mathbf{B} - \mu_0 \sigma \frac{\partial \mathbf{B}}{\partial t} - \frac{1}{c^2} \frac{\partial^2 \mathbf{B}}{\partial t^2} = 0. \quad (2.13)$$

For a plane wave where both electric and magnetic field depends on the distance x to a given plane, the wave equations for \mathbf{E} and \mathbf{B} are given by

$$\frac{\partial^2 \mathbf{E}}{\partial^2 x} - \mu_0 \sigma \frac{\partial \mathbf{E}}{\partial t} - \frac{1}{c^2} \frac{\partial^2 \mathbf{E}}{\partial t^2} = 0 \quad (2.14)$$

$$\frac{\partial^2 \mathbf{B}}{\partial^2 x} - \mu_0 \sigma \frac{\partial \mathbf{B}}{\partial t} - \frac{1}{c^2} \frac{\partial^2 \mathbf{B}}{\partial t^2} = 0. \quad (2.15)$$

These equations that describe the propagation of the plane waves in a conducting medium are called the telegrapher's equations or the telegraph equations. For insulators, where the conductivity is equal to zero ($\sigma = 0$), the telegrapher's equations become

$$\frac{\partial^2 \mathbf{E}}{\partial^2 x} - \frac{1}{c^2} \frac{\partial^2 \mathbf{E}}{\partial t^2} = 0 \quad (2.16)$$

$$\frac{\partial^2 \mathbf{B}}{\partial^2 x} - \frac{1}{c^2} \frac{\partial^2 \mathbf{B}}{\partial t^2} = 0. \quad (2.17)$$

In electrical engineering it is more common to write equations using voltages and currents, and inductances and capacitances instead. A more convenient way to write and derive the telegrapher's equations is by using an equivalent scheme for two parallel conductors. The equivalent scheme is defined for an infinitely small element of two conductors and it is presented in Fig.2.1

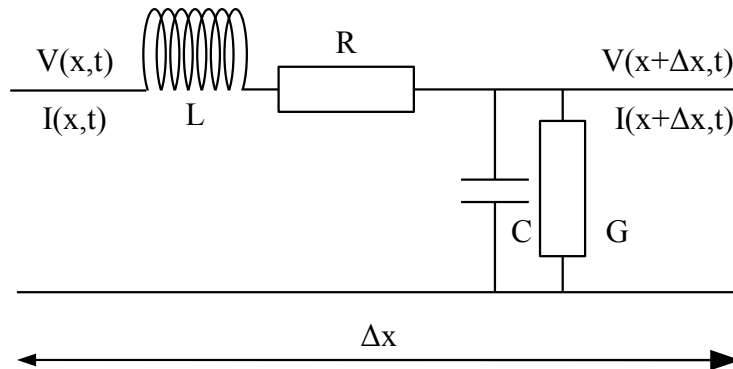


Figure 2.1: An infinitely small element of two parallel conductors.

For the sake of simplicity a somewhat simpler equivalent scheme where the resistance of the conductor and the conductance between the two lines is neglected is presented in Fig.2.2

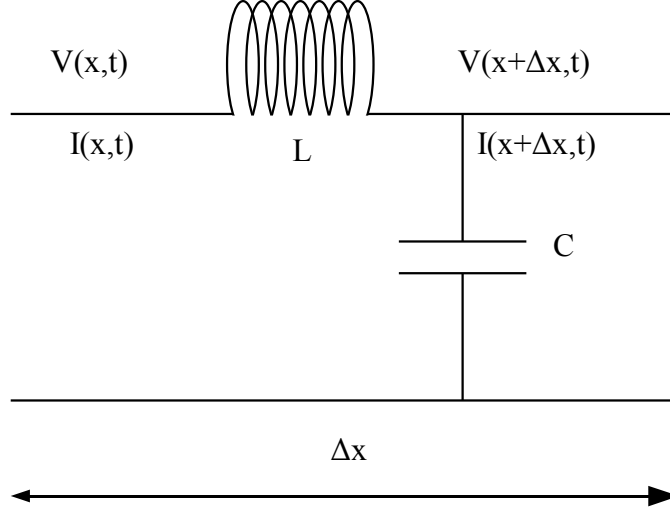


Figure 2.2: An infinitely small element of two parallel conductors.

For this circuit it is quite easy to derive the telegraphers equations using Kirchoff's Laws. Since the capacitance and the inductance presented in Figs. 2.1 and 2.2 are per unit length, values of the capacitance and inductance are obtained after multiplication by Δx . For the voltage and the current at length of $x + \Delta x$, two equations can be written as

$$V(x + \Delta x, t) = V(x, t) - C\Delta x \frac{\partial I(x, t)}{\partial t} \quad (2.18)$$

$$I(x + \Delta x, t) = I(x, t) - L\Delta x \frac{\partial V(x + \Delta x, t)}{\partial t}. \quad (2.19)$$

These two equations can be rewritten in the following way

$$\frac{V(x + \Delta x, t) - V(x, t)}{\Delta x} = -C \frac{\partial I(x, t)}{\partial t} \quad (2.20)$$

$$\frac{I(x + \Delta x, t) - I(x, t)}{\Delta x} = -L \frac{\partial V(x + \Delta x, t)}{\partial t}. \quad (2.21)$$

We take the limit as $\Delta x \rightarrow 0$ which yields $V(x + \Delta x, t) \rightarrow V(x, t)$ giving simplified telegrapher's equations for transmission lines

$$\frac{\partial V(x, t)}{\partial x} = -C \frac{\partial I(x, t)}{\partial t} \quad (2.22)$$

$$\frac{\partial I(x, t)}{\partial x} = -L \frac{\partial V(x, t)}{\partial t}. \quad (2.23)$$

These equations can be solved by taking the spatial derivative of one equation and substituting the other equation into it. Let us do it first by taking the spatial derivative of (2.22).

$$\frac{\partial^2 V(x, t)}{\partial x^2} = -C \frac{\partial^2 I(x, t)}{\partial t \partial x} \quad (2.24)$$

Substituting (2.23) into (2.24) the telegrapher equation for voltage is obtained.

$$\frac{\partial^2 V(x, t)}{\partial x^2} = LC \frac{\partial^2 V(x, t)}{\partial t^2} \quad (2.25)$$

In the same manner, the current equation is derived.

$$\frac{\partial^2 I(x, t)}{\partial x^2} = LC \frac{\partial^2 I(x, t)}{\partial t^2} \quad (2.26)$$

(2.25) and (2.26) just represent (2.16) and (2.17) in a rewritten form. The voltage corresponds to the electric field and the current corresponds to the magnetic field. Now, let us solve the voltage equation while the other equations are solved in a similar fashion. At the start of the process we are going to make a guess and write solution as

$$V(x, t) = V_0 f(x - vt) \quad (2.27)$$

where V_0 is the amplitude of the wave and $f(x - vt)$ is yet unidentified function which describes the behavior of the wave during time t along the propagation axis x . The first time derivative of this function is

$$\frac{\partial}{\partial t} f(x - vt) = -(vf'). \quad (2.28)$$

The second time derivative and second space derivative are written as

$$\frac{\partial^2}{\partial t^2} f(x - vt) = v^2 f'' \quad (2.29)$$

$$\frac{\partial^2}{\partial x^2} f(x - vt) = f''. \quad (2.30)$$

Substituting (2.28), (2.29) and (2.30) into (2.25) we can write

$$V_0 f'' = LCV_0 v^2 f'' \quad (2.31)$$

which is true only as long as

$$v = \pm \frac{1}{\sqrt{LC}}. \quad (2.32)$$

So, it is defined for which value of parameter v this solution is valid, but still, the function $f(x - vt)$ remains unknown. Let us leave this aside at the moment and observe this function at two time instants t_1 and t_2 and two positions along the axis x . At the position x_1 and time instant t_1 , the voltage will have a value of $V_1 = V_0 f(x_1 - vt_1)$. After time Δt , the position x_2 is reached. Since a lossless propagation is observed, the value of the voltage $V_2 = V_0 f(x_2 - vt_2)$ is equal to the voltage in the initial point $V_2 = V_1$. This means that the arguments are the same

$$x_1 - vt_1 = x_2 - vt_2. \quad (2.33)$$

From (2.33) we find that v represents the speed of propagating waves by solving (2.33) for v

$$\frac{x_2 - x_1}{t_2 - t_1} = \frac{\Delta x}{\Delta t} = v = \frac{1}{\sqrt{LC}}. \quad (2.34)$$

Since the solution for the telegrapher's equations is valid for two opposite values of the speed according to (2.32), two waves propagating in opposite direction exists and are given by

$$V_{pos} = V^+ f\left(x - \frac{1}{\sqrt{LC}}t\right). \quad (2.35)$$

$$V_{neg} = V^- f\left(x + \frac{1}{\sqrt{LC}}t\right). \quad (2.36)$$

2.2 Surge propagation

The surge characteristics is mainly determined by the characteristic or the surge impedance of the transmission line or cable,

$$Z_0 = \sqrt{\frac{L}{C}}. \quad (2.37)$$

The capacitance and the inductance of the cable and the transmission line differ a lot due to the differences in the geometry of the cables and the transmission lines. For the transmission lines the value of the characteristic impedance is approximately about $Z_0=400 \Omega$. For the cables this value is about ten times smaller and has the value of $Z_0=40 \Omega$.

The differences in geometries lead to a difference in the wave velocities that the wave propagates through the cable and through the transmission line.

$$v_0 = \frac{1}{\sqrt{LC}} \quad (2.38)$$

The other important characteristic of the cable is that the velocity of the wave that propagates through the cable is approximately one half to two thirds of the propagation velocity of the wave that propagates through the transmission line and varies from $v_0 = 1.5 \times 10^8 \text{ km/s}$ to $v_0 = 2 \times 10^8 \text{ km/s}$.

These characteristics strongly influence the surge that appears in the cable systems. If the system consisting of a cable and a transformer is observed, a good approximation of the system for the prediction of high frequency transients have to have stray capacitances added to the the transformer. An example of such a system is shown in Fig. 2.3

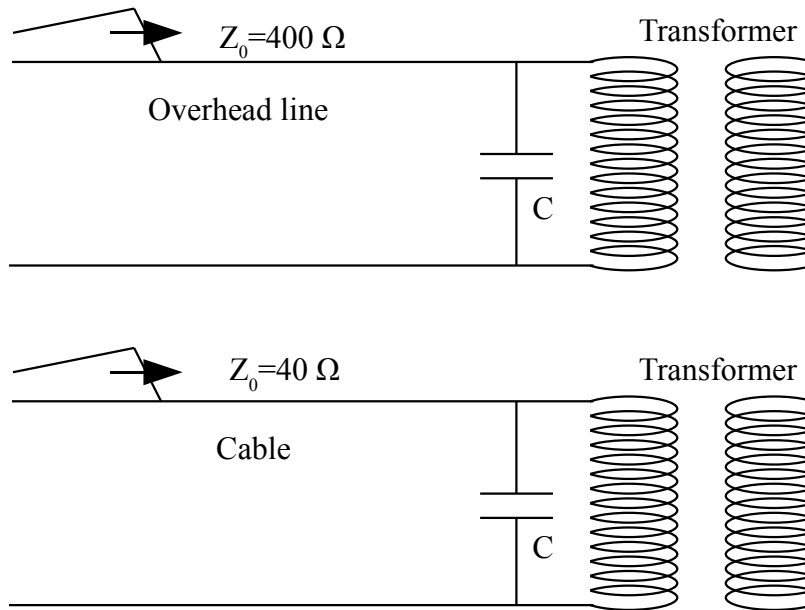


Figure 2.3: Simple system consisting of one cable and one transformer.

For the high frequency transient analysis this system can be represented as a first order system neglecting the inductance of the transformer which is very large, meaning that its time constant is a couple of orders of magnitude slower than the time constant of the cable and the stray capacitance.

The time constant of the approximated first order system can be determined as

$$\tau = \sqrt{\frac{L}{C}} C_{stray} = Z_0 C_{stray}. \quad (2.39)$$

Taking into account that the surge impedance of the cable Z_0 is ten times smaller than the surge impedance of an OH line leads to the consequence that the time constant of the cable also will be ten times quicker. This means that the surge created in the system will have ten times steeper front in the systems with the cables.

Chapter 3

Modeling in PSCAD/EMTDC

3.1 Vacuum Circuit Breaker Modeling

Vacuum and SF₆(sulfur-hexafluoride) are the most modern breaking techniques used in the circuit breakers for medium and high voltage applications. They appeared in the 1960's and quickly developed during the 1970's. The vacuum interrupters are primarily targeted for the medium voltages while the SF₆ interrupters are produced both for medium and high voltage [3].

The vacuum circuit breakers (VCB) have been intriguing the breaker designers primarily for it's advantages, which are:

1. it is completely self-contained, does not need any supply of gases or liquids, and emits no flame or smoke,
2. does not need maintenance, and in most applications its life time will be as long as the life-time of the other breakers,
3. it may be used in any orientation,
4. it is not flammable,
5. it has very high interrupting ability and does not need low ohmic resistors or capacitors to interrupt short-circuit currents,
6. it requires small mechanical energy for operation,
7. it is silent in operation.

These advantages of the vacuum breaking technique have been the main driving force of the VCB development. One of the early main disadvantages of the VCB was it's price. However, during 1970's the price was in the VCB favor comparing the price of the conventional and the vacuum interrupter [17].

Nowadays, with the environmental issues becoming more and more of a concern, the vacuum breaking technique is bringing another advantage into focus. Studies show that the

VCBs offer the lowest environmental impact of all medium voltage switching technologies over the entire product life cycle. The materials used in the VCBs are safe to handle during periodic out-of-service maintenance and at end-of-life disposal. It's main competitor in the medium voltage level, the SF6 technology is an extremely potent greenhouse gas. In addition, SF6 arc by-products are harmful and possess significant health concerns for handling and disposal. Environmental concerns have led to an increase of the total cost of ownership (TCO) of the SF6 breakers increasing its cost for purchasing, usage and disposal [18].

Constant development of the vacuum technology, vacuum processing, contact materials and evolution of the VCB design led to the significant decrease of the VCB size over past years [19].

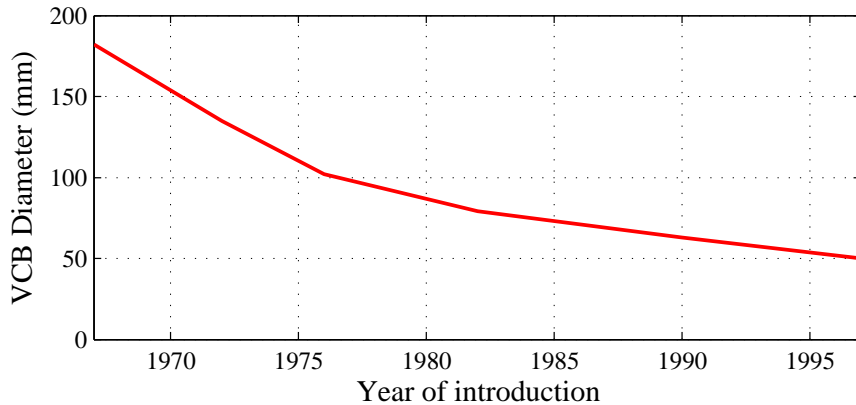


Figure 3.1: Size reduction of the 15(kV) 12(kA) vacuum interrupter 1967-1997

The vacuum breaking technique provides a very high interrupting ability and other favorable features that made it the number one choice for the medium voltage level switching apparatus. With the respect to the transient analysis in the system where the VCBs are used, it is of a substantial importance to understand the phenomenon of the arc breaking in the vacuum. In this thesis, only the phenomenon that can be "seen" from the outer system is going to be described, treating the VCB as a "black box". However, the phenomenon that leads to such a behavior of a VCB will be described in detail since the VCB itself is not in the main focus of this research. The main phenomenon in VCBs discussed in this thesis are:

- the current chopping,
- high-frequency current quenching,
- restrikes and the voltage escalation,
- prestrikes.

3.1.1 Current chopping

To explain the process during the opening of the contacts more detailed, some parameters of the VCB have to be introduced first. The transient voltage that appears over the VCB during an interruption is called the transient recovery voltage (TRV). The TRV is of high importance for the dielectric breakdown. The TRV is superimposed to the steady-state power

frequency voltage. Its peak value is related to the chopping current which is a parameter to the VCB's first reignition. The dielectric recovery of the VCB is another parameter of the VCB. This parameter depends on the contact separation velocity. When the contacts of the VCB are opening and the TRV starts to rise due to the current chopping, the TRV and the dielectric withstand of the VCB start to compete with each other. If the TRV reaches the value of the dielectric withstand of the gap between the contacts, the arc will be established again and the VCB will conduct the current. This underlines the importance of the dielectric recovery of the VCB. The time interval between the time instant of the contact opening and the power frequency current zero is called the arcing time (AT) or the arcing angle (AA) and is of substantial importance for the transient behavior of the VCB. When the arcing time is short, the dielectric withstand of the VCB is still very small. This means that the TRV will reach the dielectric withstand of the VCB very quickly and the VCB will lead the current again. Some of these parameters are going to be explained further in the thesis.

The current chopping is a phenomenon that can lead to severe overvoltages and occurs when small inductive and capacitive currents are switched. These overvoltages are produced when the current is interrupted before the power frequency current reaches zero. When conducting a small current, the arc in the vacuum is very unstable. This means that the arc will disappear before the current reaches its zero value. This has been considered as the major disadvantage of the vacuum breaking technique over the other breaking techniques. The current value when this happens is called the chopping current and the point when this happens is called the chopping level. These parameters of the VCB are shown in Fig. 3.2.

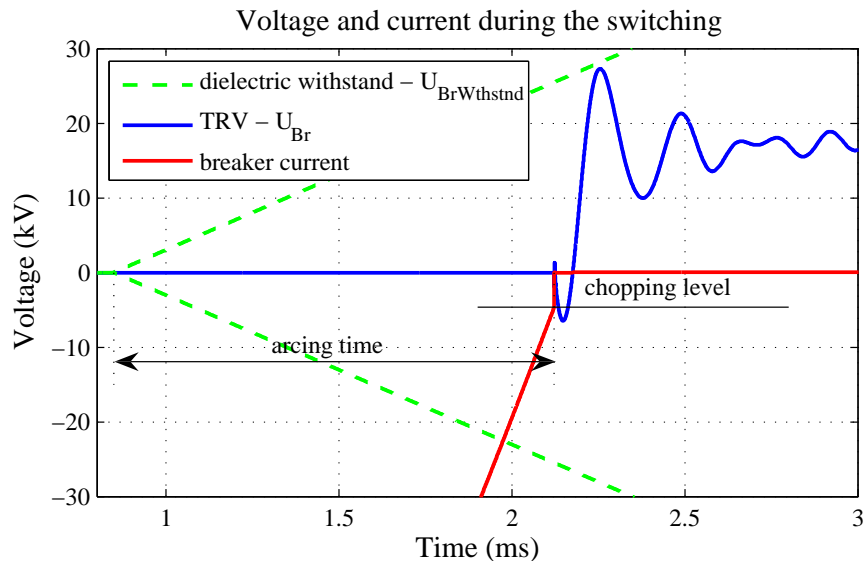


Figure 3.2: TRV, dielectric withstand, arcing time

The current declines with a very high di/dt when it is chopped. This means that a very high di/dt will produce very high overvoltage over the inductive load. The value of di/dt and the overvoltage itself is in direct proportion to the chopping current. During the very high load current (high RMS) this phenomenon does not exist. The reason for this is that due to the high current, the arc is not unstable any longer. The chopping level depends mainly on the choice of the contact materials and there has been a lot of researchers effort dedicated to reduce the chopping level by using proper materials for the contacts in VCB [20]. The chopping current is lower if the contacts open close to zero current [21]. The current chopping level is dependent on the load type and the surge impedance of the load

that is switched.

In order to obtain a mathematical description of the chopping current phenomenon, two different approaches can be taken. One of them is proposed by Reininghaus U. [22],

$$i_{ch} = a - b\hat{I} - c \log Z_N \quad (3.1)$$

where a , b and c are constants depending on the type of the material used for the contacts in the VCB and Z_N is the surge impedance of the circuit that is switched and \hat{I} is the magnitude of the load current that is switched.

The other method for current chopping level calculation is proposed by Smeets [23]. This method uses the formula

$$i_{ch} = (2\pi f \hat{I} \alpha \beta)^q \quad (3.2)$$

where f is the grid frequency, \hat{I} is the magnitude of the load current that is switched and α , β and q are the constants dependent on the contact materials. These constants which are available for the commercially available vacuum switchgear [24]:

$$\begin{aligned} \alpha &= 6.2 \times 10^{-16}(s), & \beta &= 14.2, \\ q &= -0.07512, & q &= (1 - \beta)^{-1} \end{aligned}$$

The current chopping level given by (3.2) varies between 3A and 8A. However, if the current at the power frequency is lower than the chopping level, the current is chopped immediately. Both approaches give the mean value of the chopping current which varies with the higher standard deviation compared to the breakers utilizing other breaking techniques.

3.1.2 Dielectric withstand and current quenching capability

As mentioned before in Section 3.1, the dielectric withstand of the breaker is a significant parameter for the switching analysis. This is the case especially when restrikes are studied. What happens during the beginning of the opening of the breaker is that the contacts start to separate. The withstand voltage of the gap is increasing proportionally to the square of the distance between the contacts [25], while for the first millimeter of the contact separation this dependence can be taken as linear. As the dielectric breakdown phenomenon is of a stochastic nature, for the very same VCB there will be some differences in the dielectric withstand. This difference varies with the normal distribution and a 15 % standard deviation can be assumed [24]. For an easier comparison of VCBs that have different dielectric withstand in theoretical analysis of the VCBs, only the mean value of the dielectric withstand is taken into account.

For the transient analysis the dielectric withstand is approximated using

$$\bar{U}_b = A_A(t - t_0) + B_B. \quad (3.3)$$

The constant A_A determines the slope, or the velocity of the contacts separation. It is the measure of the rate of recovery of the dielectric strength (RRDS). When the contacts are closing A_A describes the rate of decay of dielectric strength (RDDS). The values of the constants A_A and B_B vary from for the different VCBs. In Table 3.1 the values of these constants are given [26](Glinkowski) for VCBs with different types of the dielectric withstand (DW).

Table 3.1: Dielectric withstand characteristics constants

DW type	$A_A(\text{V}/\mu\text{s})$	$B_B(\text{kV})$
High	17	3.4
Medium	13	0.69
Low	4.7	0.69

When the current chopping phenomenon was discussed, it was explained that it occurs for low currents at the power frequency. What about the high frequency (HF) currents that appear due to the energy oscillation in between the stray inductance/capacitance/resistance of the VCB? What is the capability of the VCB to switch such currents?

The frequency of the HF current is mainly determined by the stray parameters of the VCB and it does not change during the conducting state of the VCB. This HF current is superimposed to the power frequency current and the magnitude of the HF current is damped quite quickly. The VCB is not capable of breaking HF currents at the zero crossing if the di/dt value of the HF current is too high. However, as the magnitude of the HF current declines, the value of di/dt is also decreasing. After a certain number of current zero crossings the value of di/dt is small enough so the VCB can break the current, and that critical value of di/dt represents the quenching capability of the HF current. The method used in this thesis to determine the quenching capability of a VCB is given by M. Glinkowski [26]. This method proposes a linear equation, identical to one used to determine the dielectric withstand

$$\overline{di/dt} = C_C(t - t_0) + D_D. \quad (3.4)$$

This equation gives the mean value of the quenching capability which has a normal distribution with the same standard deviation as the dielectric withstand. In the theoretical analysis in this thesis only the mean value of the HF current quenching capability is taken into account. In Table 3.2 the values of the constants used in (3.4) are given [26].

Table 3.2: HF current quenching capability constants

DW type	$C_C(\text{A}/\mu\text{s}^2)$	$D_D(\text{A}/\mu\text{s})$
High	-0.034	255
Medium	0.31	155
Low	1	190

Some other authors suggest that the HF current quenching capability characteristics di/dt is constant [27]. The values suggested are $100 \text{ A}/\mu\text{s}$ and $600 \text{ A}/\mu\text{s}$. To analyze the transients during the VCB switching, a test circuit representing the grid, VCB, cable and the load shown in Fig.3.3 is used.

The behavior of the voltages and the currents during the VCB operation can be observed in Fig.3.4.

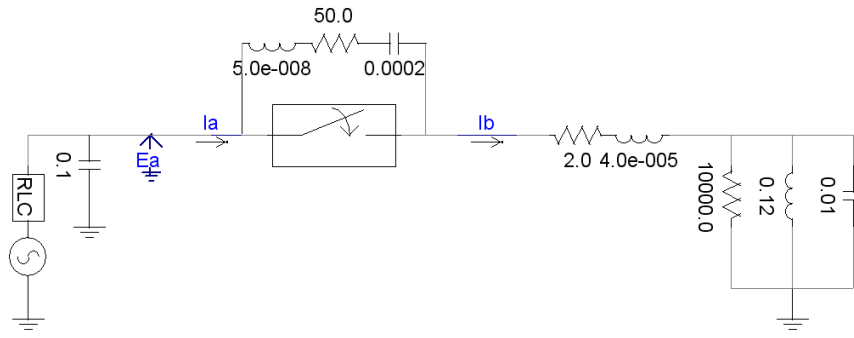


Figure 3.3: Single-phase test setup for reignition studies

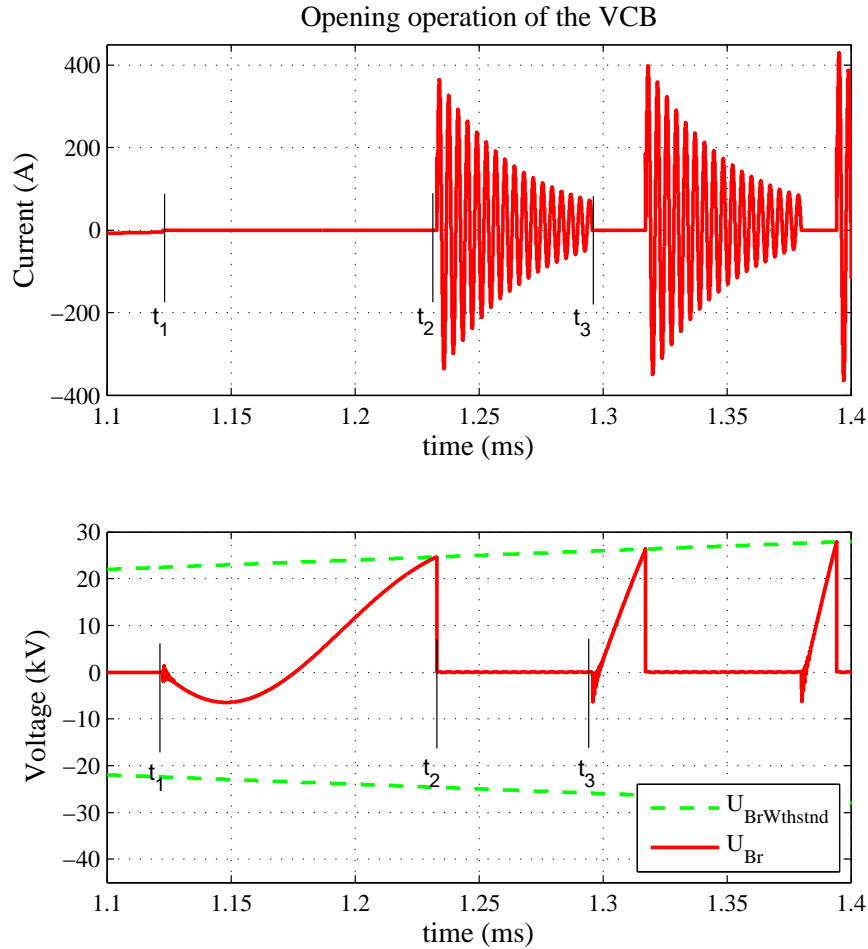


Figure 3.4: Current and voltage across VCB during switching

Before the time instant of t_1 , not all the conditions for the breaking of the arc in vacuum are reached. Although the dielectric withstand of the breaker is higher than the peak voltage of the tested system (13 kV RMS) the current is still higher than the chopping current. As the current reaches the chopping level at the instant of t_1 , the arc becomes unstable and the VCB breaks the current. The TRV starts building up very quickly and reaches the dielectric withstand of the VCB after approximately 150 μs at the time instant of t_2 . This leads to a voltage breakdown in the vacuum resulting in a HF current having a frequency determined by the stray parameters of the VCB. In the beginning of such a transient with such high initial voltage determined by the dielectric withstand, the HF current has a very

high magnitude. The VCB cannot interrupt this HF current at the zero crossing until it is damped enough. When the magnitude and di/dt of the HF current drops to the value matched by the quenching capability of the breaker, the VCB breaks the HF current and the TRV starts building up again. Next time the TRV reaches the dielectric withstand of the VCB at the time instant of t_3 , the VCB builds a higher dielectric withstand as a result of the further opening of the contacts. This means that the initial voltage for the HF current transient gets larger with the separation of the contacts. The resulting HF current is now even higher in magnitude and even more difficult to break. This process continues until the VCB achieves a successful interruption or until the VCB becomes unable to break the HF current, which is damped quickly only after $150 \mu s$, conducting only the power frequency current for the rest of the half-period. This process can be seen in Fig. 3.5

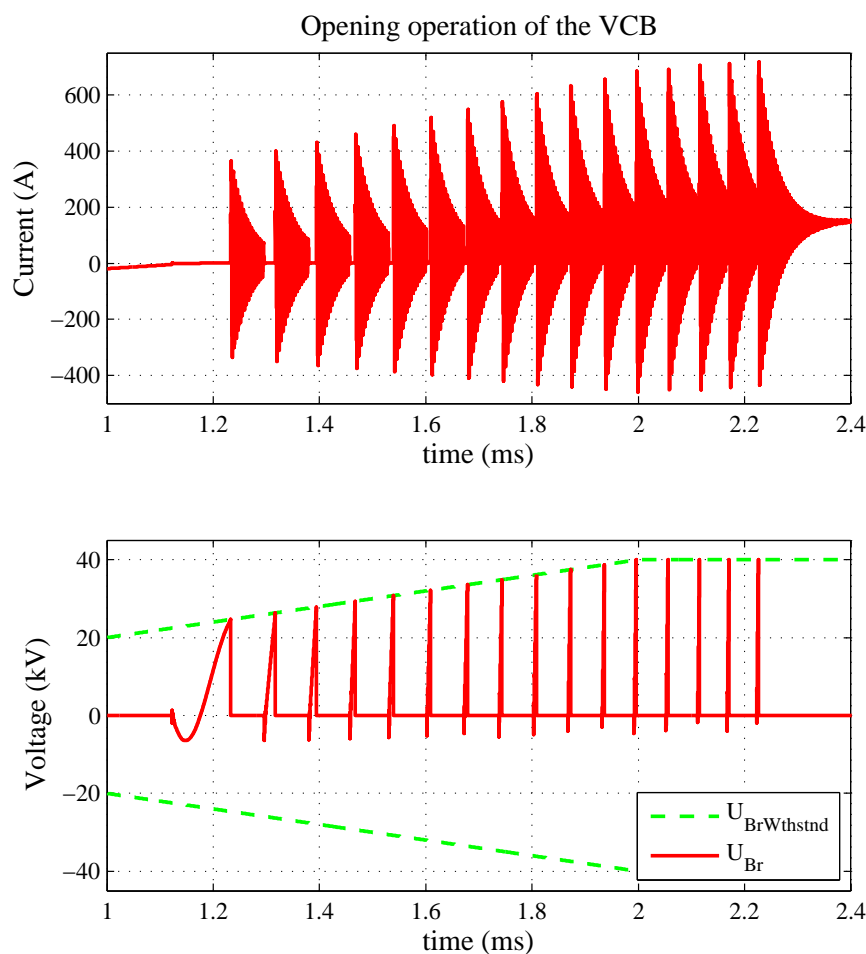


Figure 3.5: Unsuccessful interruption of the VCB

If a successful interruption is not achieved, the VCB "waits" for the power frequency current to reach the chopping level. If the current at the power frequency is too high, the VCB will break at the zero crossing. The dielectric withstand of the VCB is at its maximum when the conditions for the current breaking are reached at the second attempt to break the current. This means that the TRV that appears across the VCB is not able to reach the dielectric withstand anymore. Both attempts of the VCB to break the current are shown in Fig. 3.6

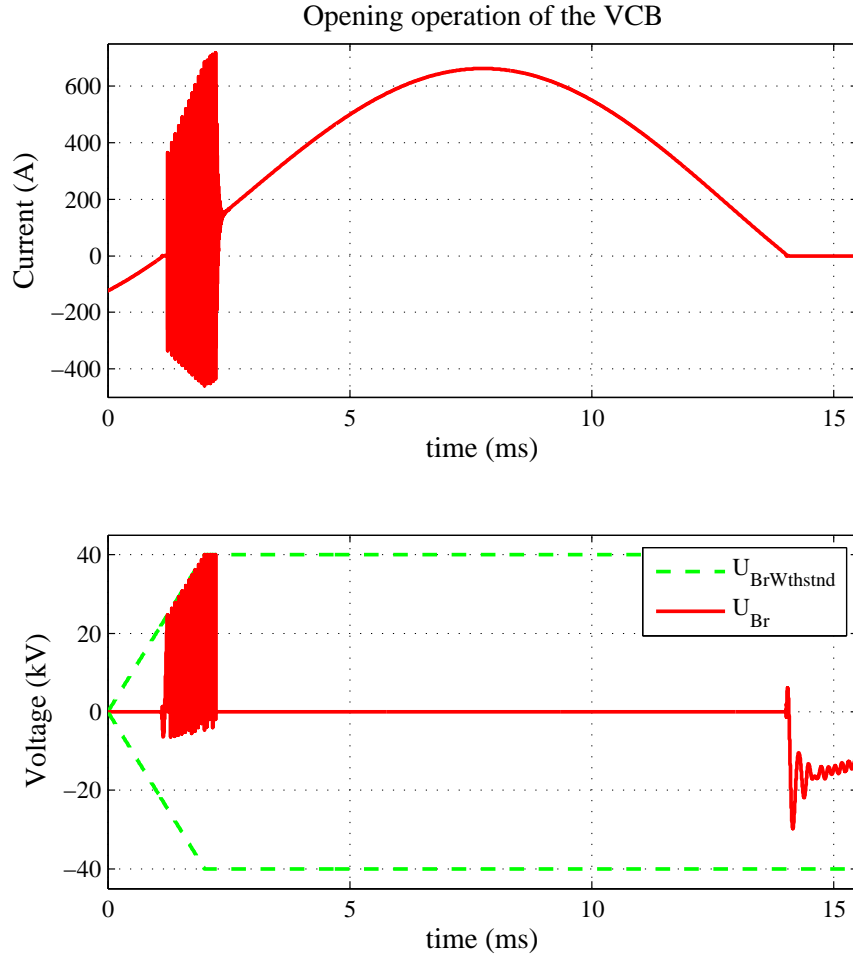


Figure 3.6: Unsuccessful and successful VCB operation

3.1.3 Multiple reignitions and voltage escalation

Reignitions and restrikes are temporary breakdowns of the vacuum dielectric. They appear when the VCB breaks the inductive and capacitive currents respectively. Reignition is a temporary voltage breakdown that occurs during the first quarter of the voltage period and restrike is the one that appears in the second quarter. Reignitions can be seen in Figs. 3.4 and 3.5. Reignitions and restrikes are caused by the fast rising TRV. The fast rise of the TRV is initiated by high di/dt that appears due to the current chopping. Due to the inductance present in the system, high di/dt produces an overvoltage that is proportional to the surge impedance of the switched object and the value of di/dt as explained before in Section 3.1.1. When the TRV reaches the dielectric withstand of the gap, the arc appears again, conducting the HF current superimposed to the power frequency current. Since the VCB is able to break the HF current, the TRV starts rising quickly as soon as the VCB breaks the HF current. The fast rising TRV reaches the dielectric withstand of the gap causing another reignition. This phenomenon is called multiple reignitions. From this description of the phenomenon of the multiple restrikes and reignitions it is easy to underline the importance of the following parameters of the VCB for the appearance of the multiple restrikes and reignitions:

- the arcing time (AT) or the arcing angle (AA),

- the dielectric withstand of the VCB and the RRDS
- the HF current quenching capability

The AT is a very important parameter for the multiple reignition behavior. A very short AT, shorter than $100 \mu s$, should be avoided [26]. If the AT is too short, the dielectric strength of the gap is not developed enough to withstand the TRV. For the VCBs that have very high RRDS, the dielectric strength recovers very fast, reducing the number of reignitions and helps to break the current.

The HF current quenching capability is very important for the number of reignitions that occur during the breaker opening. The VCB current for different VCBs with different HF quenching capability is presented in Fig. 3.7.

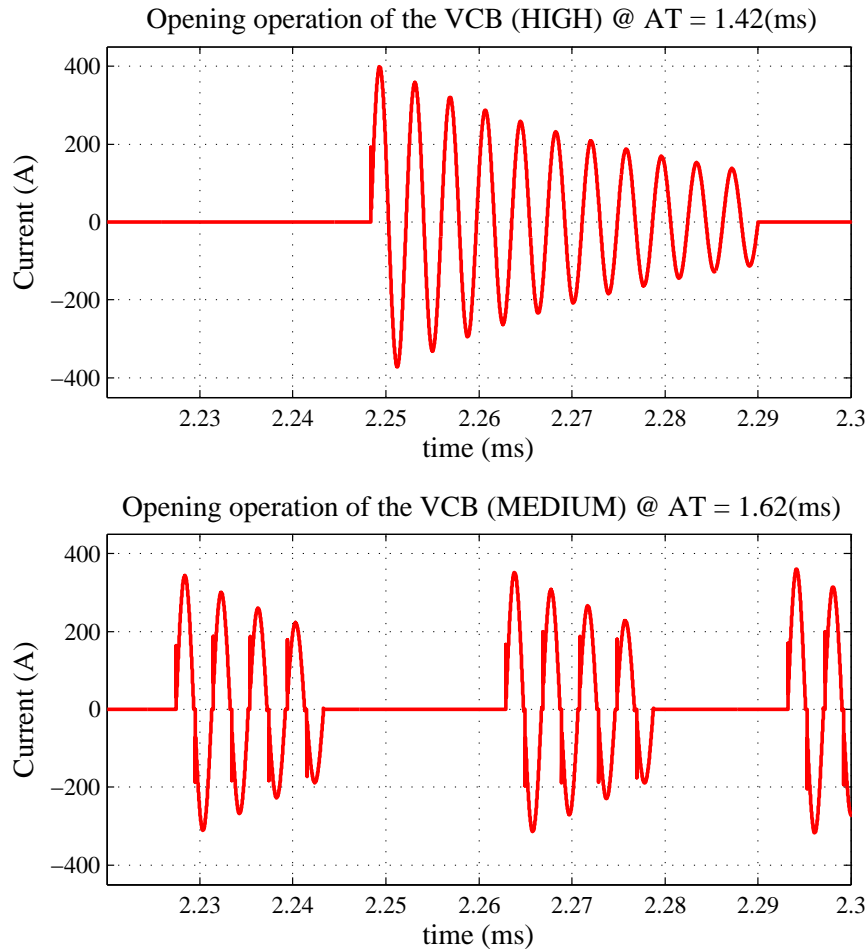


Figure 3.7: VCB current comparison for different interruption capabilities

From Fig. 3.7 it can be clearly seen that the VCB of the medium DW type is able to clear HF current of higher di/dt as the contacts separate compared to the high DW type. However, this leads to appearance of more reignitions, which can be seen in Fig. 3.8

More details can be seen in Fig. 3.9 where reignitions are shown in a shorter time scale.

From Fig. 3.9 it is clear that after each breaking of the HF current, for the VCB of the medium DW type, the TRV reaches the dielectric withstand of the VCB reigniting the HF current.

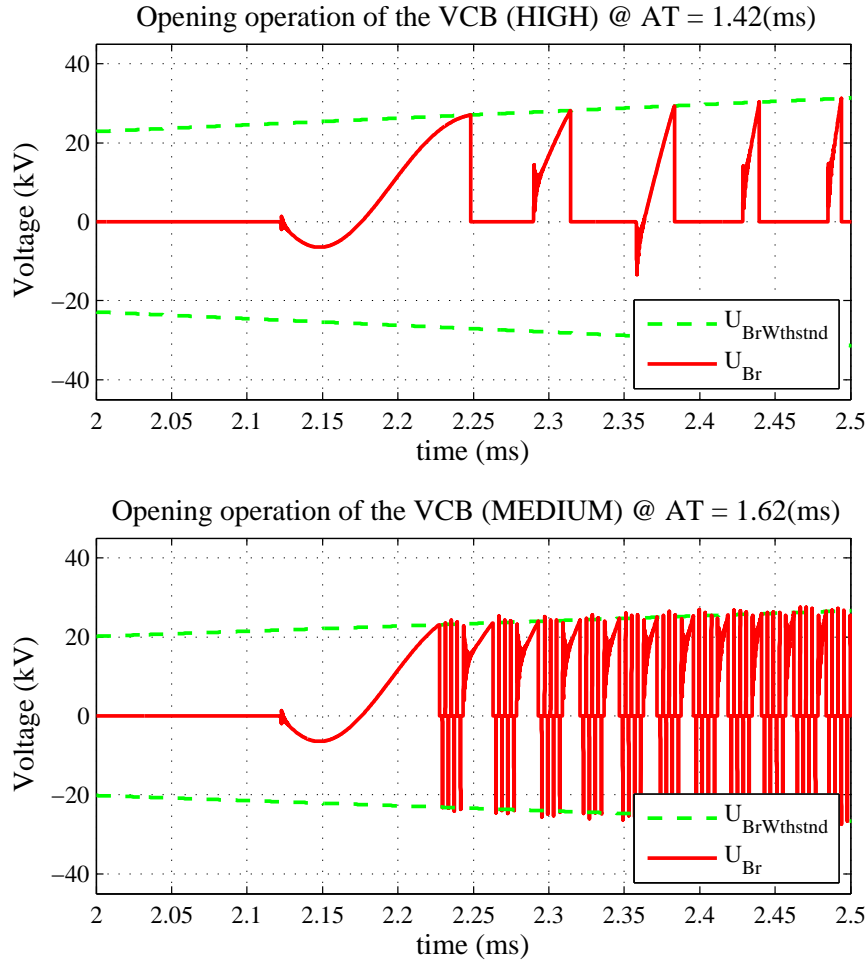


Figure 3.8: VCB voltage comparison for different interruption capabilities

Multiple reignitions can lead to a voltage escalation. Since the TRV superimposes to the steady-state 50/60 Hz voltage, when the current chopping occurs with the inductive current, the steady-state voltage is very close to its peak value resulting in a very high voltage on the terminals. With every subsequent breakdown, the voltage can be clamped on higher and higher values leading to the voltage escalation. This phenomenon can occur during the load shedding producing very high overvoltages [26]. To minimize the appearance of the voltage escalations very small AT (less than 100 μs should be avoided [26].

3.1.4 Prestrikes

Prestrikes are as well as restrikes and reignitions a temporary breakdown of the vacuum dielectric. The phenomenon of multiple prestrikes and the prestrike voltages occur during the closing operation of the VCB when the energizing of the capacitive load (capacitor bank or an unloaded cable) takes place [28]. In an offshore WP that consists of long cables with a substantial capacitance, the prestrikes are a common phenomenon that occurs during the energizing of the equipment. Energizing of a radial in a WP causes multiple prestrikes generating high transient overvoltages (TOV) [29].

For the multiple prestrike analysis in this chapter, the test setup used for the multiple

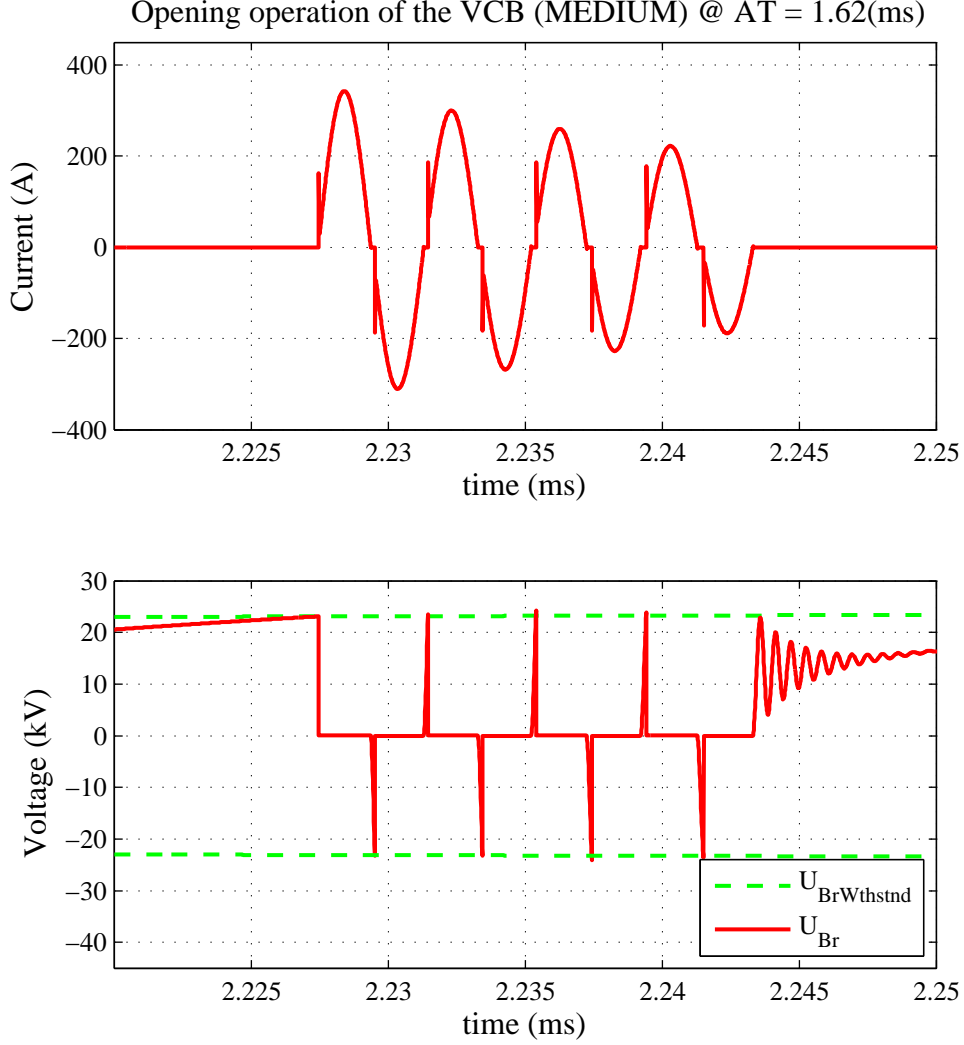


Figure 3.9: HF current quenching using VCB with medium interruption capability

reignition phenomenon analysis shown in Fig. 3.3 is used. The parameters of the VCB HF current quenching capability for this study is $C_C = 0$ and $D_D = 100 A/\mu s$. The multiple prestrikes can be observed in Fig. 3.10

Analyzing the multiple prestrike phenomenon, it can be observed that a very similar process described in the multiple restrike phenomenon takes place during the closing operation of the VCB. During the closing operation of the VCB, the gap between the contacts is reduced resulting in a decay of the dielectric withstand of the gap. The rate of decay of the dielectric strength (RDDS) is given by $B_B = 1V/\mu s$ while $A_A = 0.69kV$. As soon as the dielectric withstand of the VCB becomes lower than the voltage over the VCB, the arc is ignited between the contacts and the current flows through the VCB. This current consists of the HF current and the power frequency steady-state current. As the arc is ignited, the voltage over the VCB drops approximately to zero meaning that the decaying dielectric strength of the gap acts toward the arc interruption. Since the HF current cannot be interrupted unless the HF current quenching capability of the VCB is higher than the HF current derivative at a zero crossing, the HF current is interrupted after a number of zero crossings. The HF current interruption initiates a TRV over the VCB. The arc is established again when the TRV reaches the value of the decaying dielectric withstand of the VCB.

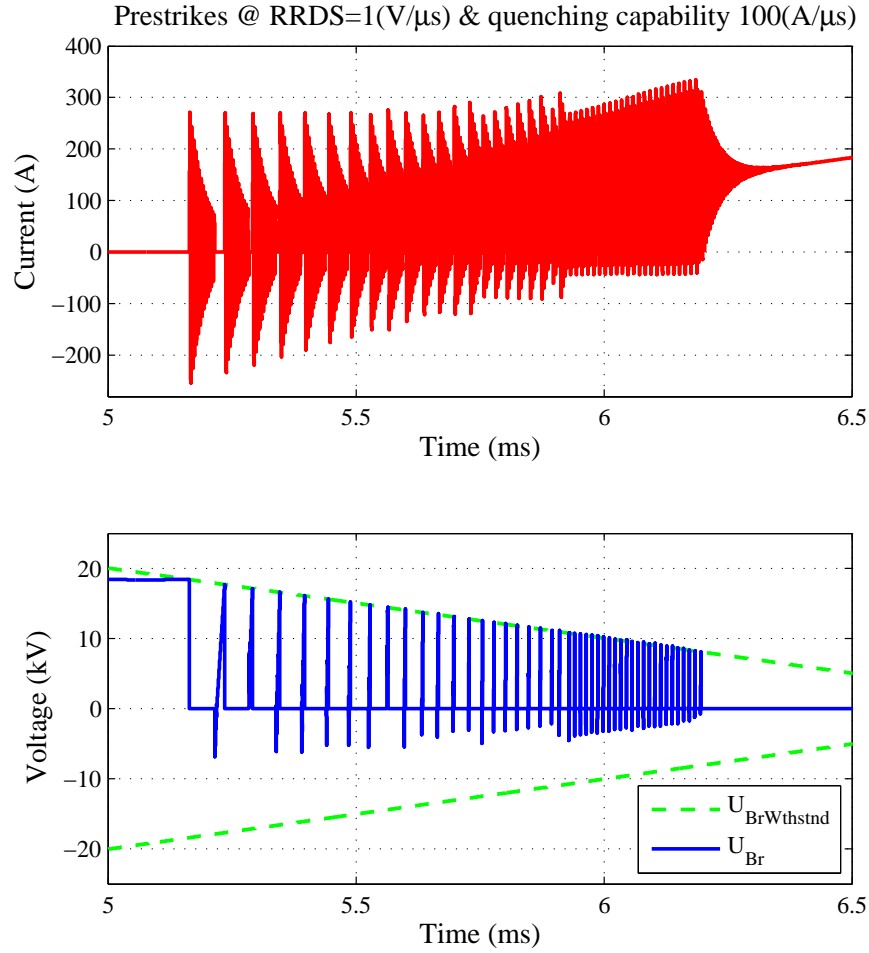


Figure 3.10: Prestrikes during the energizing of a test circuit ($D_D = 100A/\mu s$)

This process continues to produce multiple prestrikes until the dielectric withstand of the VCB reduces to such an extent that it is not able any more to interrupt the current. The HF current is damped approximately after $150 \mu s$ and the VCB conducts only the power frequency current afterwards.

For the number of prestrikes during the closing operation of the VCB, the HF current quenching capability of the VCB has an important role. For this study we will observe the VCB with the same RRDS capability, while the HF current quenching capability parameters are $C_C = 0$ and $D_D = 600 A/\mu s$. This means that the VCB is capable of interrupting the HF current almost at every zero crossing. The resulting multiple prestrikes can be noted in Fig. 3.11.

The multiple prestrikes phenomenon is influenced by the circuit parameters also. This phenomenon is going to be analyzed later when the energizing process is studied

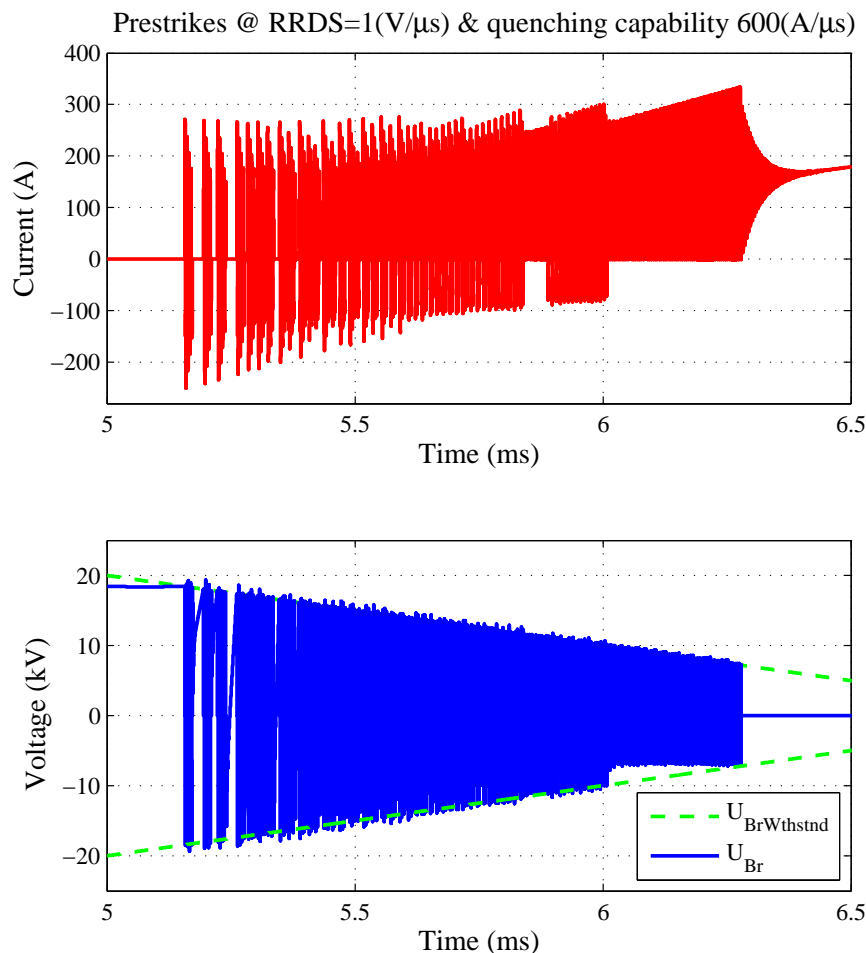


Figure 3.11: Prestrikes during the energizing of a test circuit ($D_D = 600A/\mu s$)

3.2 Modeling of Underground Cables

When the high frequency transients in systems where cables are present is studied, the reflection phenomenon will occur if the rise time of the transient is in the order of the wave traveling time across the cable. The velocity of the wave traveling across the cable is given by (2.38). For transmission lines, the velocity of the propagating wave is the same as the speed of light in vacuum, which is $300m/\mu s$. For cables, the wave propagation velocity is lower and it is $200m/\mu s$.

When the transformer is connected to the cable, then the rise time of the surge is given by (2.39). Since the stray capacitance of the transformers with oil impregnated paper insulation is in order of nF [53] and that of the dry-type transformers is approximately ten times smaller [58], the rise time of the surge is less than $100ns$ given that the surge impedance of the cable is in the order of a couple of tens of Ohms. This means that even very short cables with a length of tens of meters is long enough to establish observable wave propagation and reflection phenomenon. For that reason, the lumped cable model should be avoided and will not be treated in this thesis. Instead the focus is on the distributed parameter cable models, that allow for such a phenomenon to be studied.

To obtain a detailed model of the cable suitable for time domain simulations and studies

of the high frequency phenomena, a distributed parameter model is to be developed. To develop equations using this theory, an infinitely small piece of a single conductor line buried into the ground presented in Fig. 3.12 is observed.

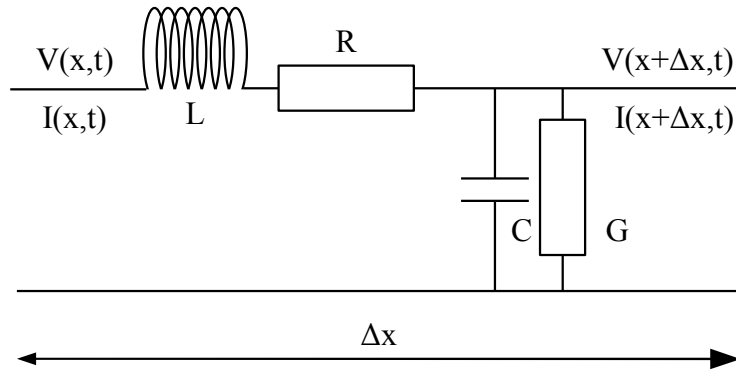


Figure 3.12: An infinitely small element of cable.

The time domain equations of a single conductor-line presented in Fig. 3.12 can be expressed as follows,

$$-\frac{\partial v(x,t)}{\partial x} = Ri(x,t) + L\frac{\partial i(x,t)}{\partial t} \quad (3.5)$$

$$-\frac{\partial i(x,t)}{\partial x} = Gv(x,t) + C\frac{\partial v(x,t)}{\partial t} \quad (3.6)$$

where $v(x,t)$ is the voltage of the line, $i(x,t)$ is the current of the line, while G, C, R and L are lumped parameters of the line that represent conductance, capacitance, resistance and inductance expressed in per-unit length. In a real cable, all these parameters are not constant, but frequency dependent. This means that the solution for these equations, even for the high frequency transients is performed in the frequency domain [30]. The set of frequency domain equations written for the same conductor can be written as

$$-\frac{d\mathbf{V}_x(\omega)}{dx} = \mathbf{Z}(\omega)\mathbf{I}_x(\omega) \quad (3.7)$$

$$-\frac{d\mathbf{I}_x(\omega)}{dx} = \mathbf{Y}(\omega)\mathbf{V}_x(\omega) \quad (3.8)$$

where $Z(\omega)$ and $Y(\omega)$ are the series impedance and the shunt admittance matrices of the cable per-unit length respectively. To determine the frequency dependent admittance and impedance matrix, different methods can be used, utilizing analytical expressions and finite element method calculations.

To solve system of equations given by (3.7) and (3.8), initially (3.8) is differentiated with respect to x and substituted into (3.7). A solution can now be found for the current, while a solution for the voltage vector needs some further deductions.

$$\frac{d^2 \mathbf{I}_x(\omega)}{dx^2} = \mathbf{Y}(\omega) \mathbf{Z}(\omega) \mathbf{I}_x(\omega). \quad (3.9)$$

The solution for (3.9) is given in the form of a sum of two traveling current waves propagating in forward and backward direction

$$\mathbf{I}_x = e^{-\Gamma x} \mathbf{I}_f + e^{\Gamma x} \mathbf{I}_b \quad (3.10)$$

where \mathbf{I}_f and \mathbf{I}_b are the forward and backward traveling waves of current and Γ is equal to $\sqrt{\mathbf{Y}\mathbf{Z}}$. The voltage vector can be found from (3.8) and (3.10) as follows

$$\mathbf{V}_x = -\mathbf{Y}^{-1} \frac{d\mathbf{I}_x}{dx} = \mathbf{Y}^{-1} \sqrt{\mathbf{Y}\mathbf{Z}} (e^{-\Gamma x} \mathbf{I}_f - e^{\Gamma x} \mathbf{I}_b) = \mathbf{Y}_c^{-1} (e^{-\Gamma x} \mathbf{I}_f - e^{\Gamma x} \mathbf{I}_b) \quad (3.11)$$

where \mathbf{Y}_c is the characteristic admittance matrix which is given by (3.12).

$$\mathbf{Y}_c = \sqrt{(\mathbf{Y}\mathbf{Z})^{-1}} \mathbf{Y} \quad (3.12)$$

In the next step, (3.11) is multiplied with \mathbf{Y}_c and added to (3.10) which yields

$$\mathbf{Y}_c \mathbf{V}_x + \mathbf{I}_x = 2e^{-\Gamma x} \mathbf{I}_f. \quad (3.13)$$

Applying boundary conditions for (3.13) at both ends of the cable, where for node 1, the cable length $x = 0$ and for node 2, the cable length $x = l$, (3.14) and (3.15) are obtained respectively.

$$\mathbf{Y}_c \mathbf{V}_1 + \mathbf{I}_1 = 2\mathbf{I}_f \quad (3.14)$$

$$\mathbf{Y}_c \mathbf{V}_2 + \mathbf{I}_2 = 2e^{-\Gamma l} \mathbf{I}_f = 2\mathbf{H}\mathbf{I}_f \quad (3.15)$$

The matrix \mathbf{H} is the wave propagation matrix. Substituting (3.14) into (3.15), the expression for the current in node 2 is obtained.

$$\mathbf{Y}_c \mathbf{V}_2 + \mathbf{I}_2 = \mathbf{H}(\mathbf{Y}_c \mathbf{V}_1 + \mathbf{I}_1) \quad (3.16)$$

In (3.16) the direction of current \mathbf{I}_2 is from the node like the direction of current \mathbf{I}_1 which is according to Fig. 3.12. When the direction of current \mathbf{I}_2 is into the node, (3.16) can be rewritten as

$$\mathbf{I}_2 = \mathbf{Y}_c \mathbf{V}_2 - \mathbf{H}(\mathbf{Y}_c \mathbf{V}_1 + \mathbf{I}_1). \quad (3.17)$$

In a similar way, the equation for current \mathbf{I}_1 can be obtained.

$$\mathbf{I}_1 = \mathbf{Y}_c \mathbf{V}_1 - \mathbf{H}(\mathbf{Y}_c \mathbf{V}_2 + \mathbf{I}_2) \quad (3.18)$$

(3.17) and (3.18) represent n coupled scalar equations but can be decoupled using modal decomposition. The modal decomposition matrices for the voltage and current vectors are obtained by

$$\mathbf{T}_I^{-1} \mathbf{Y} \mathbf{Z} \mathbf{T}_I = \lambda \quad (3.19)$$

where \mathbf{T}_I is the current transformation matrix and λ is the diagonal eigenvalue matrix. According to the eigenvalue theory [31], the voltage and current vectors and matrices of \mathbf{Y}_c and \mathbf{H} can be transformed using the following equation

$$\begin{aligned} \mathbf{I} &= \mathbf{T}_I \mathbf{I}^m \\ \mathbf{V} &= \mathbf{T}_v \mathbf{V}^m \\ \mathbf{Y}_c &= \mathbf{T}_I \mathbf{Y}_c^m \mathbf{T}_I^T \\ \mathbf{H} &= \mathbf{T}_I \mathbf{H}^m \mathbf{T}_I^{-1} \end{aligned} \quad (3.20)$$

where \mathbf{I}^m , \mathbf{V}^m , \mathbf{Y}_c^m and \mathbf{H}^m are the modal voltage vector, current vector, characteristic admittance matrix and wave propagation matrix. It should be noted that

$$\mathbf{T}_V = \mathbf{T}_I^{-T} \quad (3.21)$$

where \mathbf{T}_I^{-T} is the transpose of \mathbf{T}_I^{-1} . Now (3.17) and (3.18) can be rewritten in the form of n decoupled equations after modal decomposition.

$$\mathbf{I}_1^m = \mathbf{Y}_c^m \mathbf{V}_1^m - \mathbf{H}^m (\mathbf{Y}_c^m \mathbf{V}_2^m + \mathbf{I}_2^m) \quad (3.22)$$

$$\mathbf{I}_2^m = \mathbf{Y}_c^m \mathbf{V}_2^m - \mathbf{H}^m (\mathbf{Y}_c^m \mathbf{V}_1^m + \mathbf{I}_1^m) \quad (3.23)$$

In earlier studies [32] the frequency independent modal decomposition is performed. However, when the frequency dependent modal decomposition is performed, the modal decomposition matrices have to be calculated for each frequency. This model does not require as much computations as a full frequency dependent modal domain models but has a good accuracy both in the steady-state and transient conditions [33]. When transformed to the time-domain, (3.22) and (3.23) become

$$i_1(t) = y_c(t) * v_1(t) + h(t) * (y_c(t) * v_2(t) + i_2(t)) \quad (3.24)$$

$$i_2(t) = y_c(t) * v_2(t) + h(t) * (y_c(t) * v_1(t) + i_1(t)). \quad (3.25)$$

where symbol '*' denotes matrix-vector convolutions. When functions of \mathbf{Y}_c and \mathbf{H} are fitted with rational functions [33], then the time-domain functions can be obtained using

recursive convolutions [34]. When recursive convolutions used, the expression for nodal currents at both cable ends can be written using a history current term, node voltage and equivalent admittance.

$$i_1(t) = y_{eq}(t)v_1(t) + i_{hist-1}(t) \quad (3.26)$$

$$i_2(t) = y_{eq}(t)v_2(t) + i_{hist-2}(t) \quad (3.27)$$

This can be presented in the circuit with an ideal current source and an equivalent admittance which is shown in Fig. 3.13.

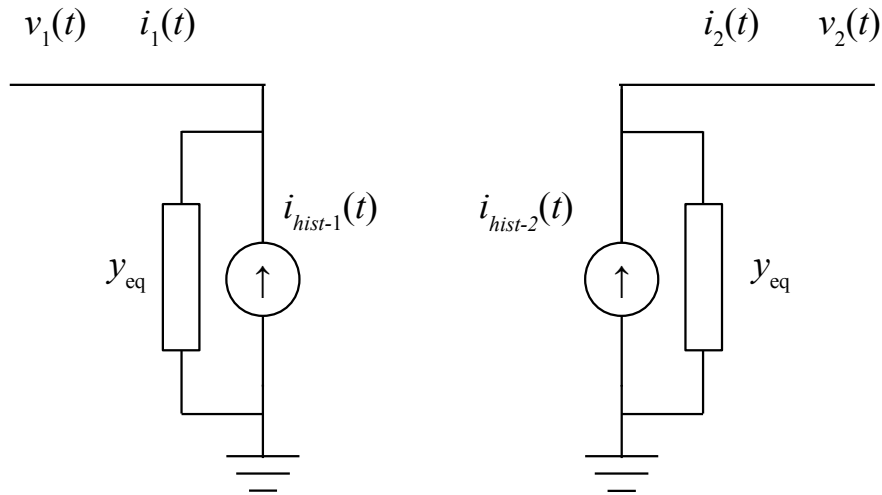


Figure 3.13: Network interface of the cable model.

3.2.1 Cable Modeling in PSCAD/EMTDC

Cable and Transmission Line Models

The cable models and the transmission line models in PSCAD/EMTDC are distributed parameter models where the parameters of the cable are frequency dependent. However, the main differences between the three available models are if the model includes lossless or lossy representation of the line equations and if the transformation matrices for the modal-decomposition are constant or frequency dependent and latter fitted in the phase domain using rational functions and later integrated using recursive convolutions.

The Bergeron cable model is the least accurate cable model for the high frequency transient analysis. This model is a lossless model, but still the cable reflections can be studied since the mathematical description uses the same approach as given in Section 3.2. It should be noted that the \mathbf{Y}_c matrix for a lossless line contains only real numbers and is presented with \mathbf{G}_c matrix. That is why the network interface of the model uses ideal current sources representing the history current and equivalent conductance.

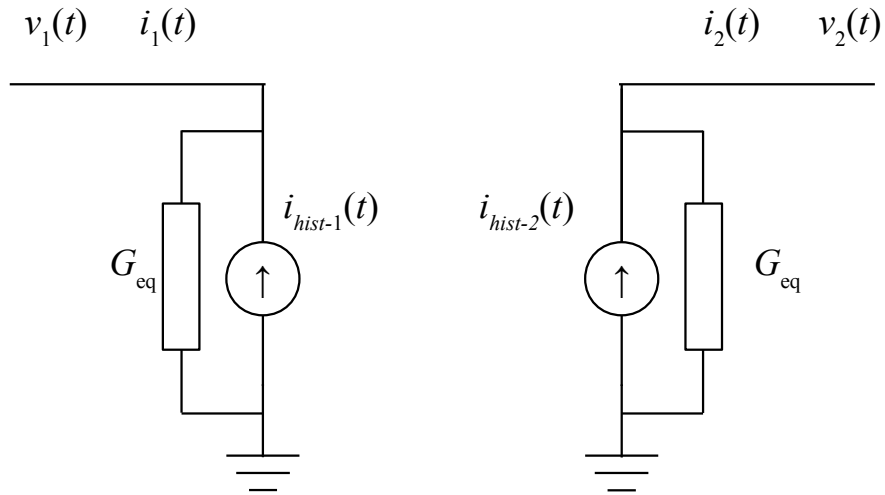


Figure 3.14: Network interface of Bergeron model.

The accuracy of the model for transient time-domain simulations is not satisfactory for a wide band of frequencies. It is accurate only for the power frequency [49]. Observing Fig. 3.16 it is easy to note the difference between the frequency dependent cable model and the Bergeron model when the cable model is used for high frequency transient studies.

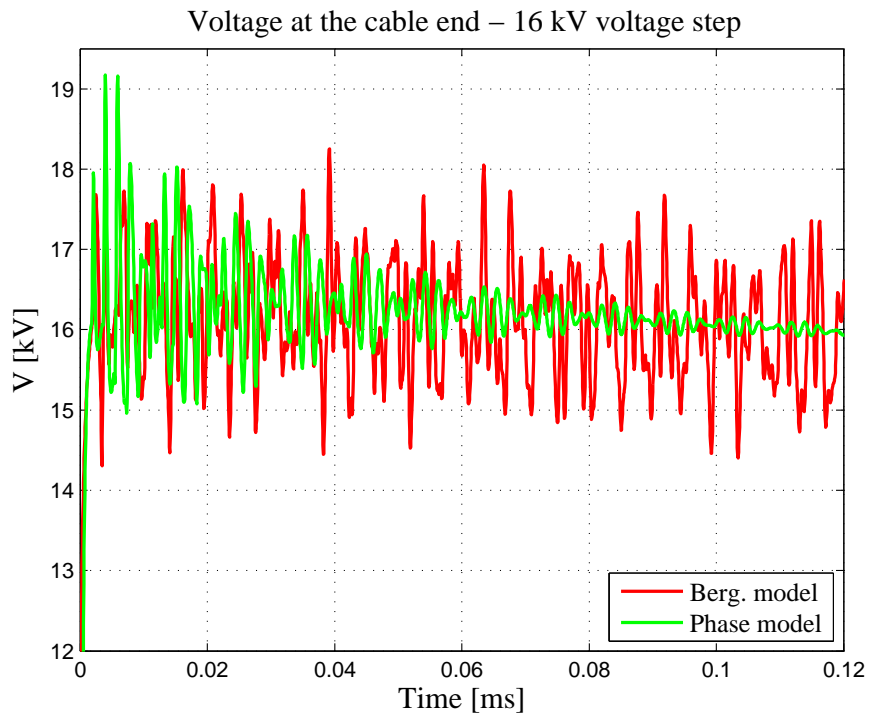


Figure 3.15: Damping Figure from Utgrunden

It can be noted that the damping of the Bergeron model is very weak since the cable is treated as lossless.

For better accuracy, PSCAD/EMTDC offers two different lossy cable models for transient analysis. The first is called the Frequency Dependent (Mode) model, representing

a model with constant modal decomposition matrices [32] while the more advanced Frequency dependent(Phase) model use rational approximation of \mathbf{Y}_c^m and \mathbf{H}^m matrices as explained in Section 3.2 allowing recursive convolution calculations. This method is based on a novel rational function fitting technique called the vector fitting (VFT) [35]. Accuracy and computation efficiency is improved compared to the frequency dependent(mode) model [36] providing very accurate time-domain simulations for the high frequency transients and for the steady-state operation.

Cable Geometry Definition in PSCAD/EMTDC

PSCAD/EMTDC provides an interface for the definition of physical properties of cables and transmission lines. For the transmission lines, the user can define different types and sizes of towers. A detailed information about the number of sub-conductors in a bundle is to be defined for certain types of towers. Definition of multi-pipe cables is provided where user can specify the position and dimension of each cable. A configuration of the three phase cable is shown in Fig. 3.16

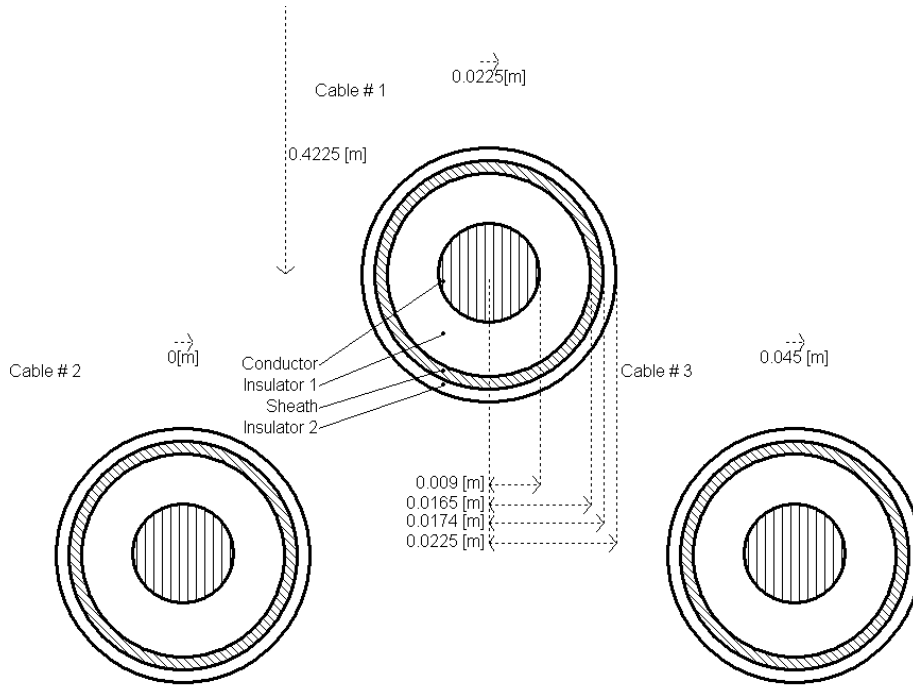


Figure 3.16: Geometry definition of three phase cable in PSCAD/EMTDC.

Although a multi-pipe geometry can be entered in the PSCAD/EMTDC interface, the PSCAD/EMTDC model treats the multi-pipe model as the model with separate three single phase cables. The capacitances of the multi-pipe cable are calculated only for one phase and mutual capacitances between cables are neglected. The capacitances between conductors in one cable are calculated using the formula that neglects semiconductor layers assuming constant relative permittivity over the insulator in between. This gives

$$C = \frac{2\pi\epsilon_r\epsilon_0}{\ln\left(\frac{D}{a}\right)} \quad (3.28)$$

where, ε_r and ε_0 are relative permittivity and the permittivity of the vacuum respectively and D and d are diameters of the outer and inner conductor.

To take the capacitive coupling between phases into account in a multi-pipe cable as well as the influence of the semi-conducting layers, a cable model is developed in a FEM software. For this purpose, the COMSOL software is used which enables the entry of parameters of the cable materials more in detail than it is possible in PSCAD/EMTDC.

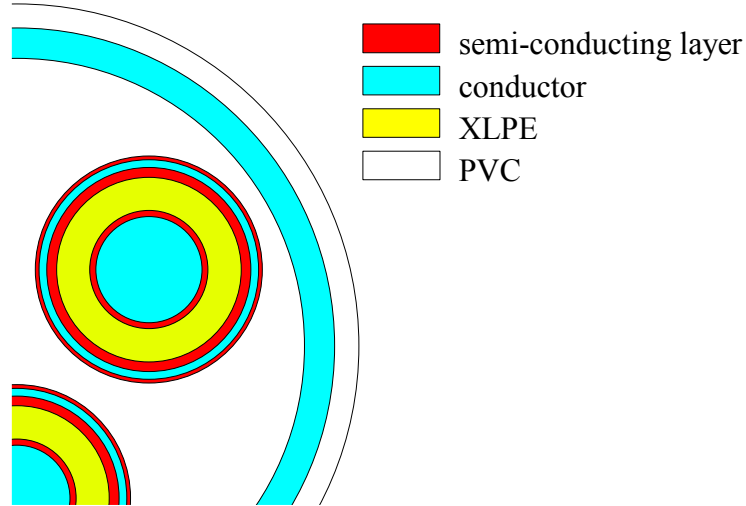


Figure 3.17: Detailed cable model

As can be observed in Fig. 3.17, a more complex model is designed compared to the PSCAD/EMTDC model. For the COMSOL model, the relative permittivity of the insulating and semi-conducting layers is set to the constant value of $\varepsilon_{XLPE} = 2.3$ and $\varepsilon_{semi_cond} = 12.1$ respectively. The conductivity of the semi-conducting layers is set to $\sigma_{semi_cond} = 1.6e - 3 S/m$ while the conductivity of the XLPE insulation is negligible. To study the conductor-shield capacitance, an analytical expression that neglects the conductance of the insulating layers and the COMSOL calculated capacitance are compared. To obtain the capacitances between the conductors in the cable, the *in-plane electric and induction currents and potentials* model is used. The boundary settings of the conducting layers are set to *port* with input property *forced voltage*. The model is solved using a parametric solver where the frequency is set to vary between $50Hz$ and $10MHz$. In this application mode, the admittance matrix \mathbf{Y} of the cable is obtained. The capacitance matrix \mathbf{C} of the cable is calculated by

$$\mathbf{C} = \frac{imag\{\mathbf{Y}\}}{2\pi f} \quad (3.29)$$

where f is the frequency. When there are multiple insulating layers with different relative permittivity placed between the conductor and the shield cylindrical conducting layers as it is the case in the XLPE cable, an analytical expression for the capacitance between the conductor and the shield C_{CS} is given by

$$C_{CS} = \frac{2\pi\varepsilon_0}{\frac{\ln\left(\frac{r_2 r_4}{r_1 r_3}\right)}{\varepsilon_{semi_cond}} + \frac{\ln\left(\frac{r_3}{r_2}\right)}{\varepsilon_{XLPE}}} \quad (3.30)$$

where r_1 and r_4 are the outer radius of the conductor and inner radius of the shield respectively, r_2 and r_3 are the outer radius and the inner radius of the of the semi-conducting layer respectively. The calculation of the conductor-shield capacitance using the analytical expression and COMSOL is presented in Fig. 3.18.

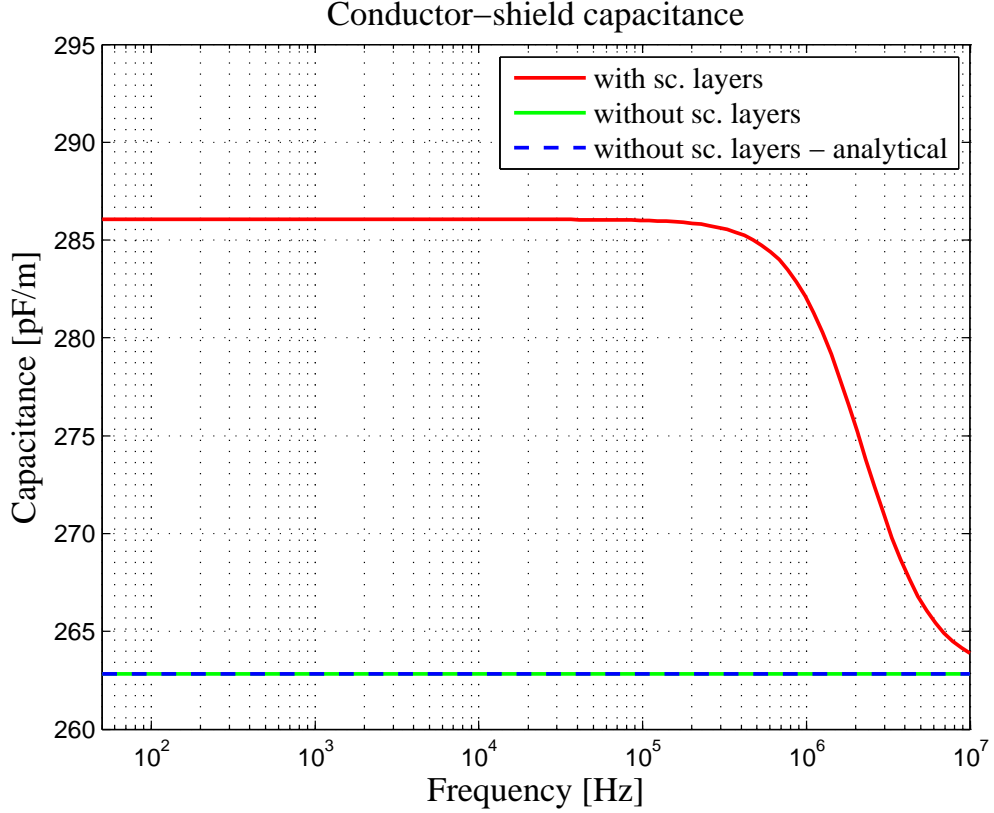


Figure 3.18: Capacitance comparison

It can be noted in Fig. 3.18 that there is a significant influence of the semi-conducting layers on the cable capacitance. Due to different time constants (ϵ_r/σ) of different insulation levels, the capacitance is varying with frequency and will approach the capacitance of the simplified cable model only at frequencies higher than $10MHz$. The difference between the capacitances for models with and without semi-conducting layers for a frequency range from $50 - 10^6 Hz$ is 8.8%. This is a quite significant margin and will influence even the steady state values for $50Hz$ signals. This means that the capacitance should be adjusted in such a way so it takes the influence of the different (ϵ_r/σ) properties of the semi-conducting layers and the XLPE insulation into account.

Since the cable model interface in PSCAD/EMTDC allows the definition of insulators and conductors only, the semi-conducting layers and the XLPE layer between the conductor and the shield are replaced by a single insulator. These layers with different electric properties are to be represented by only one layer with the ϵ_{res} and σ_{res} values that will match the capacitance of the full cable model

$$C_{CS} = \frac{2\pi\epsilon_0}{\frac{\ln\left(\frac{r_2 r_4}{r_1 r_3}\right)}{\epsilon_{semi_cond}} + \frac{\ln\left(\frac{r_3}{r_2}\right)}{\epsilon_{XLPE}}} k_{cap} = \frac{2\pi\epsilon_{res}\epsilon_0}{\ln\left(\frac{r_4}{r_1}\right)} \quad (3.31)$$

not consider the non-linearities of the core when the transformer is saturating. However, when the fast transients are studied, the transformer can be considered linear if one of the windings is loaded [42]. If the transformer is unloaded it is considered linear only for the transients with frequencies higher than $100kHz$ [42]. The most important problem for those who want to develop such a model is that the internal structure of the power transformer is not available even to the transformer owner. If needed, even the owner of the transformer can not develop detailed transformer model for transient analysis unless the transformer is opened and it's structure analyzed.

Another, more practical method is to design a black-box model of the transformer. The first developed black-box transformer models were based on modal analysis [43] previously used in mechanics to describe the dynamic behavior of elastic structures [43]. To develop a black-box model, measurements are carried out to determine the admittance matrix. Numerous scientific articles are written on this topic [43]-[46]. Once the admittance matrix is measured for the wide band of frequencies, the admittance or impedance vector between each terminal is fitted with a rational form given in the frequency domain as

$$Y(s) = Z(s)^{-1} = \frac{a_0s^m + a_1s^{m-1} + \dots + a_{m-1}s + a_m}{b_0s^n + b_1s^{n-1} + \dots + b_{n-1}s + b_n}. \quad (3.33)$$

The function presented in (3.33) can be presented as a sum of partial functions as shown in (3.34), and the least square fitting method for the complex curve may be used [46] to obtain parameters r_m, a_m, d and e .

$$Y(s) = \sum_{m=1}^N \frac{r_m}{s - a_m} + d + se \quad (3.34)$$

For a three phase transformer, there are 36 admittance vectors and each one of them has to be fitted. However, the problem can be simplified since it has been shown that the admittance vectors have a common set of poles [48].

For the time-domain simulations it is necessary either to develop the equivalent network [43], [45], [47] or to use recursive convolutions [34]. The method of recursive convolutions is used to obtain the time-domain simulations for the frequency dependent cable models as shown before.

3.3.1 Transformer Modeling for Low Frequency Transient Analysis

For the transients with the frequencies reaching up to $3kHz$, the core nonlinearities are important and for the proper transient studies they have to be implemented in the transformer model [25]. This is the case even when the transient frequency reaches $20kHz$ if the transient energizing and the load rejection with high voltage increase are studied [25].

The PSCAD/EMTDC software includes different transformer models that include the model of the core nonlinearities. The transformer models are based on scheme presented in Fig. 3.20.

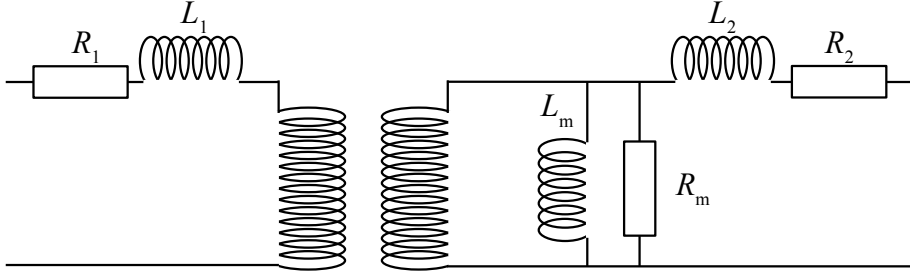


Figure 3.20: Transformer model implemented in PSCAD

The parameters of the transformer L_1 , L_2 , R_1 , R_2 and R_m are kept constant. Core nonlinearities are modeled so the parameter of the mutual inductance L_m is modeled according to the saturation curve defined in the properties of the model. PSCAD/EMTDC offers two different transformer models when it comes to the saturation modeling. The first model does not take into account the magnetic coupling between different phases, so from the magnetic aspect, the three phase transformer is treated as three single phase transformers [49]. The magnetic coupling between phases does not exist and if one phase is saturated, the others are not affected. In order to improve the transformer model, an effort is made for more detailed modeling of the three phase transformer saturation [50]-[51]. For the transformer model based on the Unified Magnetic Equivalent Circuit (UMEC) algorithm, phases are magnetically coupled as shown in Fig. 3.21.

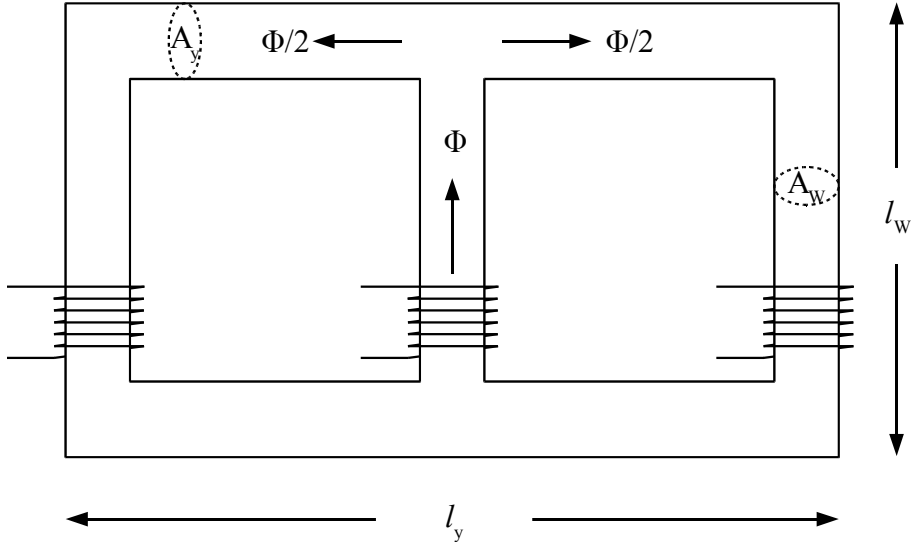


Figure 3.21: Core model used in UMEC algorithm

However, since the resistance parameters of the transformer model which represent losses in the transformer windings, and the losses in the core are constant, the skin effect, the proximity effect and the core losses which are frequency dependent are not accounted for correctly. To analyze the impact of the skin effect on the transformer winding resistance, the COMSOL software is used. The resistance of the transformer conductor changes significantly if the frequency increases from $50Hz$ to $1kHz$. The current density figures at $50Hz$ and $1kHz$

is shown in Fig. 3.22

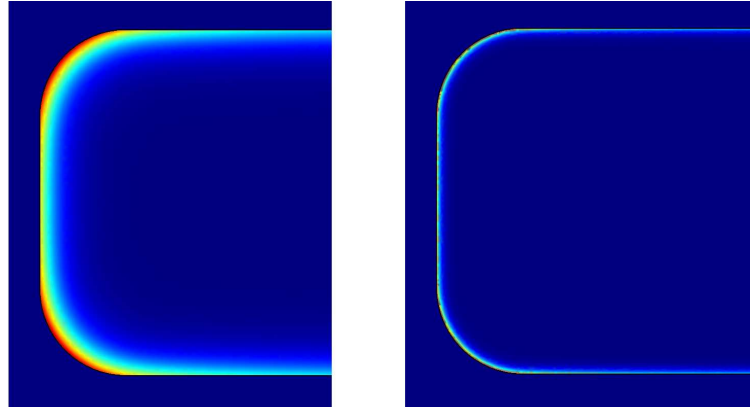


Figure 3.22: Current density in transformer conductor at $50Hz$ and $1kHz$

For the $1kHz$ signal, the current is pushed towards the surface of the conductor thus increasing the resistance of the conductor.

The resistance of the transformer windings as the function of frequency is plotted in Fig. 3.23

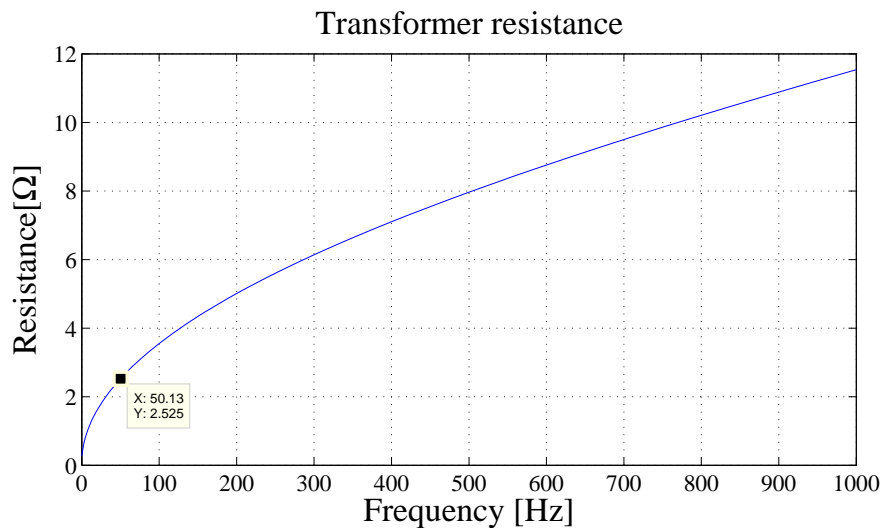


Figure 3.23: Resistance of the transformer windings as the function of frequency

To account for the frequency dependent resistance of the transformer conductors, the standard PSCAD/EMTDC model is extended using the Foster equivalent circuit. The parameters of the Foster circuit are calculated using the vector fitting algorithm [35]. In order to account properly for the skin effect in the transformer windings, the leakage reactance and the frequency dependent resistance of the windings are fitted using the vector fitting algorithm [35],[47] and added to the existing UMEC model. The winding resistance and the leakage reactance of the model in PSCAD/EMTDC is adjusted accordingly, giving that at the $50Hz$ frequency, the Foster equivalent network connected in series with the UMEC transformer model will give a correct value of the leakage reactance and the winding resistance.

In the upper part of Fig. 3.24, an equivalent Foster circuit with parameters fitted to match the transformer impedance up to $1kHz$ is presented. When the Foster equivalent

circuit is added to the PSCAD/EMTD transformer model based on the UMEC algorithm, than R_0 and L_0 are added to the leakage reactance and the winding resistance parameters which are entered directly into the model parameters. The equivalent network consisting of the Foster equivalent network and the UMEC transformer model is shown in the lower part of Fig. 3.24

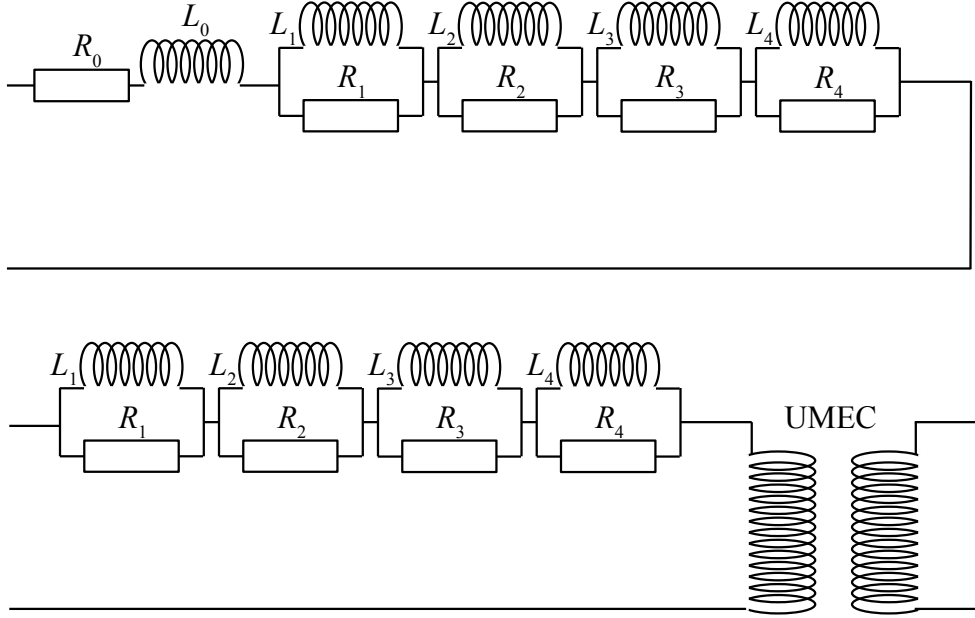


Figure 3.24: Transformer model that takes into account skin effect in transformer windings

3.3.2 Transformer Modeling for High Frequency Transient Analysis

When the analysis of the high frequency transients is required, a suitable transformer model is needed to give a proper response to the high frequency transients generated mainly during the operation of the switching apparatus. The model described in the previous section, with modeled skin effect of the windings is suitable for the low frequency transients. For the low frequency transient, the leakage reactance is the dominant component of the transformer impedance and in power system analysis, the transformer is usually represented with an ideal transformer and the transformers corresponding leakage reactance. However, when the frequency moves to the other side of the frequency spectrum approaching infinity, it has been observed on various types of rotating machines and transformers that the impedance is approaching zero [42].

$$\lim_{\omega \rightarrow \infty} \{|Z(j\omega)|\} = 0 \quad (3.35)$$

The phase angle of the transformer impedance for the low frequency disturbances as mentioned before is approximately 90° degrees or $\frac{\pi}{2}$ radians. However, when the frequency approaches infinity, the argument of the impedance approaches -90° degrees or $-\frac{\pi}{2}$ radians. So, for the high frequencies, the transformer stray capacitances dominate in the transformer response.

$$\lim_{\omega \rightarrow \infty} \{Arg [Z (j\omega)]\} = -\frac{\pi}{2} \quad (3.36)$$

Therefore, a very simple but reasonably accurate model of the transformer for very high frequency transient analysis can be made using only a capacitor connected in parallel to the standard model. This approach was used in many studies [53]-[55] and proved to give satisfactory results for the high frequency transient analysis. Usually for the transient studies, only the stray capacitance of the transformer side exposed to the transient is to be added to the standard transformer model. This is good for the specific type of studies when a VCB, cable and loaded/unloaded transformer system is observed for the switching transient studies. This is the case of transients in collection grids in wind parks [54] and is used in this study. If the surges through transformers are the subject of study, then the stray capacitance between primary and secondary side and the stray capacitance between the secondary side and the ground are important [53].

For the values of the stray capacitances, the manufacturer of the transformer should be contacted. However, the value of these capacitances are within certain limits for a specific rated power of the transformer and can be taken approximately [53],[56] and [57]. For the core-form transformers, typical values of stray capacitances are given in Table 3.3 [53]. For the dry-type transformers, the value of the stray capacitances are in order of hundreds of pico Farads [58] or approximately ten times smaller compared to the core-form transformer transformers.

Table 3.3: Typical stray capacitances of HV and LV to ground and between HV and LV sides (nF)

Transformer rating (MVA)	HV-ground cap.	LV-ground cap.	HV-LV capacitance
1	1.2-14	3.1-16	1.2-17
2	1.2-16	3-16	1-18
5	1.2-14	5.5-17	1.1-20
10	4-7	8-18	4-11
25	2.8-4.2	5.2-20	2.5-18
50	4-6.8	3-24	3.4-11
75	3.5-7	2.8-13	5.5-13

Chapter 4

Practical Case Studies

4.1 Utgrunden Wind Park Cable Energizing

The Utgrunden wind park (WP) is a wind park located in southern Kalmarsund in Sweden with a rated power production of 10 MVA. The WP is connected to the 55 kV grid on Öland at the Degerhamn substation. The Utgrunden WP consists of 7 wind turbines (WT) each rated at 1.5 MVA. The Utgrunden WP is placed 8 km west of the island of Öland and the power is transported to the PCC using sea cable. A simplified presentation of the Utgrunden WP is given in Fig. 4.1.

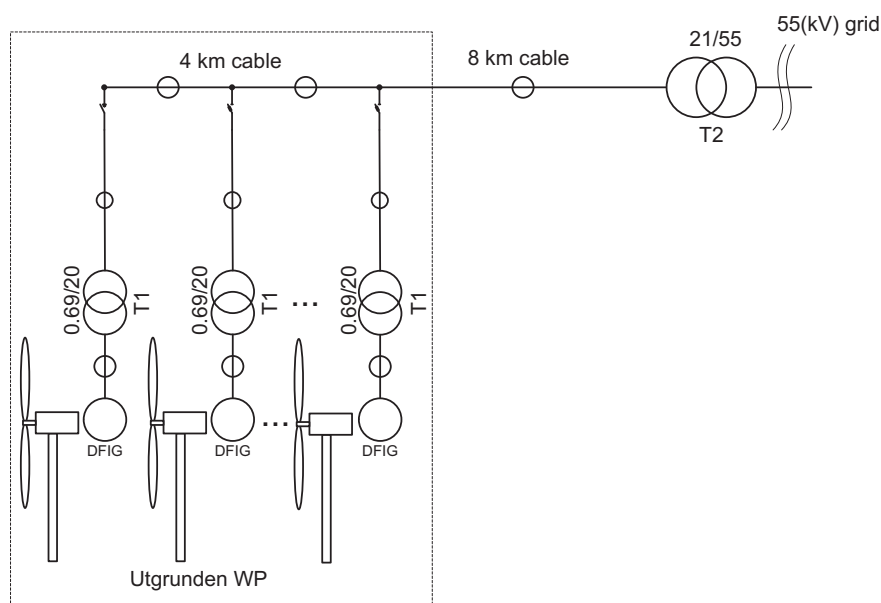


Figure 4.1: Utgrunden WP, sea cable and 21/55kV/kV substation

The WTs used at Utgrunden are of doubly-fed induction generator (DFIG) type.

The cable used in the Utgrunden WP is a 24 kV XLPE cable. The length of the cable from the WP to the 21/55 kV transformer in the Degerhamn substation is 8 km and the park is about 4 km long. The sea cable has a rated current of 275 A. The other important parameters of the cable such as the capacitance, inductance and resistance per unit length

are:

$$\begin{aligned} C_{km} &= 0.281 \mu F/km \\ L_{km} &= 0.352 mH/km \\ R_{km} &= 0.14 \Omega/km. \end{aligned}$$

In order to use these parameters in the advanced PSCAD/EMTDC cable model, the dimensions of the cable have to be determined. Observing the data sheets in ABB's "XLPE Cable Systems - User's guide" a perfect match could not be found. The cable with electrical parameters that is the closest match, is a 24 kV cable with 240 mm² cross-section of the conductor. The outer diameter of this cable matches to the outer diameter of the cable used in the Utgrunden WP. The parameters of this cable such as the capacitance and inductance per unit length are:

$$\begin{aligned} C_{km} &= 0.31 \mu F/km \\ L_{km} &= 0.35 mH/km. \end{aligned}$$

For the cable length of 12 km the total cable capacitance, inductance and reactances are calculated to be:

$$\begin{aligned} C_{12km} &= 3.72 \mu F \\ L_{12km} &= 4.2 mH \\ X_C &= 855 \Omega \\ X_L &= 1.32 \Omega. \end{aligned}$$

In the WTs, the 24 kV XLPE cable is connected to the local WT transformer which transforms the 21 kV voltage level to 690 V which is appropriate for the induction generators. The rating of the transformer is 1.6 MVA with an assumed short-circuit impedance of 6 %. A calculation of the base impedance at the 20 kV bus gives the value of $Z_{bT1} = 250 \Omega$ and the reactance and inductance of the transformer seen from the 20 kV bus are $X_{T1} = 15 \Omega$ and $L_{T1} = 47 mH$.

The transformer in the Degerhamn substation has a Y/Y winding connection with a 21kV/55kV ratio and a rated power of 12 MVA. On the high-voltage side of the transformer, there is a tap changer used for the adjustment of the transformer ratio with steps of $\pm 1.67 \%$. The primary voltage can be adjusted in 8 steps. The base impedance referred to the 21 kV side of the transformer is $Z_{bT2} = 36.75 \Omega$. The short circuit impedance is $Z_{T2 pu} = 0.4 + j6 \%$ or $Z_{T2} = 0.147 + j2.2 \Omega$

$$\begin{aligned} X_{T2} &= 2.2 \Omega \\ R_{T2} &= 0.147 \Omega. \end{aligned}$$

The inductance of the transformer seen from the low-voltage side is $L_{T2} = 7 mH$.

The 55 kV grid has a short-circuit power of 126 MVA with a grid impedance angle of 73°. The short-circuit impedance referred to the 55 kV grid side is $Z_{gr} = 24 \Omega$. Taking into account the value of the impedance angle, the short circuit reactance and resistance of the 55 kV grid connected in the Degerhamn substation is:

This gives the inductance and resistance of the 55 kV grid to be $L_{gr} = 73 mH$ and $R_{gr} = 7 \Omega$. Referred to the 21 kV voltage level, the inductance of the grid is $L_{gr(21)} = 10.6 mH$ and the resistance is $R_{gr(21)} = 1.02 \Omega$

$$\begin{aligned} X_{gr} &= 23 \Omega \\ R_{gr} &= 7.02 \Omega. \end{aligned}$$

4.1.1 Resonance in the Utgrunden wind park

The Utgrunden WP presented in a single-line diagram can be seen in the Fig. 4.2.

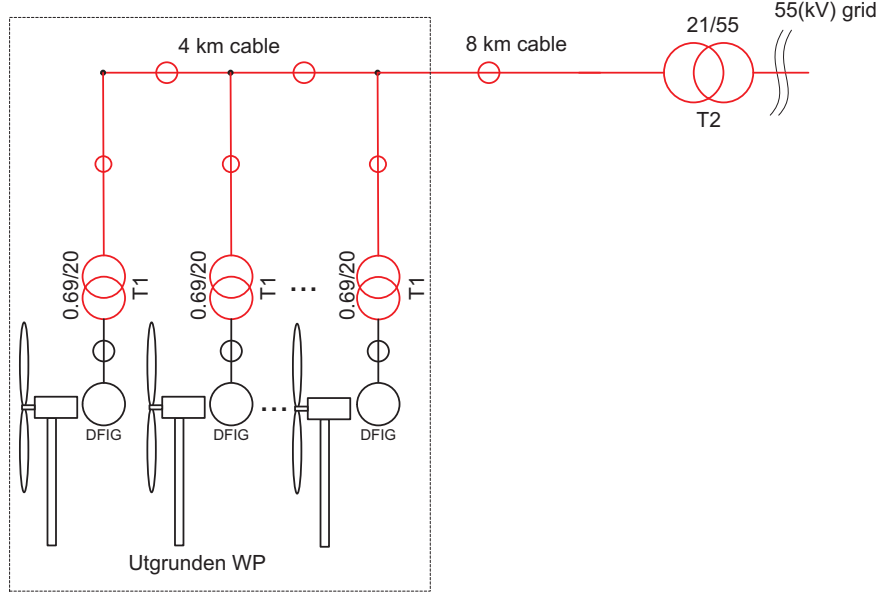


Figure 4.2: Simplified single phase diagram

As the switch of the transformer T2 is closed (on the 21 kV side) the cable and the WT transformers are energized. The capacitance of the cable is dominating in the system and the other capacitances are neglected. The calculated resonance frequency, taking into account the total inductance of the system consisting of the T2 transformer inductance L_{T2} , the cable inductance $L_{12 km}$, the inductance of the 55 kV grid referred to the 21 kV level and the total system capacitance consisting of the cable capacitance $C_{12 km}$ is :

$$f_{res} = \frac{1}{2\pi \sqrt{C_{12km}(L_{12km} + L_{T2} + L_{gr(21)})}} = 559 \text{ Hz} \quad (4.1)$$

4.1.2 Measurements and analysis of cable energizing in Utgrunden

In Fig. 4.3 and Fig. 4.4 the voltages and currents of T2 are presented during energizing.

After the cable has been energized, the voltage rises slightly due to the reactive power generated by the cable capacitance. The rise of the voltage can be seen on Fig. 4.5

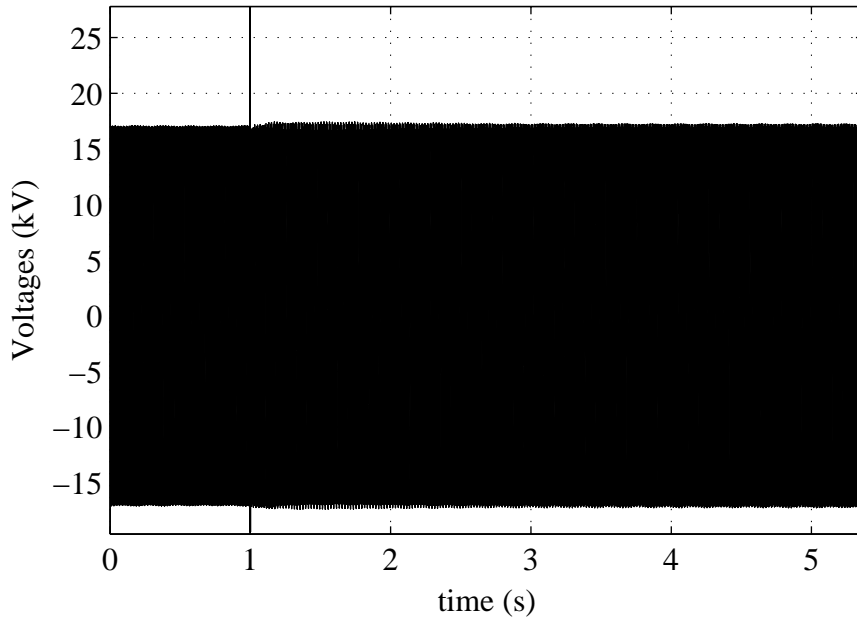


Figure 4.3: Phase voltages during energizing

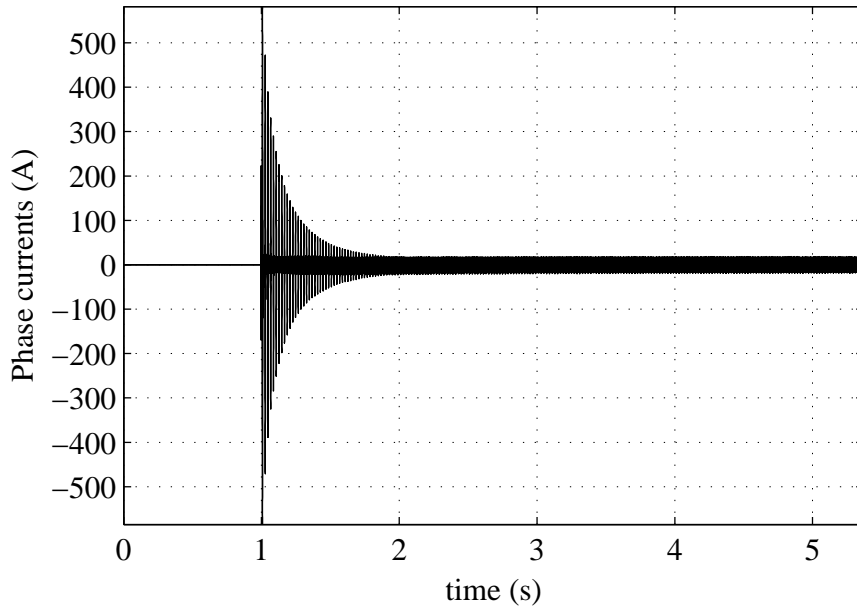


Figure 4.4: Phase currents during energizing

A zoom of the voltages and currents are shown in Fig. 4.6 and Fig. 4.7

In these figures the resonance frequency of approximately 794 Hz can be observed. The calculated resonance frequency differs from the measured frequency for 235 Hz . The calculation of the resonance frequency is quite sensitive to small deviation of capacitances and inductances present in the system and such deviation was expected given the difficulties in defining cable parameters.

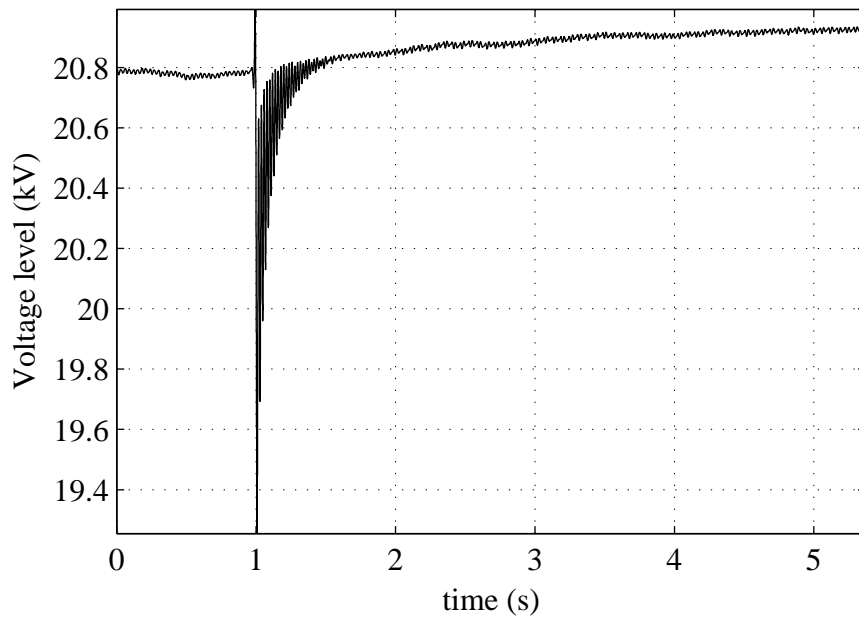


Figure 4.5: Voltage level when cable is energized

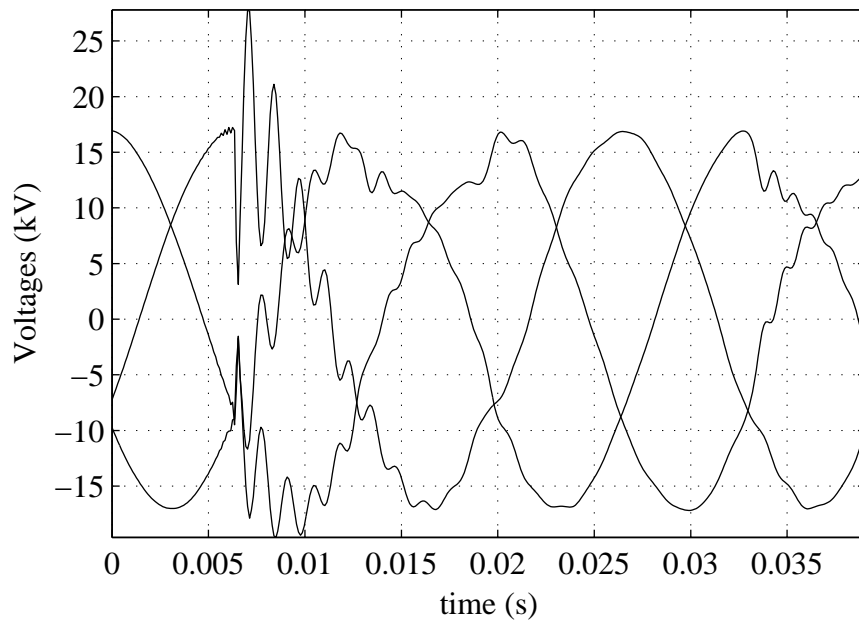


Figure 4.6: Phase voltages during transient

In the very beginning of the transient, between the time instants of $t = 0.0065$ s and $t = 0.012$ s, the current transient caused by the cable energizing can be seen in Fig. 4.7. After the cable is energized, the transformer becomes heavily saturated drawing strongly distorted currents with peak value of about 580 A. The current caused by the T2 transformer energizing is shown more in detail in Fig. 4.8.

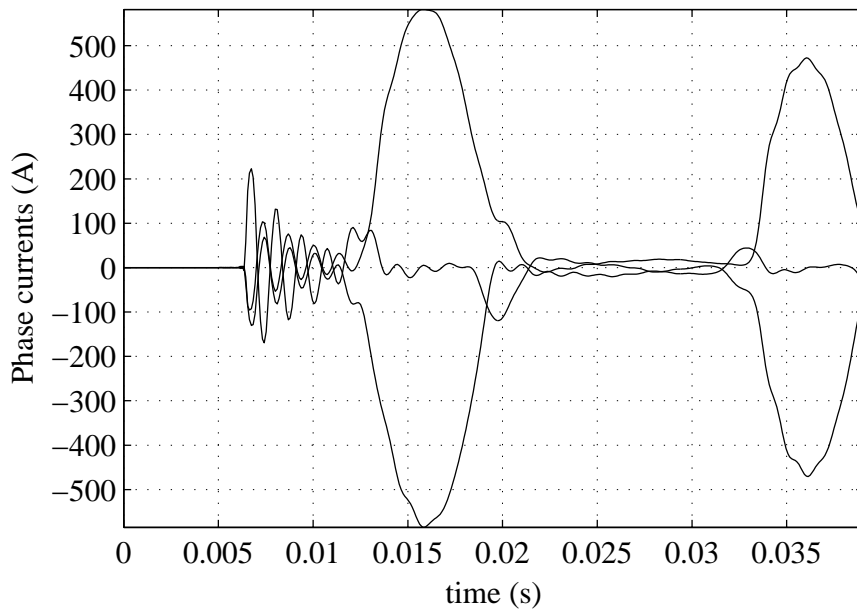


Figure 4.7: Phase currents during transient

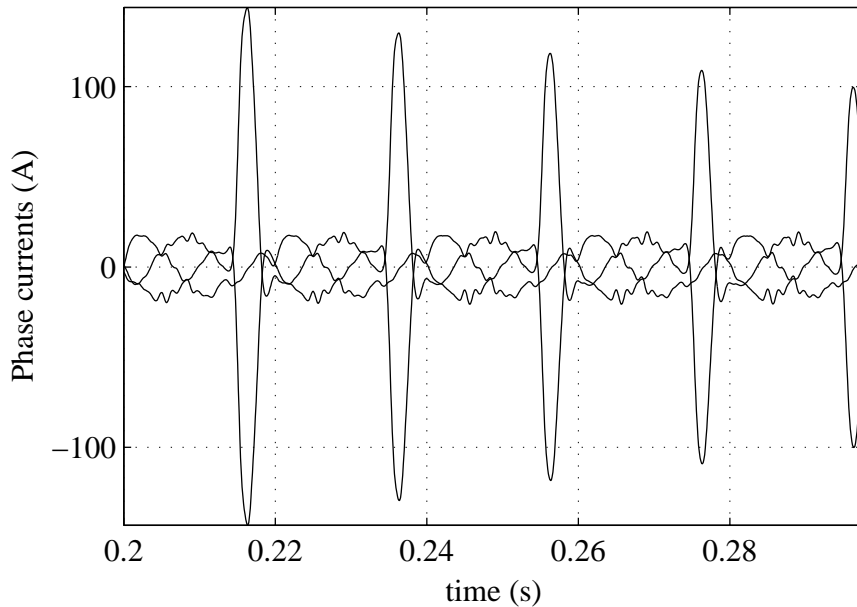


Figure 4.8: Phase currents during the transformer energizing transient

After a time period of 1 s the current transient has ceased and only the no-load capacitive current caused by the cable capacitance remains in the system, which is shown in Fig. 4.9.

Now, the cable and transformer energizing of the Utgrunden WP is simulated using PSCAD/EMTDC. The system is modeled using master library components. The test is performed by closing the breaker on the 21 kV side of the T2 transformer. By closing the breaker, the energizing of the cable and of the transformers in the WT's is initiated.

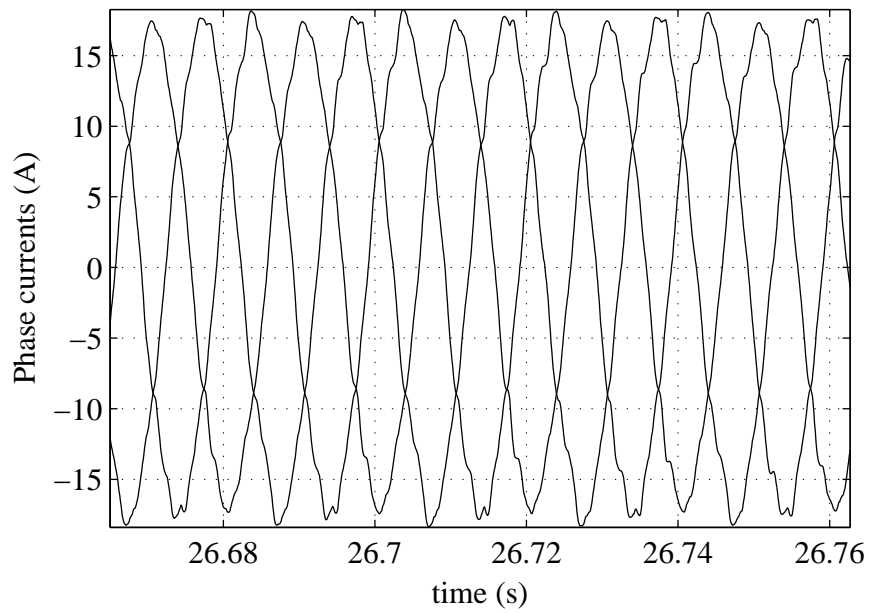


Figure 4.9: Steady-state phase currents - no-load current

In Fig. 4.10 and Fig. 4.11 the voltage and current of T2 is presented.

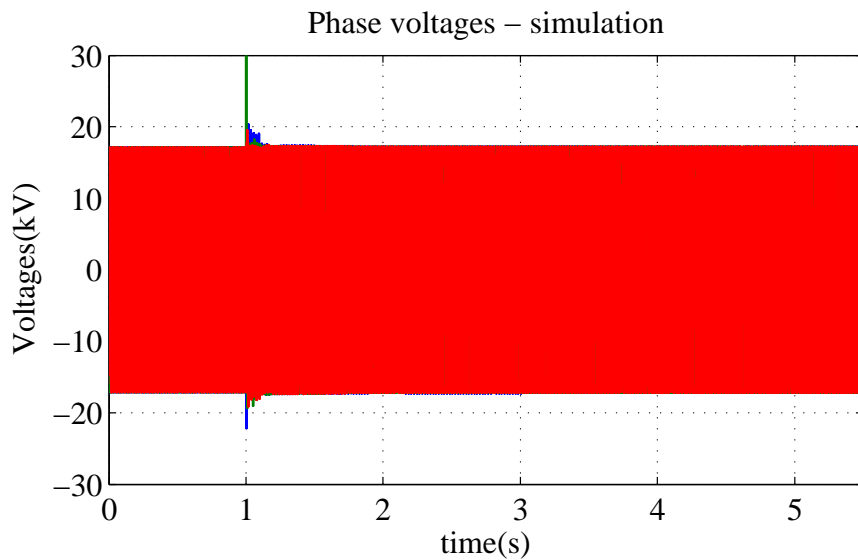


Figure 4.10: Phase voltages during energizing - simulation

During the energizing of the cable and the transformers the positive sequence voltage drops. After the cable has been energized, the voltage rises slightly due to the reactive power generated by the cable capacitance. The initial voltage drop of the positive sequence voltage and the voltage rise after the cable is energized can be seen on Fig. 4.12

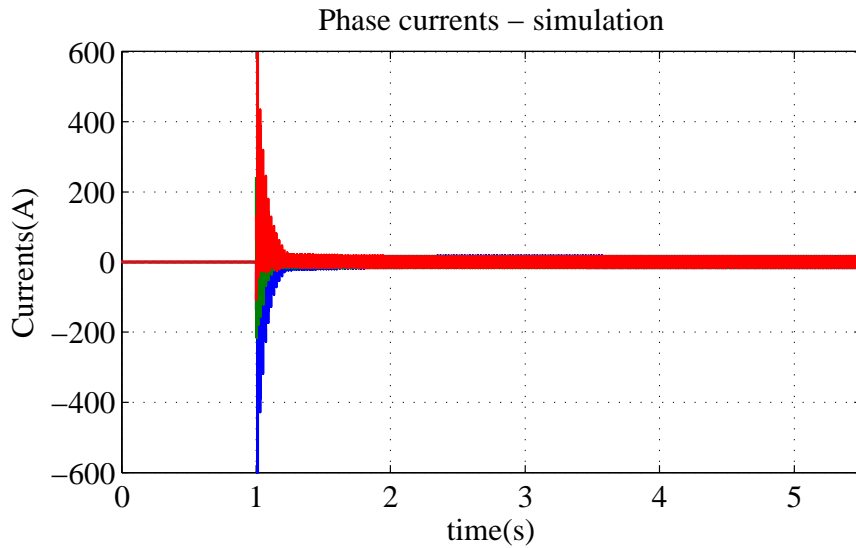


Figure 4.11: Phase currents during energizing - simulation

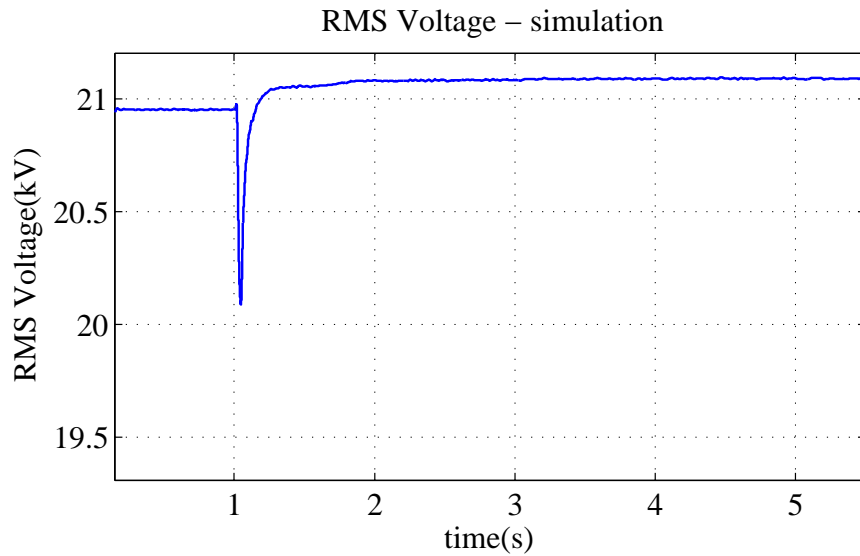


Figure 4.12: Voltage level when cable is energized - simulation

A zoom of the voltages and currents are shown in Fig. 4.13 and Fig. 4.14

In these figures the resonance frequency is 600Hz and matches the calculated resonance frequency.

In the very beginning of the transient, between the time instants of $t = 0.0065\text{ s}$ and $t = 0.012\text{ s}$, the current transient caused by the cable energizing can be seen in Fig. 4.14. After the cable is energized the transformer becomes heavily saturated producing strongly distorted and very high currents with the peak value of about 600 A .

The measured resonance frequency in the PSCAD/EMTDC simulations varies between 555 Hz and 593 Hz depending on the cable model. This is in agreement with the calculated resonance frequency given by (4.1).

The frequency of the transient is much higher than the power frequency and the damping

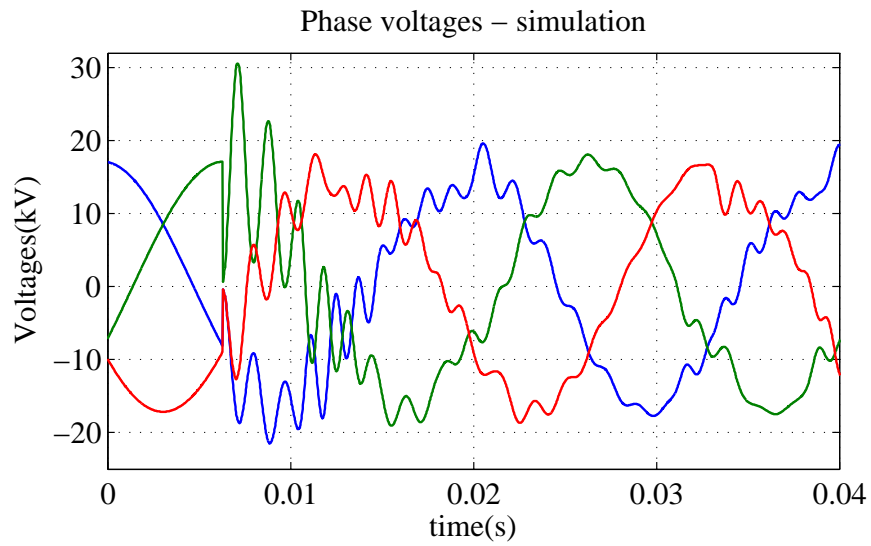


Figure 4.13: Phase voltages during transient - simulation

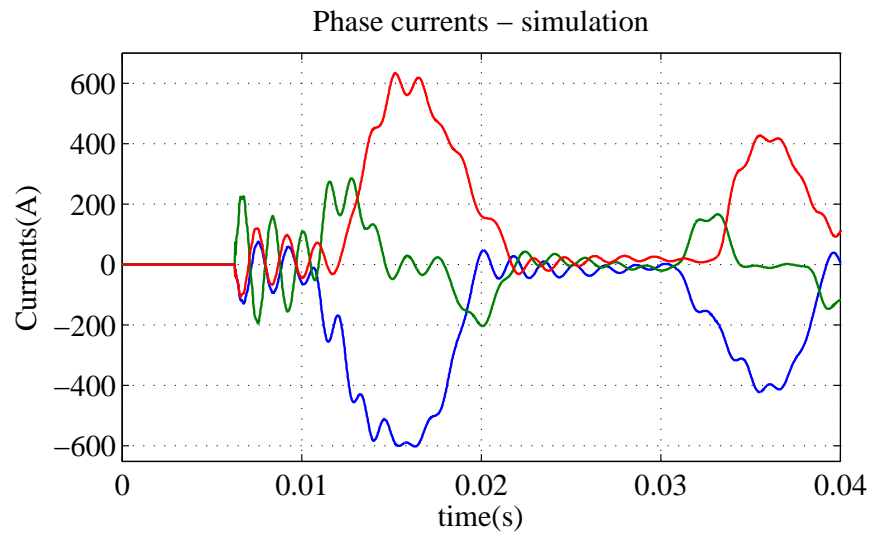


Figure 4.14: Phase currents during transient - simulation

is effected by skin effect. The increased damping due to the skin effect is modeled for the cable model and the transformers while for the grid the skin effect is neglected.

4.2 The Cable Lab

A cable lab for the transient analysis studies is built in the facilities of ABB Corporate Research in Västerås, Sweden. The cable lab is built with the purpose to replicate a feeder/turbine system found in the wind farms for the fast transient studies. The benefits of the lab measurements compared to the measurements in the field are many. The lab is built in a way so it enables reconfiguration of the test setup so it can replicate various wind turbine and feeder connection arrangements. Furthermore, various protection measures can be tested and compared in an environment that provides a good platform for the comparison of the protective devices.

4.2.1 Layout of the Three Phase Test Setup

The cable lab is a three phase setup thus allowing for the full scale tests for the purpose of the transient analysis studies. The setup of the cable lab consists of 550m long 20kV XLPE three core cable with 240mm² cross section of conductor, 52m long 20kV XLPE single core cable with the same conductor cross section, two transformers where transformer TX1 represents the transformer placed in the wind turbine while transformer TX2 represents the platform transformer. As a switching device, a vacuum circuit breaker is used. The full test setup is presented in Fig. 4.15

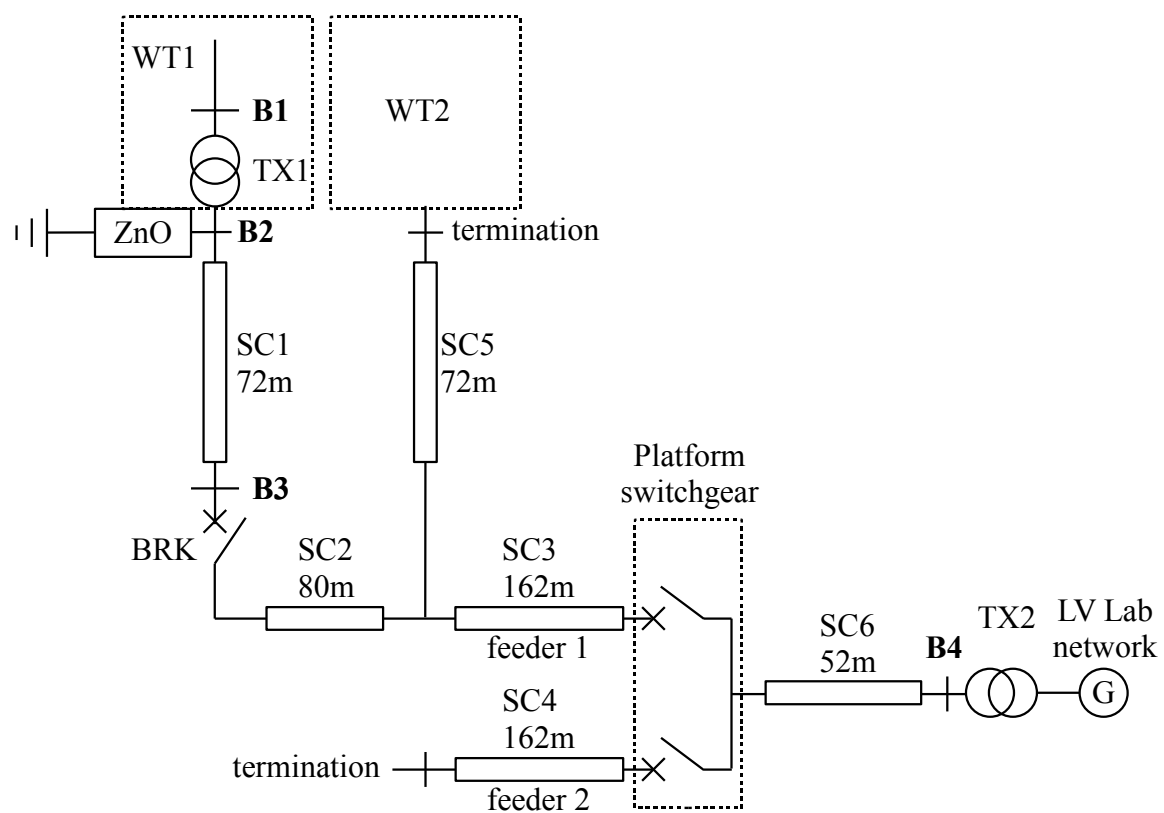


Figure 4.15: The cable lab setup layout

The setup is built so it may provide different connection arrangements found in real wind parks. Cables marked as SC1 and SC5 with $72m$ of length, represent the cable in the wind turbine which is placed between the wind turbine transformer (TX1) and the breaker (BRK). Cable SC5 is terminated at the other end, and in the test setup represents a disconnected wind turbine. This is very suitable for the analysis of the wave reflection and its impact on the high frequency transients. The SC2 cable is a cable which connects two turbines. The length of the cable is a bit too short compared to the cable between two wind turbines in a real wind park collection grid, but still its length is sufficient for the high frequency transient analysis. Cables SC3 and SC4 represent two feeders of the WP collection grid with the length of $162m$. "Feeder 2" or SC4 cable is terminated at the end, and represents a feeder with all wind turbines disconnected. The setup allows to have this feeder both connected or disconnected. When connected, Feeder 2 adds additional capacitance to the system and reflection point at its end where is terminated. The switchgear platform is connected to the platform using a single phase $52m$ long $20kV$ XLPE cable. On the platform, TX2 transformer is placed and it is connected to the grid from the low voltage (LV) lab network. Since both TX1 and TX2 transformers are connected in delta arrangement on the high voltage side, an artificial neutral point is provided using three $24kV$ rated voltage transformers connected with their primary windings connected in wye. During the inductive load test, an inductor with $0.318mH$ inductance is placed at bus **B1**

Transformer TX1 is protected with a surge arrester consisting of two ZnO blocks connected in series in order to prevent overvoltages of very high magnitude that can damage the transformer. The low voltage level supplied from the lab network is set to give $12kV$ voltage level on the high voltage side of the transformer TX2. The voltage is set to $12kV$ since the voltage rating of vacuum circuit breaker used in the testing is also $12kV$.

The rating of the equipment installed in the cable lab is as follows:

- $550m$ of $20kV$ XLPE three core cable with $240mm^2$ cross section of conductor;
- $52m$ of $20kV$ XLPE single core cable with the same conductor cross section;
- Transformer TX1, $20.5/0.41kV/kV$, $1.25MVA$, Dyn11 $Z_k = 5.4\%$;
- Transformer TX2, $20/0.69kV/kV$, $1MVA$, Dyn11 $Z_k = 5.1\%$;
- Breaker rated at $12kV$, $3.15kA$.

In the lab, various different protection devices are tested. As mentioned before, during the tests, transformer TX1 is always protected using a ZnO surge arrester in order to prevent damage to the transformers. For the transient studies, the RC protection and surge capacitor protection using different connection arrangements is tested. During the tests, the following surge protection is used:

- Two blocks of ZnO connected in series with continuous operating voltage $COV = 14.3kV$, with characteristic points of $1mA@17.2kV$ and $10kA@28.5kV$;
- Surge capacitors with $83nF$ and $130nF$ capacitance;
- Resistors with 20Ω and 30Ω resistance.

During the tests, different protection schemes are tested. In some cases different protection devices were placed at two buses at the same time in order to find the best solution.

4.2.2 Measurement Setup

In Fig. 4.16 the measurement setup is presented. Measurements are performed at buses **B2** and **B3**, where **B2** is the bus where the high voltage side of transformer TX1 is connected and **B3** is the bus at the breaker where cable SC1 which represents the wind turbine cable is connected.

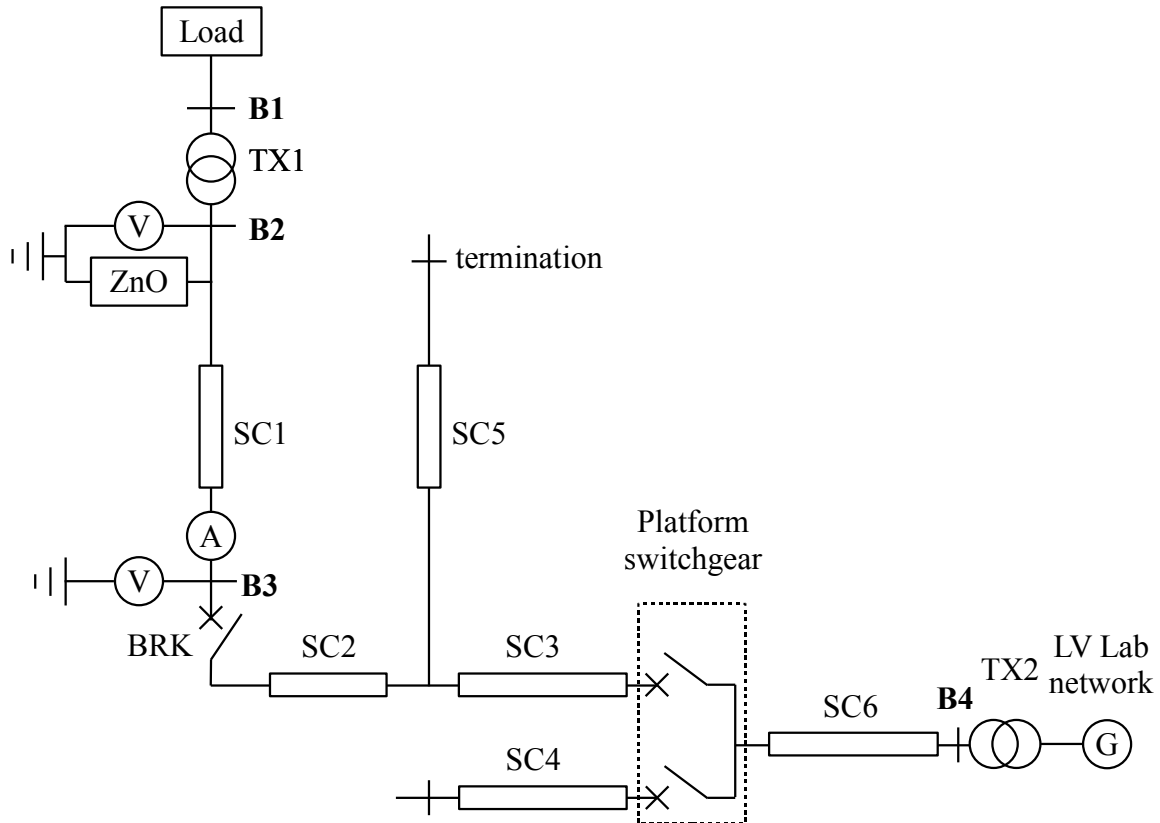


Figure 4.16: The cable lab measurement setup layout

On the bus **B2**, only the voltage is measured. It is of the highest importance to measure this voltage with good accuracy since the voltage measured at this bus is the voltage that stresses the insulation of transformer TX1. On the bus **B3** both current and the voltage are measured. Since this is the bus where the breaker is connected, the measured current represents the current through the breaker which is important to study the breaker phenomena. By measurement of voltages at these two buses it is possible to observe the wave traveling and reflection phenomenon which creates high frequency transient overvoltages.

Since the high frequency phenomenon is measured, measurement equipment with high bandwidth is used. For measurement of voltages at bus **B2**, Northstar voltage dividers Type VD-100 are used. The accuracy of these voltage dividers is 1% in frequency range between $10Hz - 1MHz$ while at frequency range between $1MHz - 20MHz$ it is 3% and

the divider ratio is 10000 : 1. At bus **B3** HILO Type HVT40RCR voltage dividers are used. The bandwidth of these dividers is 10MHz while the ratio is 2500 : 1. For the current measurement at **B3**, Pearson current monitor type D101 is installed. The bandwidth of this current probe is 4MHz with maximum peak current of 50kA.

The Signals from voltage dividers and current probes are lead by optical link to two transient recorders type TRA 800s. By using optical links it is ensured that the measured signal is not disturbed. Nine channels in total are recorded at the sampling rate of 20MHz using 12 bit resolution.

4.2.3 Measurement Results and Analysis

In this section, the results obtained during the measurements and the simulation results are compared and analyzed. The purpose of the analysis is to verify the model developed for simulation of the high frequency transients and to study the impact of mitigation methods on the high frequency transient.

The system model is built using the component models developed as described in Section 3. The parameter estimation of the components is based on the measurements for the base case. The base case is the case with only surge arresters connected to the system. The results obtained using the transient mitigation equipment are compared to the base case and the influence of the different mitigation devices is studied.

Since the results depend on many parameters, the worst case scenario is always chosen. This report does not estimate the risk of obtaining the worst case, but considering the projected life time of the transformers and the number of the breaker operation during such a period, the worst case scenario will most likely occur during the transformer life time.

When it comes to the worst case scenario, it is important to note that the characteristics of a high-frequency transient such as the magnitude of the voltage surge and the number of strikes depend on the arcing time (arcing angle) of the breaker, or the time that passes from the start of the contact separation until the power frequency current zero crossing. The arcing time is essential for the appearance of the reignitions in the system. If the reignitions are to be avoided, the point-on-wave control can control the breaker in such a way so the high frequency transients are avoided. On the other hand, to make sure that the worst case scenario is investigated during the test and the simulation, the arcing time of the breaker for all cases of the breaker opening operation is chosen so the breaker starts the separation of the contacts at the very instant when the current in one of the phases just passes the current chopping level. This gives that the dielectric withstand of the breaker is at its minimum when the breaker interrupts the current, thus producing reignitions very shortly after the current interruption. This case produces voltage escalations with the maximum voltage level and therefore this is the worst case scenario for the breaker opening operation. The exception is the no-load case when the current never reaches the chopping level. In this case, the contacts of the breaker start separating when the current is at its maximum. This gives the fastest rate of rise of the transient recovery voltage since it is directly proportional on the level of the chopped current.

For the closing operation of the breaker, the worst case scenario which produces the highest magnitude of the surge voltage is when the dielectric withstand of the gap reaches

the phase voltage when it is at its maximum. In this case, the voltage surges of the highest magnitude are generated.

Since the voltage breakdown, the current chopping and the high frequency current interruption are the stochastic phenomena and very much determine the results presented in the time-domain, the exact replication of the measurement results using simulations is not possible. This is especially the case for the opening of the breaker, where larger number of the stochastic strikes appears. Therefore, the verification of the simulation models is performed by verifying the following characteristics of the high frequency transient:

- The appearance of repetitive strikes;
- The highest magnitude of the surge voltage;
- The rise time of the surge created during the strike.

Furthermore, the obtained results are compared to standard values of the basic lightning impulse voltage level (BIL). The results obtained in this section are measured at a non-standard voltage level which is set below the rated voltage of the transformers, cables and other equipment. This is performed in order to avoid damages on the equipment used for testing since the simulations showed that transient overvoltages of very high magnitudes are expected during some tests.

The standards for both dry-type and oil filled transformers define for each voltage level the BIL at which the transformer will not show any signs of insulation damages. These voltage impulse tests are considered as the highest stress that can happen to insulation of a transformer and therefore, if the transformer is able to withstand this voltage without any problems, its insulation will most probably survive other high frequency transients.

The BIL defined by standards for dry-type and oil-impregnated transformers is given in Table 4.1.

Table 4.1: Nominal system voltage and basic lightning impulse insulation levels (BIL) for dry-type and oil-filled transformers [59],[60]

	BIL (kV)	45	60	75	95	110	125	150	200
U_{nom}									
8.7 (DT)		S	1		1				
15 (DT)			S		1	1			
24 (DT)					2	S	1	1	
34.5 (DT)							2	S	1
8.7			S						
15				S					
24								S	
34.5									S

Where S is referred as the standard value, 1 as an optional higher level where the transformer is exposed to high overvoltages, 2 as the case where surge arresters are used and found to provide appropriate surge protection and DT as the dry-type transformer.

This data is used for comparison with strikes obtained by measurements and simulations. For the presentation of the voltage strikes in the scatter plots, the magnitudes of the voltage strikes are shown in per unit, where $1pu$ presents the nominal voltage of the transformer. This is done because, the maximum magnitudes of the voltage strikes obtained at any voltage level with properly calculated surge arresters is the same when presented in per unit. However, the BIL for each voltage level has a different value when expressed in pu making a comparison difficult. For example, for the $8.7kV$ level, the basic lightning insulation level is $5.2pu$ for dry-type transformers and $8.6pu$ for oil insulated transformers while for the $34.5kV$ level the BIL values are $3.6pu$ (with surge arrester used) and $5.8pu$ respectively. For this reason, the minimum value in per unit is used as the reference value for the dry-type and the oil insulated transformers. The comparison is done for both standards since the magnitude of the voltage strikes is the same for both dry-type and oil insulated transformers and the difference is only in the rise time of the surge.

To obtain the data for the scatter plots, a signal characterization method is utilized to obtain the magnitude of strikes and its rise times as its important characteristics [61]. In the scatter plots, these transient voltage characteristics are compared to the BIL voltage. As a consequence, the inspection of the transient voltages is simplified and it is easy to notice if the strikes during the transient exceed the rise time and/or the magnitude of BIL. A plot showing the transient overvoltage and the detection of strikes is presented in Fig. 4.17.

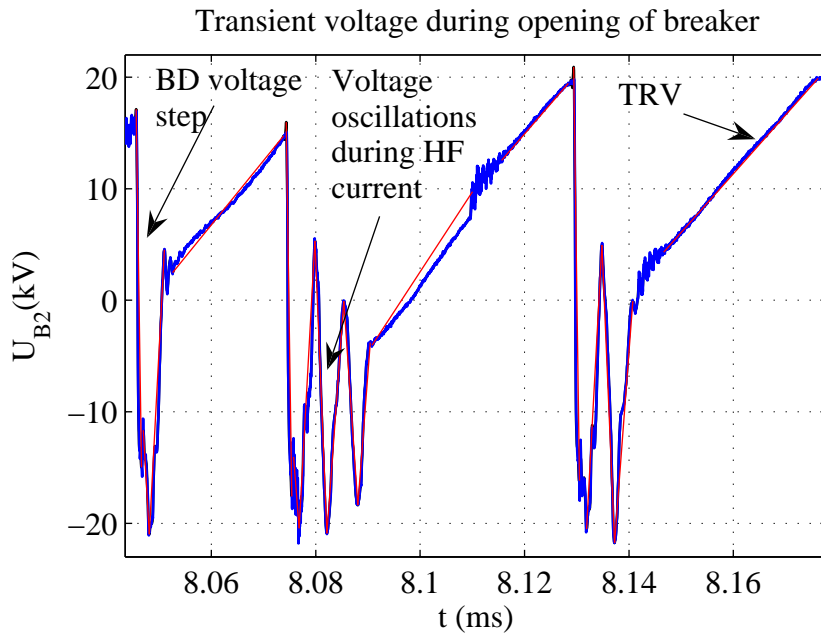


Figure 4.17: Characteristic voltage steps during transient

As it can be noted, voltage steps of different slopes are generated during the transient. The steepest voltage slope is generated right after the voltage breakdown in the vacuum. The stepness of this voltage is determined by the surge impedance of the cable and the stray capacitance of the transformer, yielding a very steep voltage front with the rise time t_{rise} in the order of $0.5\mu s$. Observing Fig. 4.18 it can be seen that these voltage steps belong to the first group of the fastest transients.

Right after the breakdown, the high frequency current generates voltage fronts with rise times t_{rise} in order of $2\mu s$ giving the oscillation frequency of $500kHz$ approximately. These

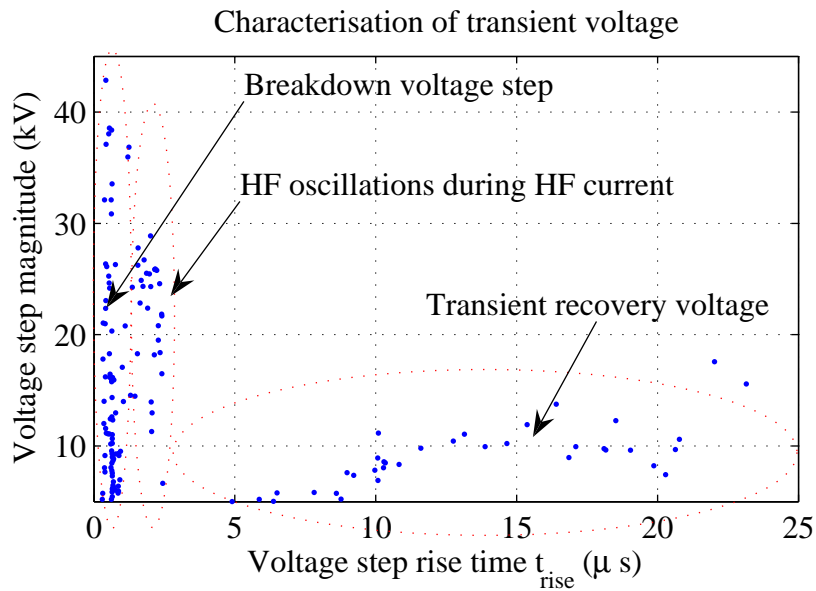


Figure 4.18: Characterization of transient voltage - scatter plot

voltage steps are placed in the second group of voltage steps and can be easily separated by visual inspection in Fig. 4.18.

The voltage steps with the highest rise time represent the transient recovery voltage which occurs during the period of time when the arc is interrupted. Since the rate of rise of the transient voltage is almost constant, it can be observed that the longer the rise time, the higher the magnitude of the voltage step.

Figs. 4.17 and 4.18 give a simple and clear insight how the characterization data can be observed and interpreted. Scatter plots, as one shown Fig. 4.18, will be used to present results and to compare the simulation and the measurement data to BIL.

Estimation of Breaker Parameters

To obtain the breaker parameters, the voltage over the breaker is not directly measured. Instead, only the voltage on one side of the breaker is measured along with the current through the breaker. The dielectric withstand over the breaker during the very short period of time can be estimated by measuring the voltage right before the breakdown and right after the breakdown. Since the voltage changes much quicker compared to the speed of the contact separation, the voltage over the breaker can be determined very accurately. This is displayed in Fig. 4.19

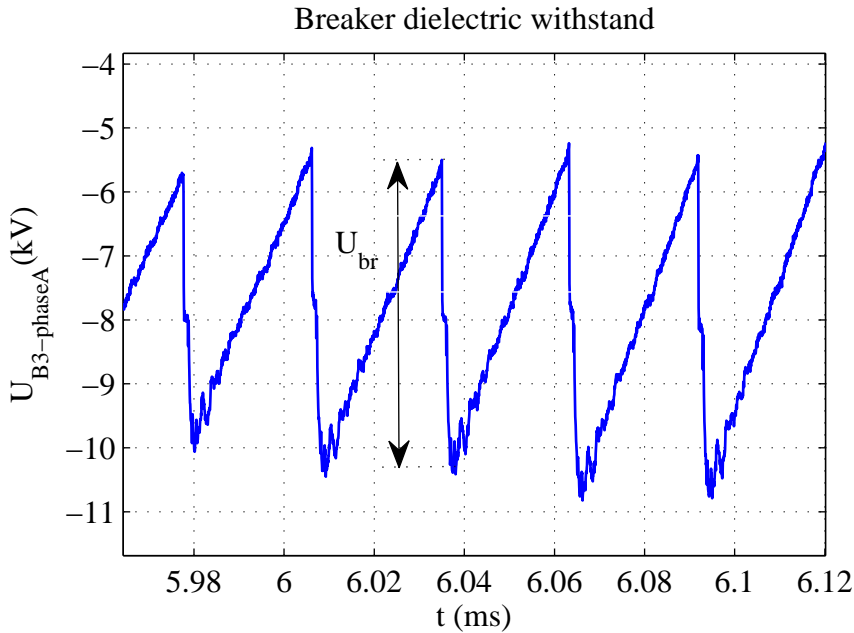


Figure 4.19: Voltage at breaker

The high frequency current quenching capability will be calculated from the plots which show the current through the breaker, and it is a straight forward procedure to determine the high frequency current quenching capability or the ability to interrupt the high frequency current.

Breaker Dielectric Withstand The dielectric withstand of the breaker is a very important parameter for the analysis of switching transients. During the operation of the breaker, when prestrikes and restrikes occur, it is of highest importance to properly model the dielectric withstand capability of the breaker. During the initial separation of contacts, the dielectric withstand starts increasing from an initial dielectric withstand with value varying from $0.69kV$ to $3.4kV$ [26] depending on the breaker. In the published literature, the dielectric withstand of the breaker increases linearly with a constant speed [24]. However, the voltage plots obtained during the measurements show that the speed of the contacts in the breaker increases during the operation and cannot thus be modeled using a straight line with the slope that represents the speed of the contact separation.

To model the dielectric withstand characteristics of the breaker, a simplified mechanical model of the breaker is analyzed. This system is shown in Fig. 4.20

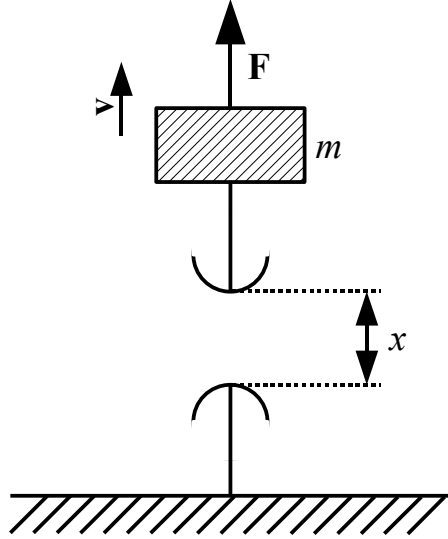


Figure 4.20: Representation of the breakers mechanical system

For this analysis, the force that separate the breaker contacts is assumed to be constant. This gives that the breaker contacts are constantly accelerated yielding that the speed of the contact separation is linearly increasing and not remaining constant as stated in the literature. This gives that the speed of the constant separation \mathbf{v} and the distance between contacts \mathbf{x} are given as

$$\begin{aligned} \mathbf{v} &= \mathbf{v}_0 + at = \mathbf{v}_0 + \frac{\mathbf{F}}{m}t \\ x &= vt = v_0t + \frac{F}{m}t^2. \end{aligned} \quad (4.2)$$

Since the initial speed of the breaker contacts is equal to zero, the final expression for the distance between contacts is given by

$$x = \frac{F}{m}t^2. \quad (4.3)$$

If we take that that the dielectric withstand between contacts as the function of distance is proportional to the distance (this is true for small distances) we can write

$$V_{br} = Cx + V_0 = C\frac{F}{m}t^2 + V_0. \quad (4.4)$$

Since the constants C , F and m are unknown and it is difficult to obtain them, this analysis is used just to describe the behavior of the dielectric withstand of the breaker during the breaker operation. To obtain the accurate dielectric withstand curve of the breaker, the dielectric withstand of the breaker is analyzed during the opening and the closing of the breaker. The opening of the breaker is presented in Fig. 4.21.

From Fig. 4.21 it can be observed that the dielectric withstand of the breaker is not linear, and for that reason, it is going to be approximated using the second order polynomial. In order to define the dielectric withstand curve by the second order polynomial given by

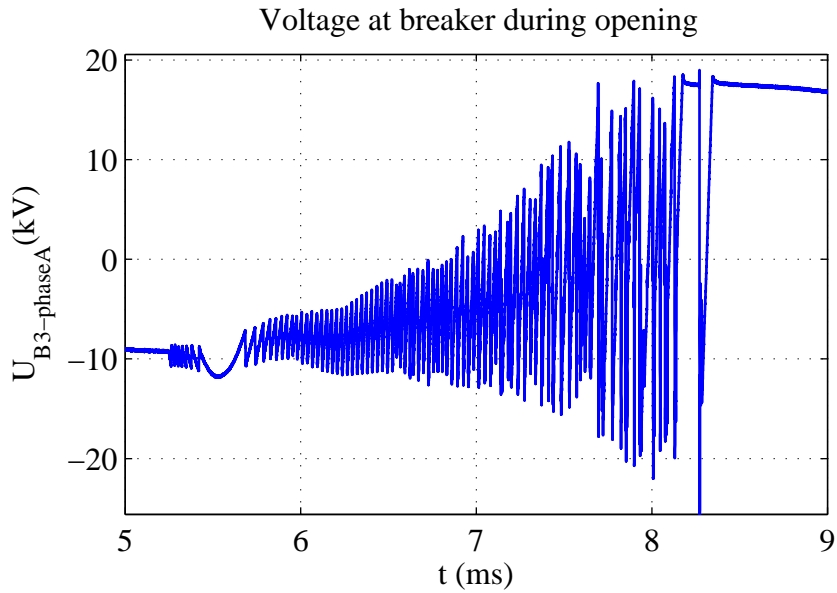


Figure 4.21: Voltage at breaker during opening - inductive load

$$V_{br} = at^2 + bt + c \quad (4.5)$$

where parameters a , b and c have to be calculated. In order to do that, the rate of rise of the dielectric withstand is calculated from the plot obtained by measurements in the beginning of the opening operation and approximately $2ms$ after. The value of the c parameter is equal to the dielectric withstand in the very beginning of the opening operation.

This is shown in Figs. 4.22 and 4.23

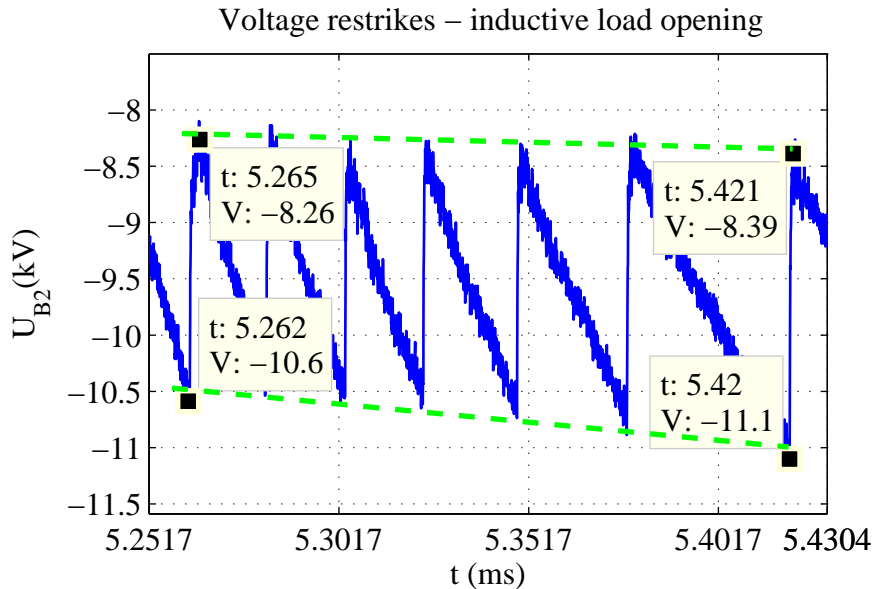


Figure 4.22: Calculation of c parameter and rate of rise of V_{br} at beginning of opening

In the breaker model, the stochastic nature of the breaker is neglected and the calculated dielectric withstand of the breaker represents its mean value. Whenever the voltage over

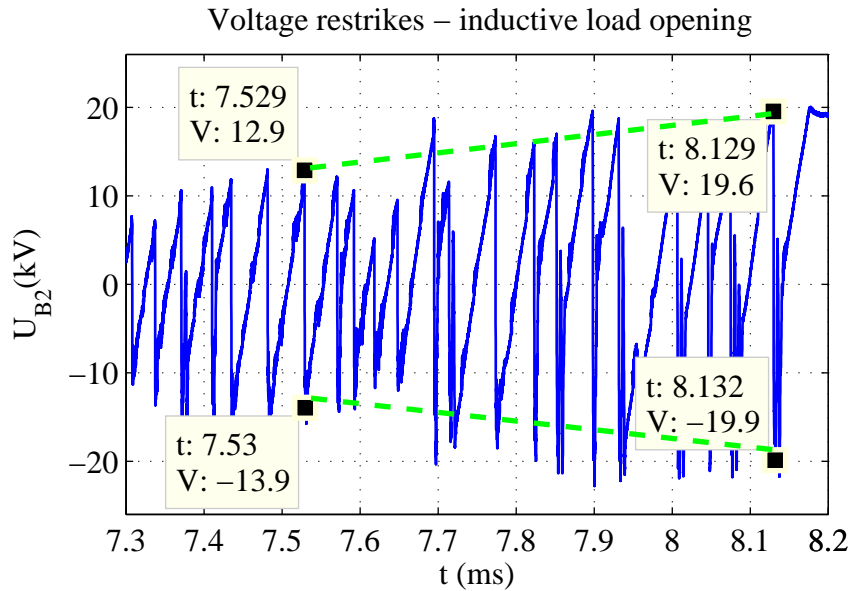


Figure 4.23: Rate of rise of V_{br} 2.2ms after beginning of opening

the breaker is equal or greater than the dielectric withstand, the breakdown occurs and the breaker conducts the current. Using the measurement data obtained at the breaker opening event, the mean value of the breaker dielectric withstand can be written as

$$V_{br} = 5.25e9t^2 + 4.15e6t + 1200. \quad (4.6)$$

During the closing operation, the breaker contacts reach very high speed, and the acceleration of the contacts cannot be observed. To model the dielectric withstand curve of the breaker during the closing operation, it is more convenient to use the constant speed approach. In Fig. 4.24 it can be observed that the speed of contacts is very high and therefore it can be considered as linear.

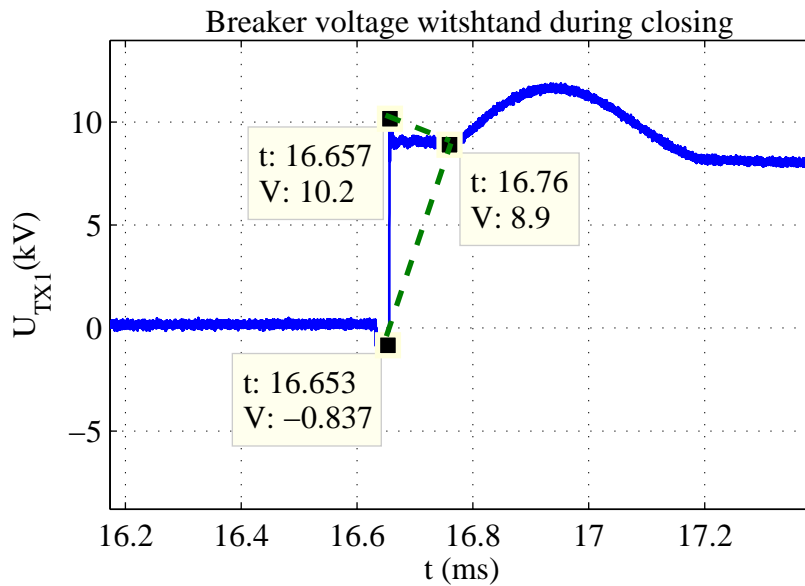


Figure 4.24: Breaker dielectric withstand at closing

At the time instant of $t = 16.653ms$ a prestrike occurs. When this happens, the cable is charged and the current is interrupted immediately after. For that reason, the voltage remains constant until the time instant of $t = 16.76ms$ when the contacts are finally closed. The closing speed of the contacts varies between $45kV/ms$ and $65kV/ms$ and in this case the speed of $50kV/ms$ is recorded.

Interruption of the high frequency current The high frequency current quenching capability of the breaker can be modeled using two different approaches. This is stochastic phenomenon as well as the voltage breakdown in the breaker, but for the breaker model used in the simulations only the mean value is calculated and the stochastic nature of the phenomenon is neglected. Furthermore, the mean value of the high frequency current quenching capability is taken to be constant as suggested in [27]. These assumptions significantly simplify the calculation of the derivative of the high frequency current di/dt at which the breaker is not capable to interrupt the high frequency current when crossing the zero value.

In Fig. 4.25 it can be observed that while the peak of the high frequency current and its derivative which is directly proportional to it are low, the breaker is capable of breaking the high frequency current almost at every zero crossing.

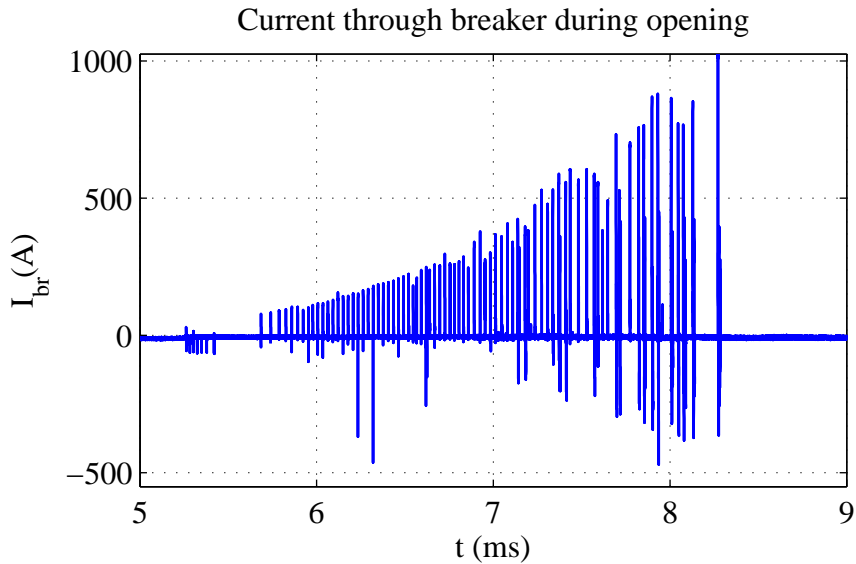


Figure 4.25: Current through breaker at opening

To obtain the value of di/dt at which the breaker is not able to interrupt the high frequency current at the zero crossing, the current graph showed in Fig. 4.25 is zoomed showing the current at the time interval between $8.128ms$ and $8.143ms$, which is presented in Fig. 4.26.

In Fig. 4.26 it can be observed that the breaker did not manage to interrupt the high frequency current with $di/dt = 350A/\mu s$. The high frequency current is interrupted only when the value of di/dt is equal or lower to $250A/\mu s$. For the simulations, the value of di/dt parameter is set to $350A/\mu s$.

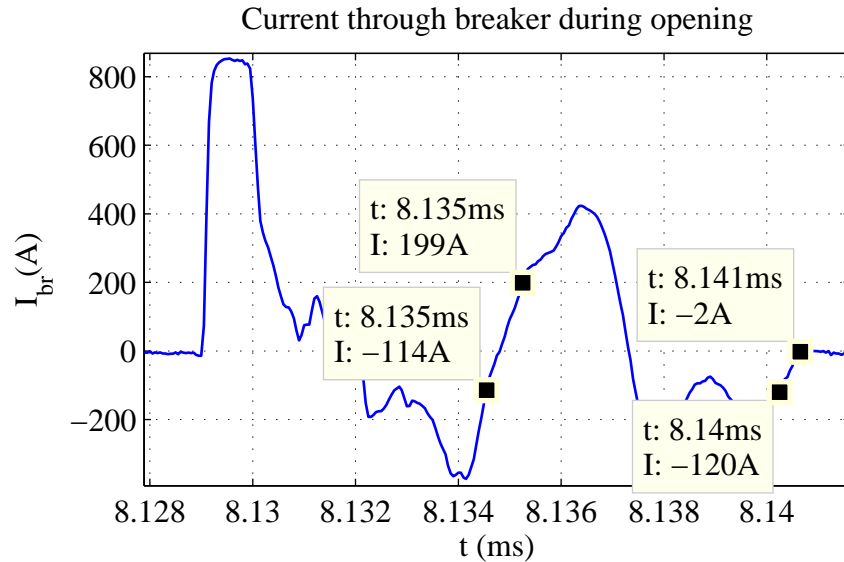


Figure 4.26: Interruption of high frequency current at zero crossing

Base Case Results

As mentioned before, the case with only surge arresters connected to the transformer terminals is taken as the base case. The reason for having surge arresters connected all the time is just a precaution in order to avoid any damage to the transformers during testing. However, a simulation case without any surge protection devices is presented to illustrate the magnitude of the generated surges. This case is simulated only for the opening operation of the breaker since the highest magnitudes of surges are obtained during reignitions due to the voltage escalation.

No-load case The no-load case is performed for both closing and opening operation of the breaker with the surge arrester connected to the transformer terminals. The scheme that presents this case is shown in Fig. 4.27.

During the closing operation of the breaker, the prestrikes are expected to occur. The prestrikes are generated at the time instants when the dielectric withstand of the gap between the breaker contacts is lower than the voltage over the gap. Therefore, the time instant to close the contacts is chosen so the dielectric withstand of the breaker reaches the voltage over the gap when its level is at the maximum.

As it can be noted from Fig. 4.28, the switching of the breaker does not occur exactly at the maximum voltage, but at the point very close to it. The reason for that is that during the experiment this margin was treated as sufficiently good, and therefore, the simulations are set for a similar switching time instant.

During the closing operation, voltage prestrikes occur in the system. The critical point for the verification of the model is to compare the rise time t_{rise} calculated analytically to the measurement and to the simulation. During the prestrike, the voltage surge is determined by the voltage level at which the voltage breakdown appears, and the time constant of the system. The time constant of the system is determined by the surge impedance of the cable

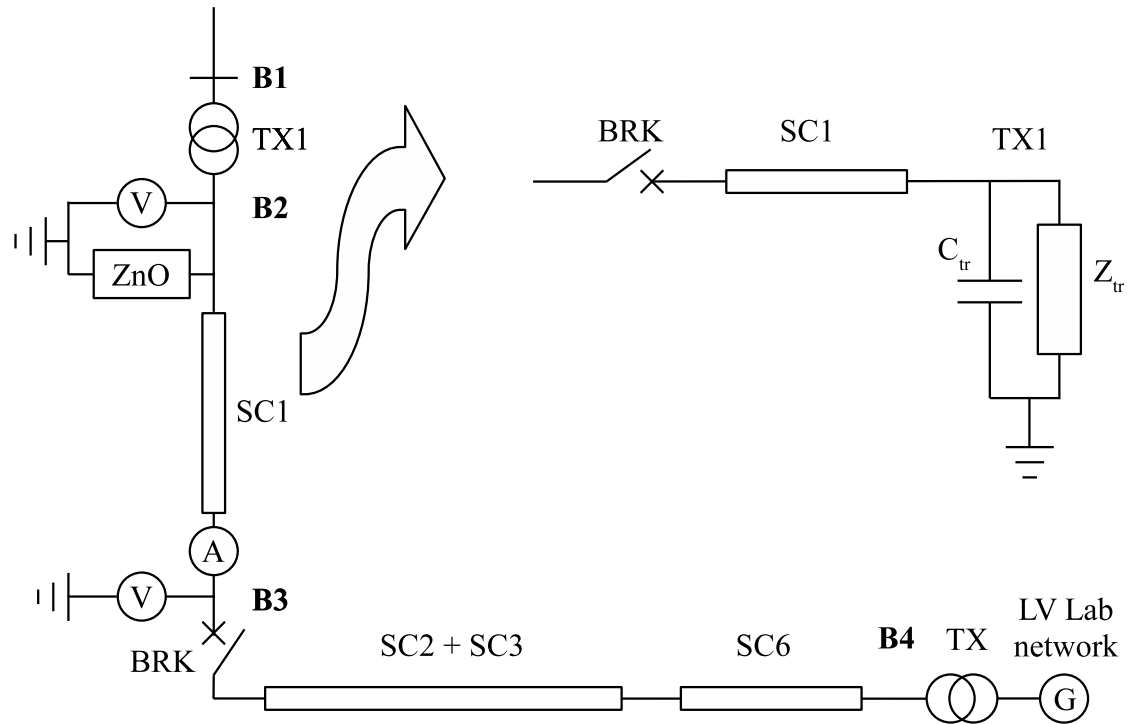


Figure 4.27: No-load case with surge arrester at TX1

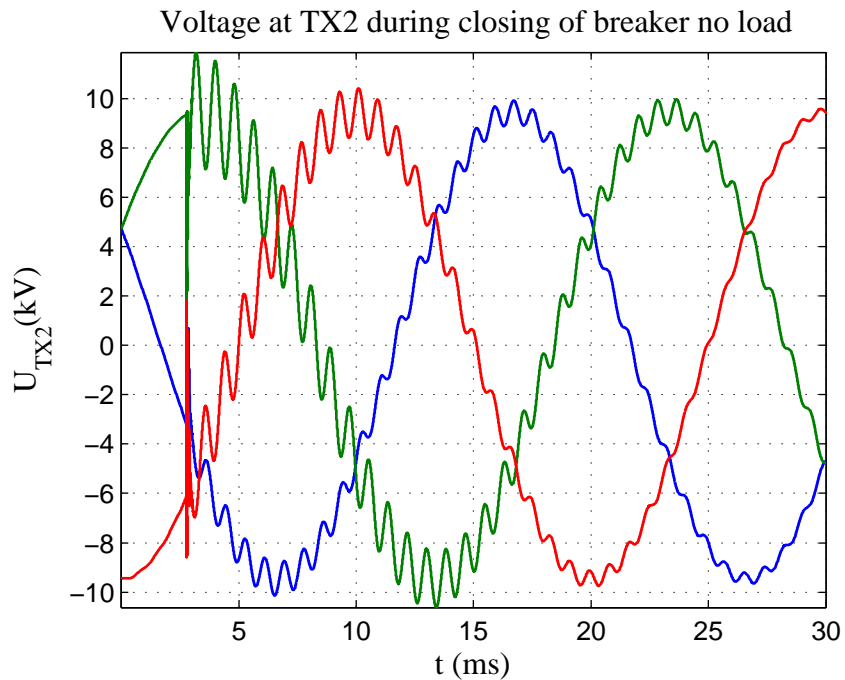


Figure 4.28: Voltage at TX2 during closing of breaker - simulation

Z_{cab} and the stray capacitance of the transformer C_{tr} and is given by

$$\begin{aligned}\tau &= Z_{cab}C_{tr} \\ t_{rise} &= 2.2\tau.\end{aligned}\tag{4.7}$$

During the measurement of the stray capacitances of the transformer, a stray capacitance of $8.5\mu F$ is measured. The transformer model consisting only of the stray capacitance and the surge impedance is presented in Fig. 4.29. The surge impedance of the cable is calculated to be 24.8Ω giving the analytically calculated $t_{rise} = 0.462\mu s$.

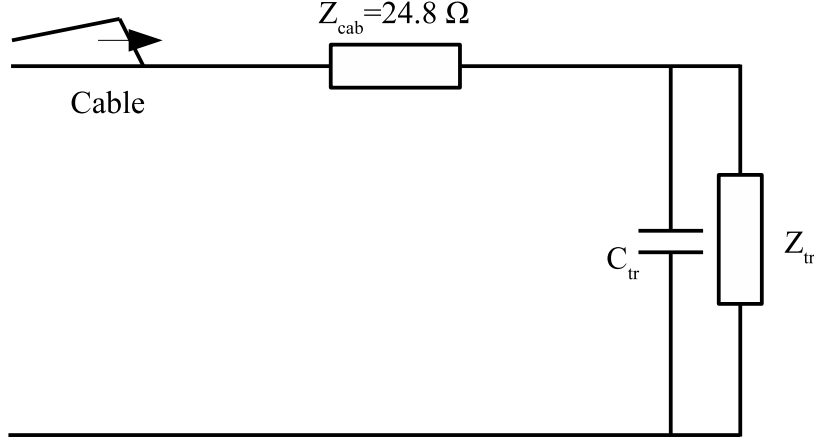


Figure 4.29: Cable/Transformer model for HF transient

When this result is compared to the measurement and the simulation, a very good agreement is observed. Due to the different voltage levels at the occurrence of the prestrike, the steady-state voltage levels in the plot are not identical. The ideal case is approximated using expression

$$V = V_0 \left(1 - e^{-\frac{t}{\tau}}\right)\tag{4.8}$$

where V_0 is the steady-state voltage level, and τ is the time constant given by (4.7). For the simulation case, this voltage is set at $9.3kV$, while it is for the simulation set to $10.1kV$.

In Fig. 4.30 it can be seen that the simulation result matches the measurement and the analytically calculated value. It shows that the transformer model gives good response for the high frequency transient.

To observe the response of the whole system, and the generation of the high frequency transients during the closing operation of the breaker, a whole time span which shows the closing cycle including the transient voltage from the very first prestrike until the contacts are closed is observed. This transient can be seen in Figs. 4.31 and 4.32.

As the contacts of the real breaker close at slightly different time instants compared to the simulation, the phase to phase comparison of the voltages in the time domain, obtained by the simulation and measurement is almost impossible. The simulation shows only one prestrike in each phase, while in the measurement it can be observed that another prestrike appears approximately $1ms$ after the first one. This happens due to the bouncing of the

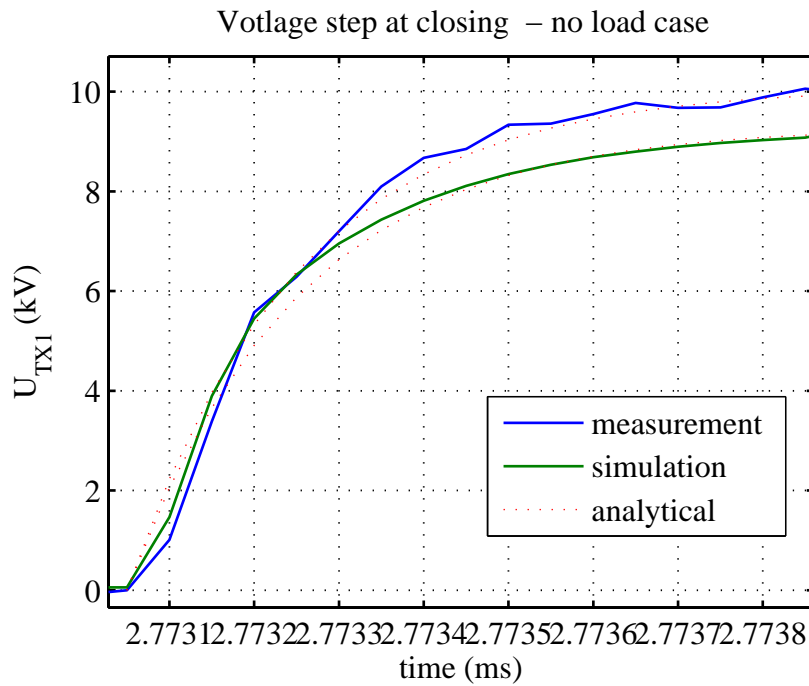


Figure 4.30: Voltage surge rise time

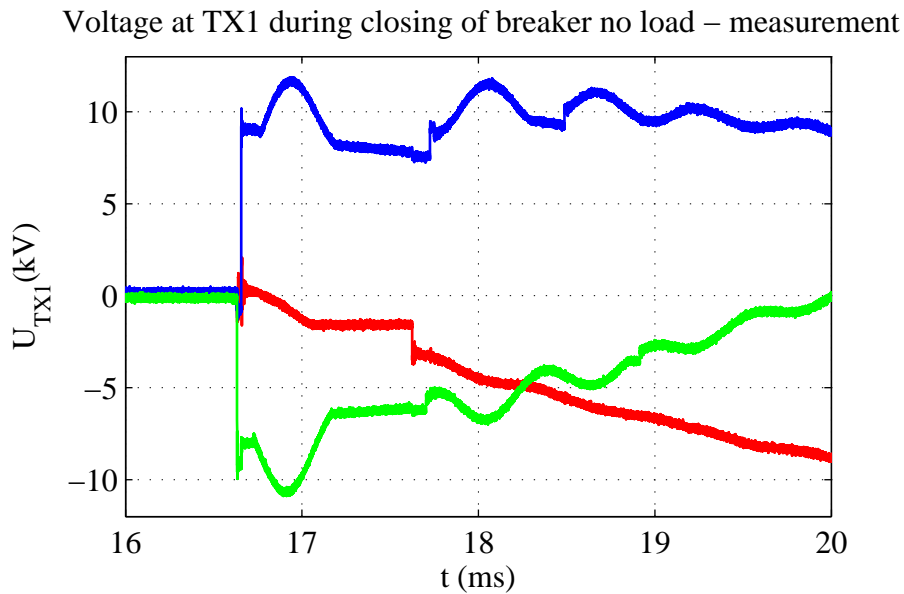


Figure 4.31: Transient voltage at TX1 during closing - no load - measurement

contacts of the breaker and it will be shown later more in detail. This phenomenon is not modeled since it does not play a significant role in generation of high magnitude surges.

Furthermore, the 900Hz oscillations that appear in the transient voltage are much better damped in the real system. This is expected since the transformer model and the grid model does not include modeling of the skin-effect phenomenon.

When the TOV characterization algorithm is applied, the magnitude and the rise time of the strikes are calculated. The results of the characterization of the transient can be seen in Figs. 4.33 and 4.34.

Voltage at TX1 during closing of breaker no load – simulation

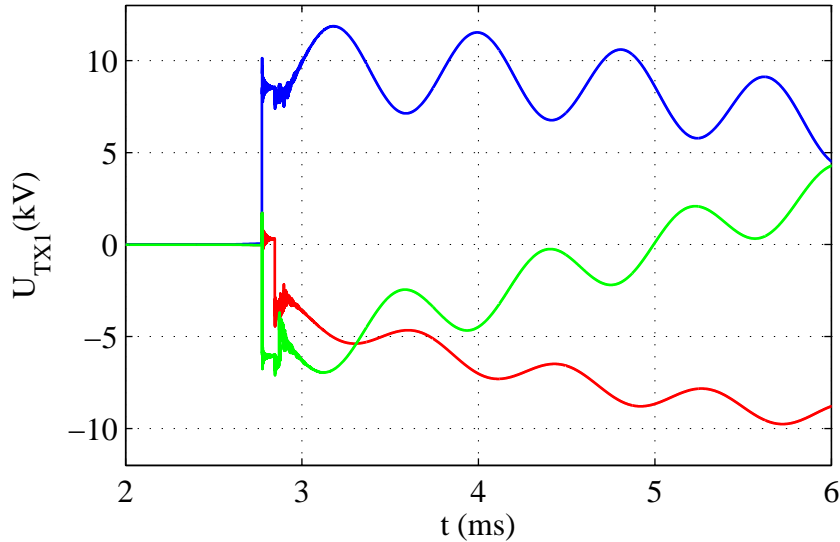


Figure 4.32: Transient voltage at TX1 during closing - no load - simulation

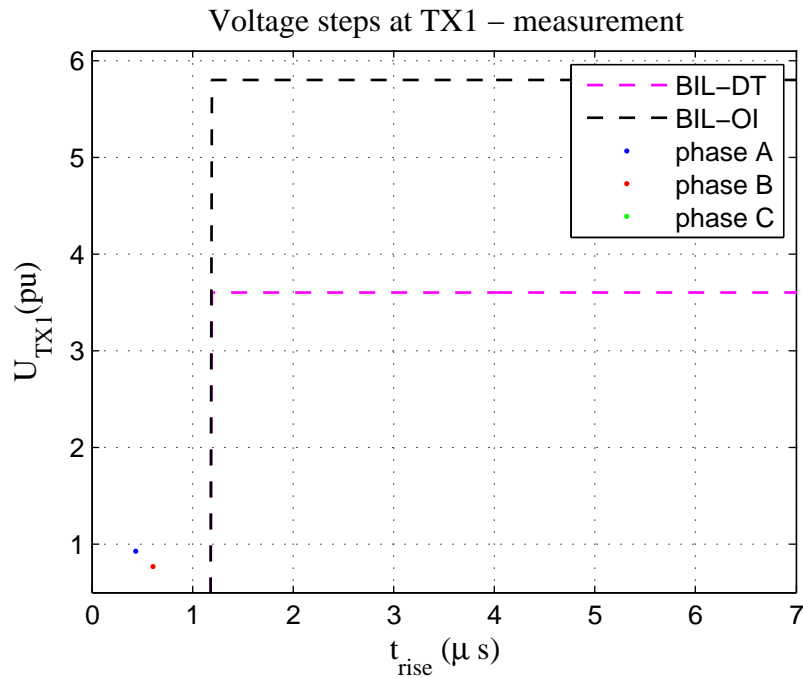


Figure 4.33: Strikes recorded during closing transient at no load - measurement

In Figs. 4.33 and 4.34 it can be observed that the magnitude of the transient and its rise time obtained by simulation are in good agreement with the measurement. BIL-DT and BIL-OI represent the BIL for dry-type and oil insulated transformers respectively. It is important to note that the magnitudes of surges are below $1pu$ and much below the BIL of the dry-type and oil insulated transformers. However, the rise time of these strikes is shorter than the BIL rise time of $1.2\mu s$. In the case of dry-type transformers, the rise time of the surge is approximately 10 times shorter than the rise time of the surge when the oil insulated transformer is used. This is due to a 10 times smaller stray capacitance of the dry-type transformers.

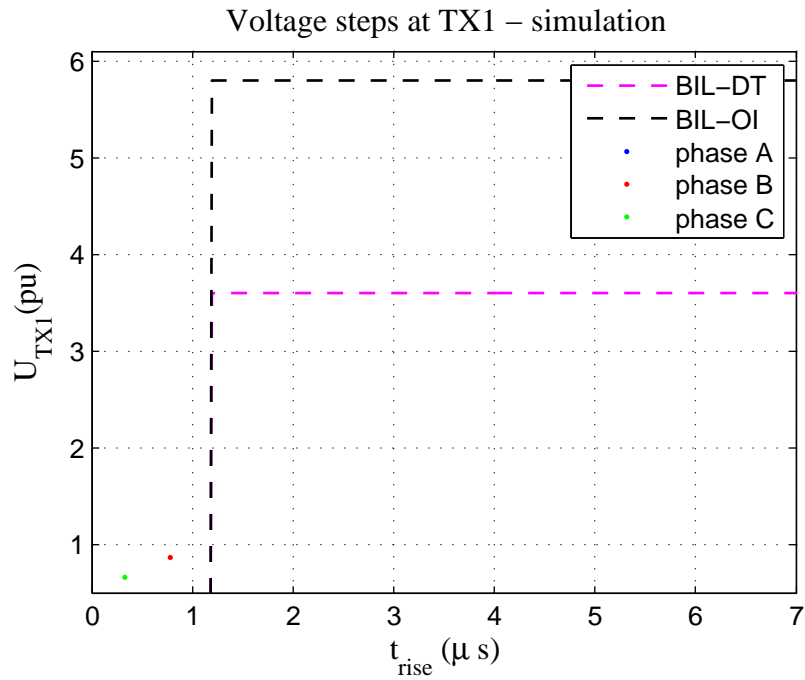


Figure 4.34: Strikes recorded during closing transient at no load - simulation

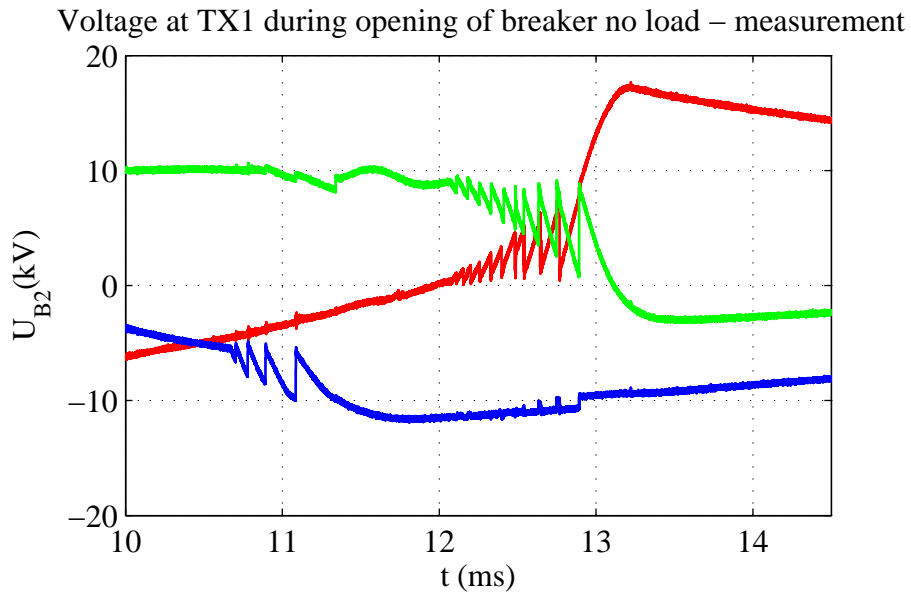


Figure 4.35: Transient voltage at TX1 during opening - no load - measurement

For the opening transient, it is expected to record a higher number of repetitive strikes. During the opening operation, at the time instant of the contact separation, the transformer magnetizing current is chopped and generates fast rising transient recovery voltage. As the contacts are separated with rate of rise of the dielectric withstand which is much slower than the rate of rise of the transient recovery voltage, a reignition quickly occurs. This is shown in Fig. 4.35 at $t = 10.6ms$ in the measurement plot and in Fig. 4.36 at $4ms$ in the simulation.

Furthermore, it is observed that the contacts start to open in phase A (blue curve) approximately $1.5ms$ before in other two phase. This time delay is stochastic and in the simulation it is set to $1ms$. The timing of the contact separation is critical to obtain a good

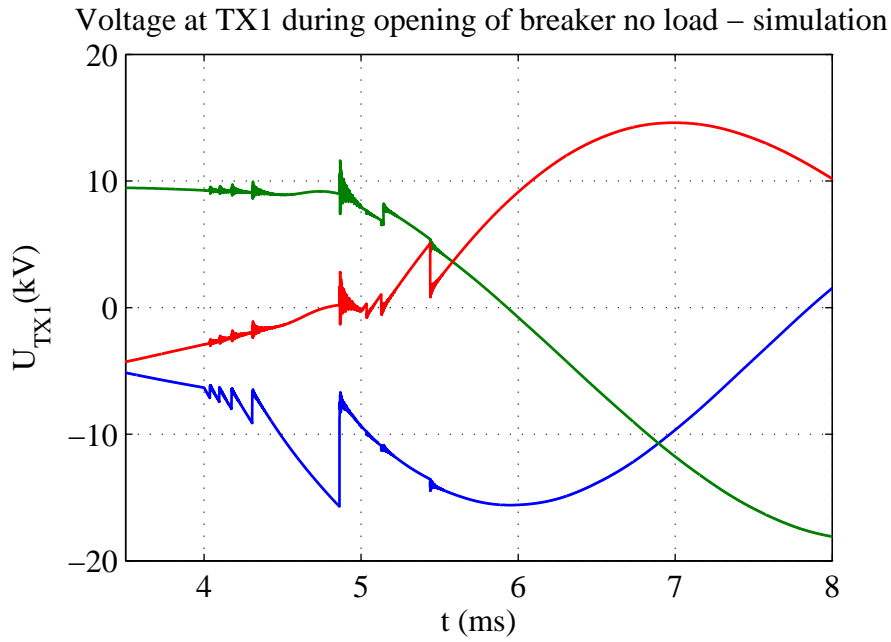


Figure 4.36: Transient voltage at TX1 during opening - no load - simulation

agreement since the rate of rise of the recovery voltage very soon after the contact separation becomes slower than the rate of rise of the dielectric withstand. Although the difference in the number of reignitions exists when the simulation is compared to the measurement, the repetitiveness of the strikes is confirmed both in the simulation and the measurements. The magnitude and the rise time of the highest strike obtained in the simulation is in agreement with the measurements which shows a good accuracy of the model.

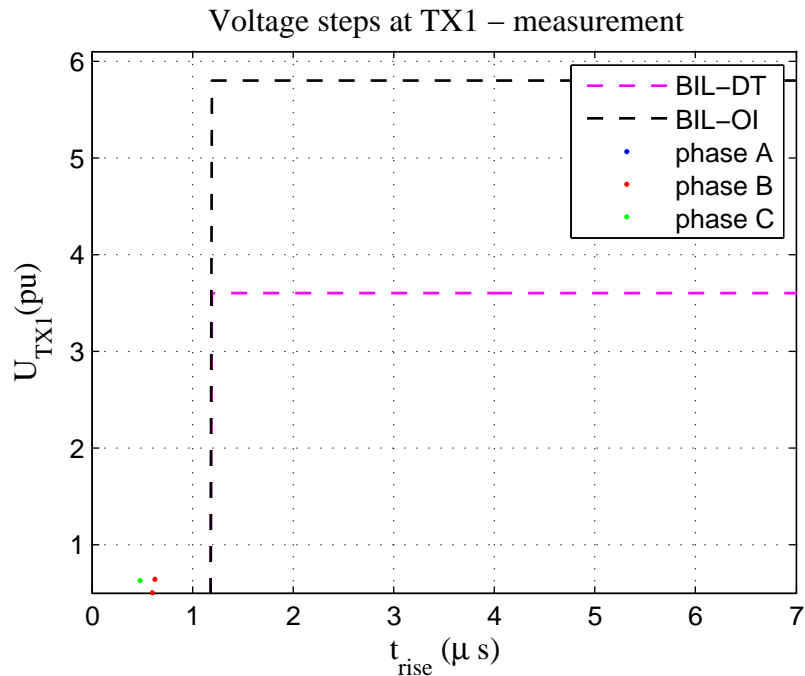


Figure 4.37: Strikes recorded during opening transient at no load - measurement

In Figs. 4.37 and 4.38 it can be seen that the magnitude of the strikes is well below $1pu$ with the rise times about $1\mu s$. The reason for such a voltage level of the surges is that

the chopped current is very small which makes the rate of rise of the dielectric withstand of the breaker soon becoming quicker than the transient recovery voltage. For that reason, reignitions occur only for a very short period of time right after the separation of contacts.

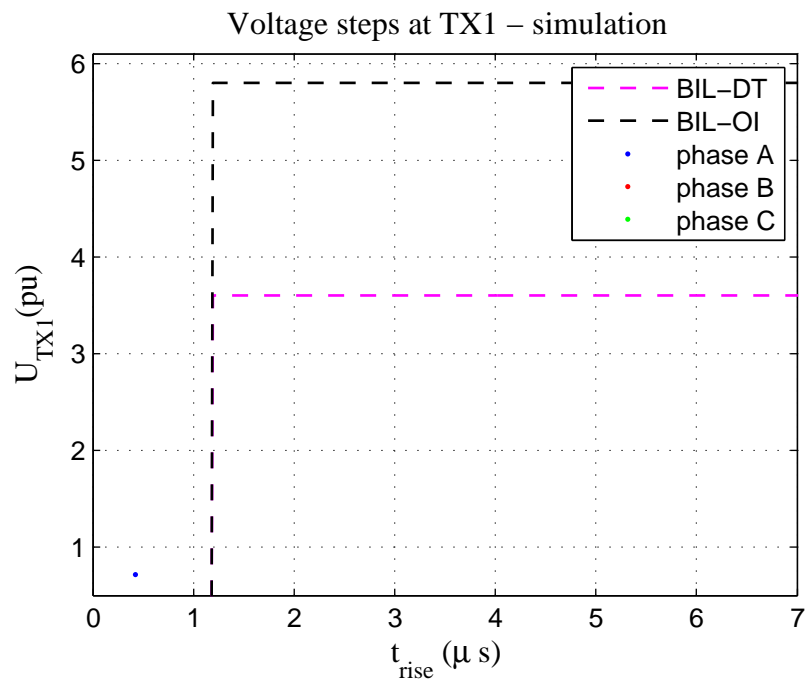


Figure 4.38: Strikes recorded during opening transient at no load - simulation

Inductive load case The case with a switching of an inductive load is chosen since it represents the worst case scenario for the transient voltage. When the current reaches the chopping level, the voltage in that phase is very close to its maximum because of the 90° phase shift. If the breaker contacts are opened at that time instant, the transient voltage is superimposed to the power frequency voltage when it is at its maximum. This produces transient overvoltages with the highest magnitude.

It is important to stress that an interruption of an inductive load is an extreme case conducted to obtain the worst case scenario. However, it does not represent a normal operation in a wind park where it should not be normal practice to open the breakers and switches when the transformer is fully loaded. This case could still happen accidentally, due to malfunction or other reasons. Furthermore, even if such an accident happens, the risk of generation of multiple reignitions and the voltage escalation is quite low since this phenomenon can appear only if the contacts open during a very narrow time window when the current is below the current chopping level.

If a voltage escalation incident occurs in a setup where surge arresters are not installed, the transient voltage can easily breach BIL and damage the transformer. This case is not performed during the measurement for the sake of the tested transformer. Simulations show that in this case, a very high overvoltage is generated. This situation is presented in Fig. 4.39.

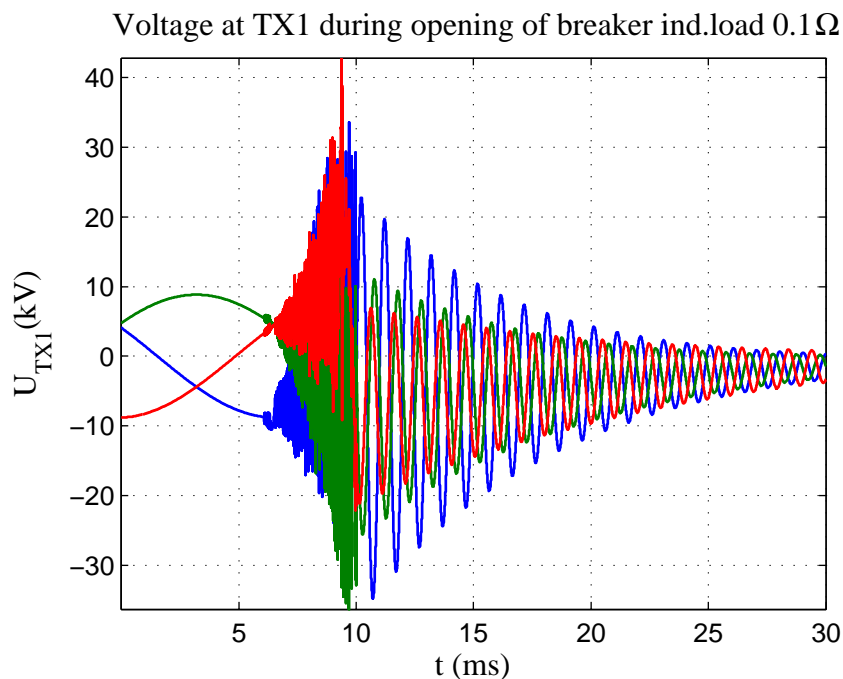


Figure 4.39: Strikes recorded during opening transient at no load without surge arrester - simulation

During the closing operation, it is expected that the transient voltage does not differ compared to the no-load case. The reason for this is that the response of the system during the time between the first prestrike and the touching of the breaker contacts is determined by the same parameters as in the no-load case, the stray capacitance of the transformer C_{tr} and the surge impedance of the cable Z_{cab} . However, due to the bouncing of the contacts, measurement show low magnitude reignitions at the time instant $0.6ms$ after the first pre-

strike. This behavior of the breaker will generate larger number of strikes when compared to the simulation. This is shown in Figs. 4.40 and 4.41.

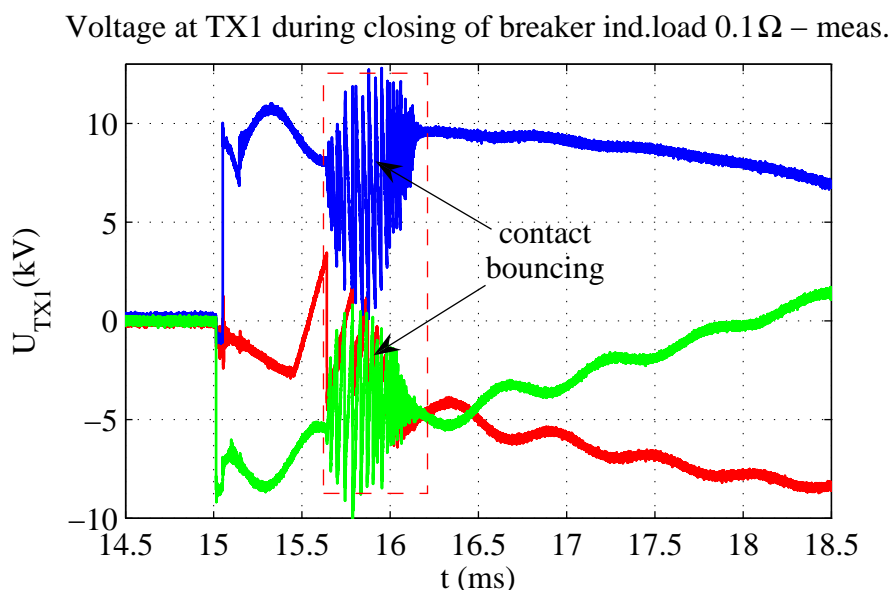


Figure 4.40: Transient voltage at TX1 during closing - inductive load - measurement

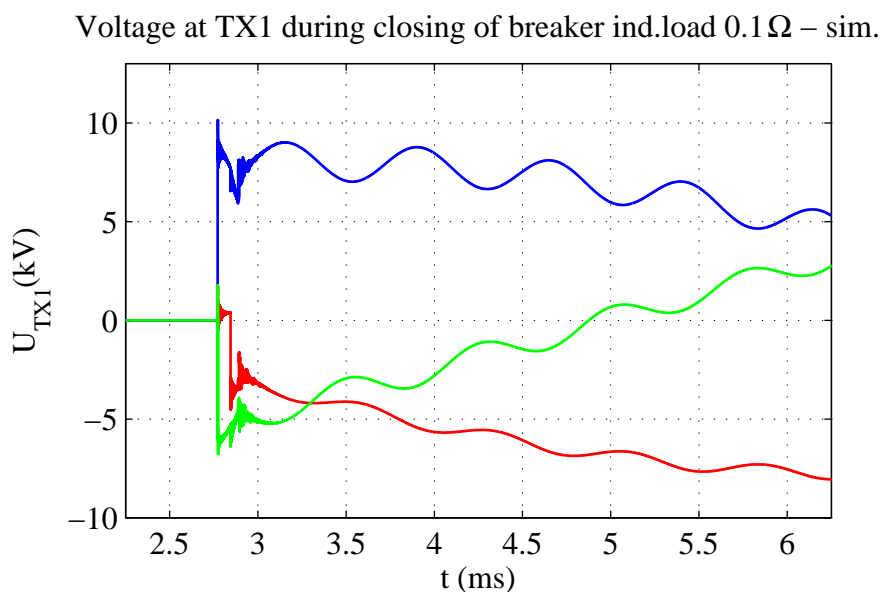


Figure 4.41: Transient voltage at TX1 during closing - inductive load - simulation

Observing the scatter plot showing the strikes recorded during the transient, a larger number of strikes are observed during the measurement. This can be seen in Figs 4.42 and 4.42.

The magnitudes of the voltage strikes are well below BIL levels specified for the dry-type and oil insulated transformers, but have a shorter rise times which is the same as in the no-load case.

For the opening operation of the breaker, a high number of reignitions with the transient voltages reaching the level of the surge protection is expected. As was mentioned before,

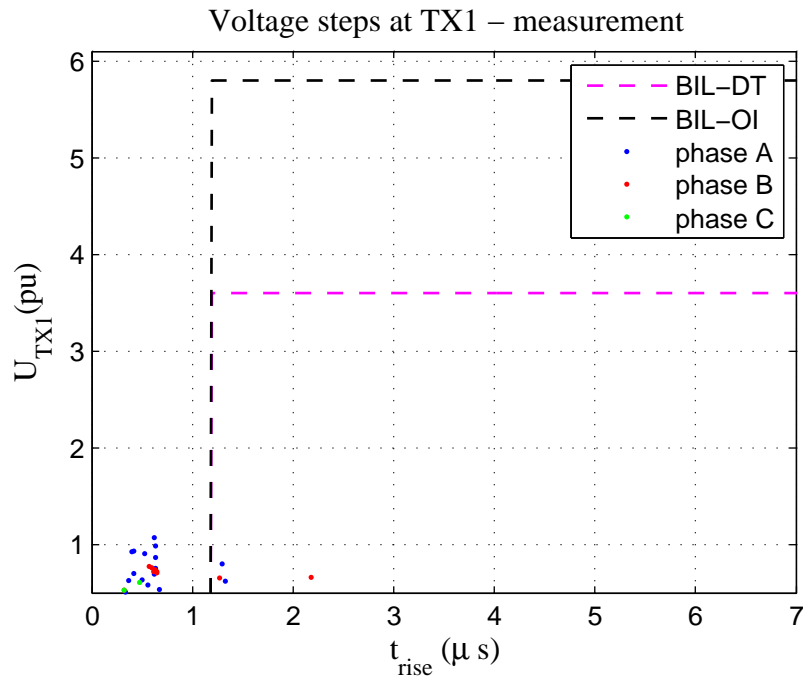


Figure 4.42: Strikes recorded during closing transient at inductive load - measurement

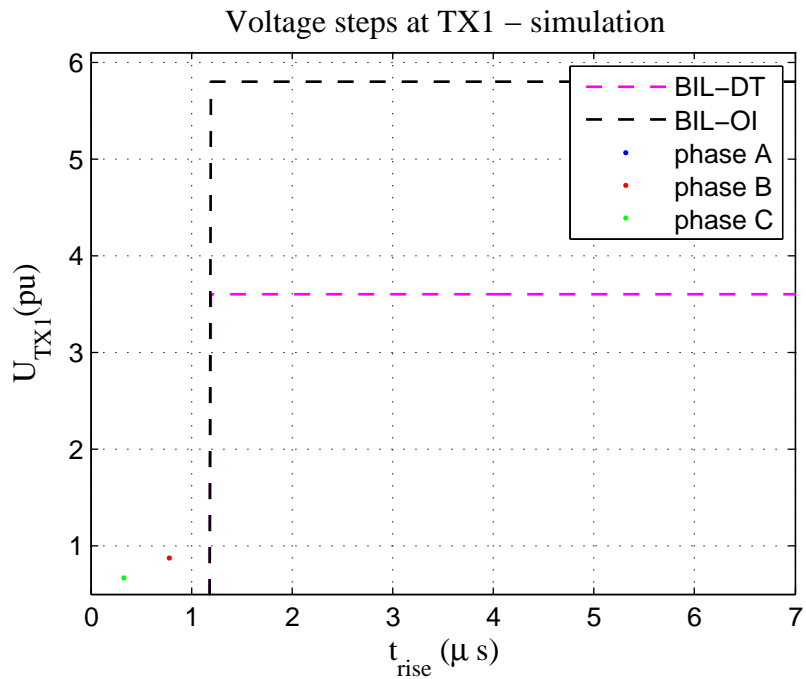


Figure 4.43: Strikes recorded during closing transient at inductive load - simulation

the rate of rise of the transient recovery voltage is much quicker than the rate of rise of the breakers dielectric withstand due to the current chopping. The current chopping level is found to be between 2.5–5A which is much more compared to the current level in the no-load case. This results in a very large number of reignitions. To obtain good agreement between the measurements and simulations, a good breaker model is needed. This is especially the case for the dielectric withstand and the high frequency current quenching capability of the breaker. Observing Figs. 4.44 and 4.45 it can be seen that the dielectric withstand of the

breaker is accurately modeled and calculated using the algorithm described in Section 4.2.3.

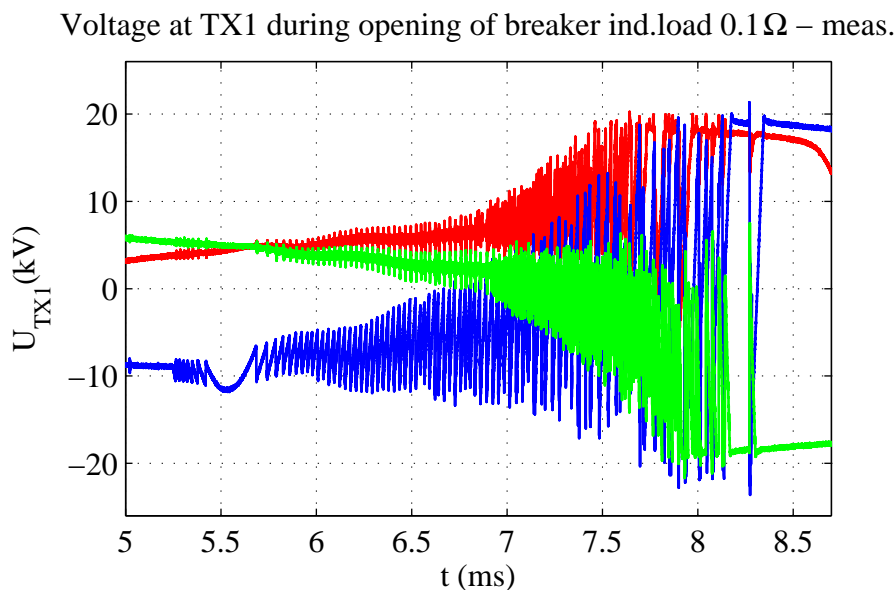


Figure 4.44: Transient voltage at TX1 during opening - inductive load - measurement

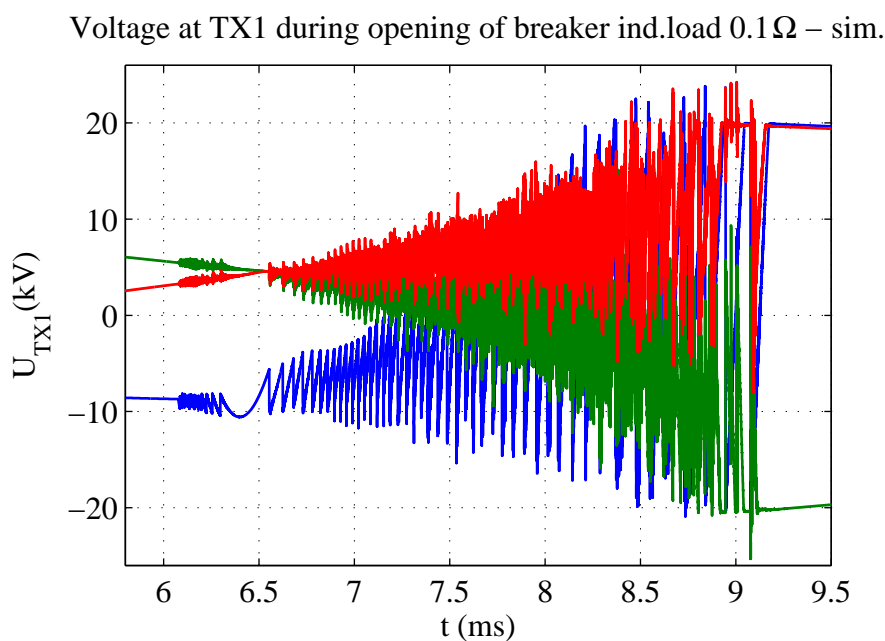


Figure 4.45: Transient voltage at TX1 during opening - inductive load - simulation

The high frequency oscillations caused by the high frequency current are simulated with good accuracy. That can be seen in Fig. 4.46 during the time period between the start of the voltage surge and 0.02ms after. When the low magnitude high frequency oscillations are observed which are induced by surges in other phases due to the capacitive coupling, it can be seen that these oscillations are damped very poorly in the simulation. This is because of a simplified transformer model with stray capacitances. This can be improved by adding some resistance to the transformers stray capacitances. These oscillations are observed between 8.5ms and 8.54ms in the simulation plot shown in Fig. 4.47 and between 8.11ms and 8.12ms in the measurement plot in Fig. 4.46.

Voltage at TX1 during opening of breaker ind.load $0.1\ \Omega$ – meas.

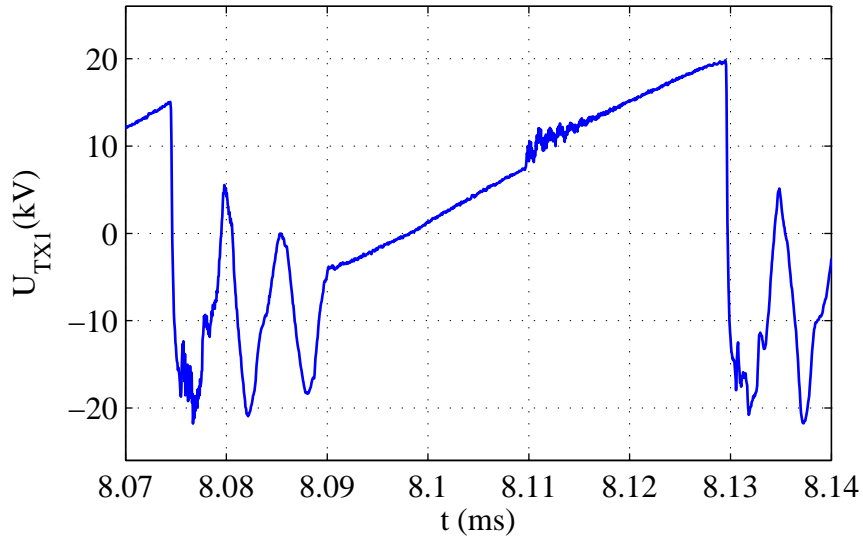


Figure 4.46: Transient voltage HF oscillations - inductive load - measurement

Voltage at TX1 during opening of breaker ind.load $0.1\ \Omega$ – sim.

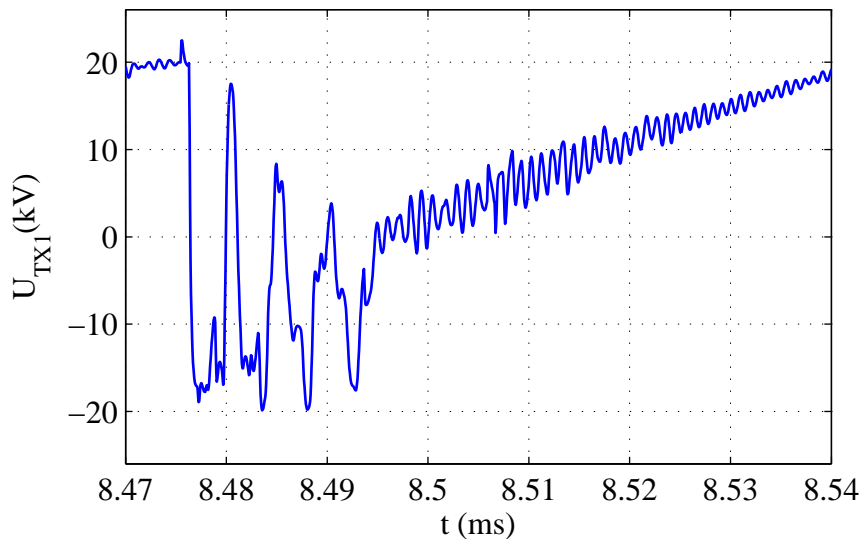


Figure 4.47: Transient voltage HF oscillations - inductive load - simulation

The steepness of the voltage slope and its rise time match very well. This result is already shown for the closing operation, and for the opening operation it is presented in Fig. 4.48. In this direct comparison of the measured and simulated voltage surge, a very good agreement in slope is obtained. However, the magnitude of the voltage transient obtained by the simulation is reduced due to the stronger oscillations caused by the low damped capacitive coupling of the transformer. Furthermore, high magnitude oscillations appearing at the time instant $t = 8.7315\text{ms}$ presents the voltage wave reflected from transformer TX2 and it can be noticed that the wave propagates at a slightly higher speed in the simulations. This is because the cable model is made using three single-core cables due to the limitations of the PSCAD/EMTDC cable model, while in the measurements three-core cables are used.

The result showing strikes during the voltage transient is presented in Figs. 4.49 and

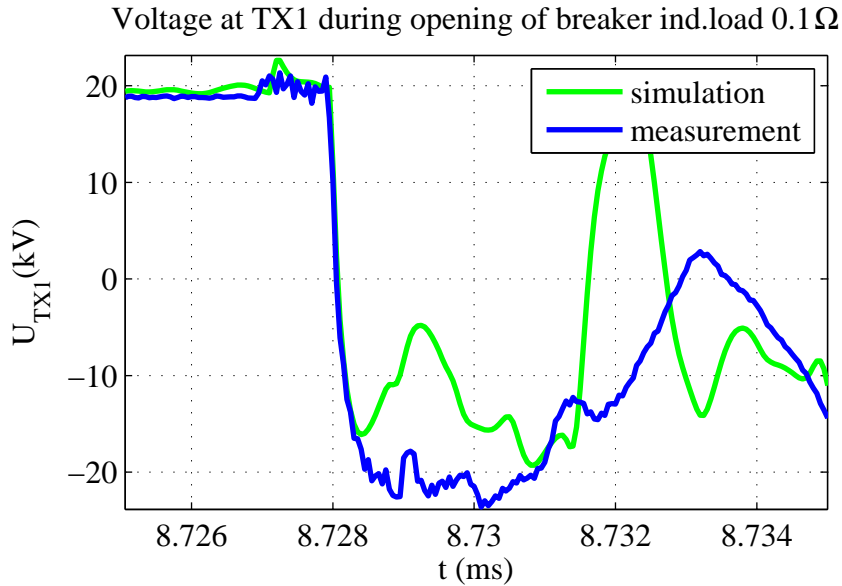


Figure 4.48: Voltage slope - comparison

4.50. This result is going to be analyzed by separating the strikes in three groups. The first group contains voltage surges with a rise time of $0.5\mu s$. This group represents the voltage surges formed during the breakdown of the dielectric in the breaker. Surges recorded both in simulations and measurements show that the magnitude and the rise time of the surge exceeds the limits defined by BIL. This occurs even with a surge arrester installed at the terminals of the transformer, proving that the surge arrester protection can not provide sufficient protection without use of additional protective devices.

When simulations are compared to the measurements, good agreement is observed in the rise time and in the magnitude of the surges. However, a larger number of voltage surges are observed in simulations. This result is influenced mostly by the low damped capacitive coupling of the transformer, since the most important difference is in two phases (B and C) where the breaker poles start to separate approximately $1 - 1.5ms$ later. This difference is observed in Fig. 4.44 also.

The second group of strikes with rise times of $2 - 2.5ms$, represent the high frequency oscillations caused by the high frequency current appearing right after the voltage breakdown as shown in Figs 4.46 and 4.47 at time intervals between $8.075 - 8.09\mu s$ and $8.475 - 8.495\mu s$ respectively. Both the magnitude and the rise time have good agreement between the measurements and simulations.

The last group of strikes representing the transient recovery voltage is completely missing in the simulation scatter plots. The reason for this is that the characterization algorithm did not recognize the transient recovery voltage as single voltage steps due to the presence of the high frequency oscillations shown in Fig. 4.47.

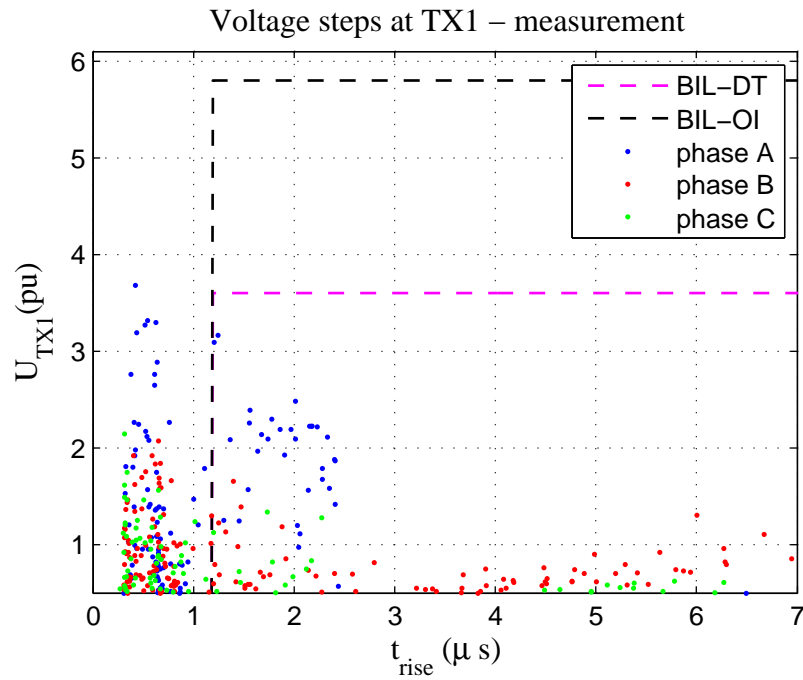


Figure 4.49: Strikes at TX1 during opening - inductive load - measurement

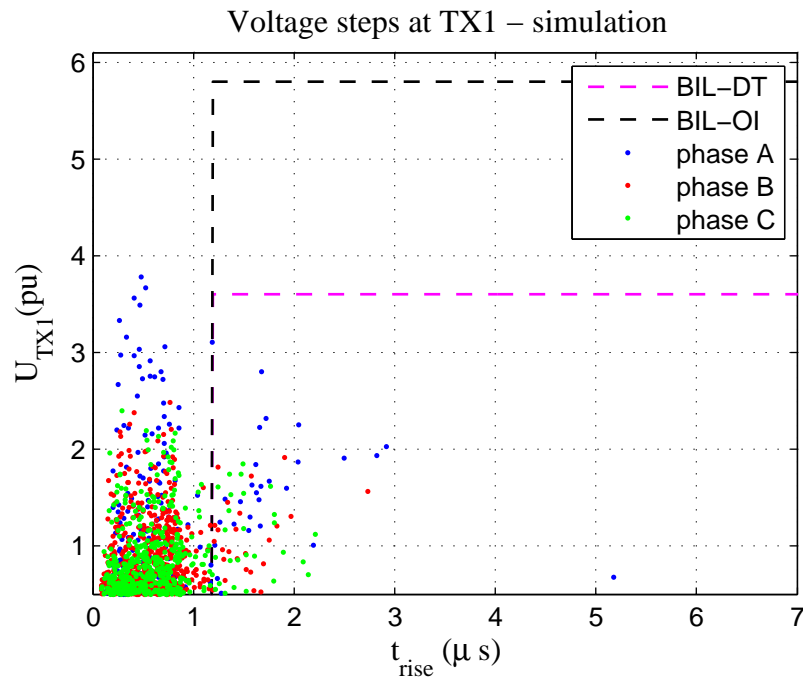


Figure 4.50: Strikes at TX1 during opening - inductive load - simulation

Surge Capacitor Protection

Surge capacitors have been commonly used as protection device to mitigate transients. The combination of surge capacitors and surge arresters has been used to protect medium voltage induction motor windings from steep-fronted voltage surges [62]. The purpose of using the surge capacitor is to reduce the rise time of the surge [63]. In this report, two case of surge capacitor protection is used, where the capacitance of the surge capacitor is either $83nF$ or

130nF. The surge capacitor is installed in front of transformer TX1. The surge arrester is kept at the transformer terminals to limit the maximum overvoltage appearing on the transformer. The scheme showing the full setup is presented in Fig. 4.51.

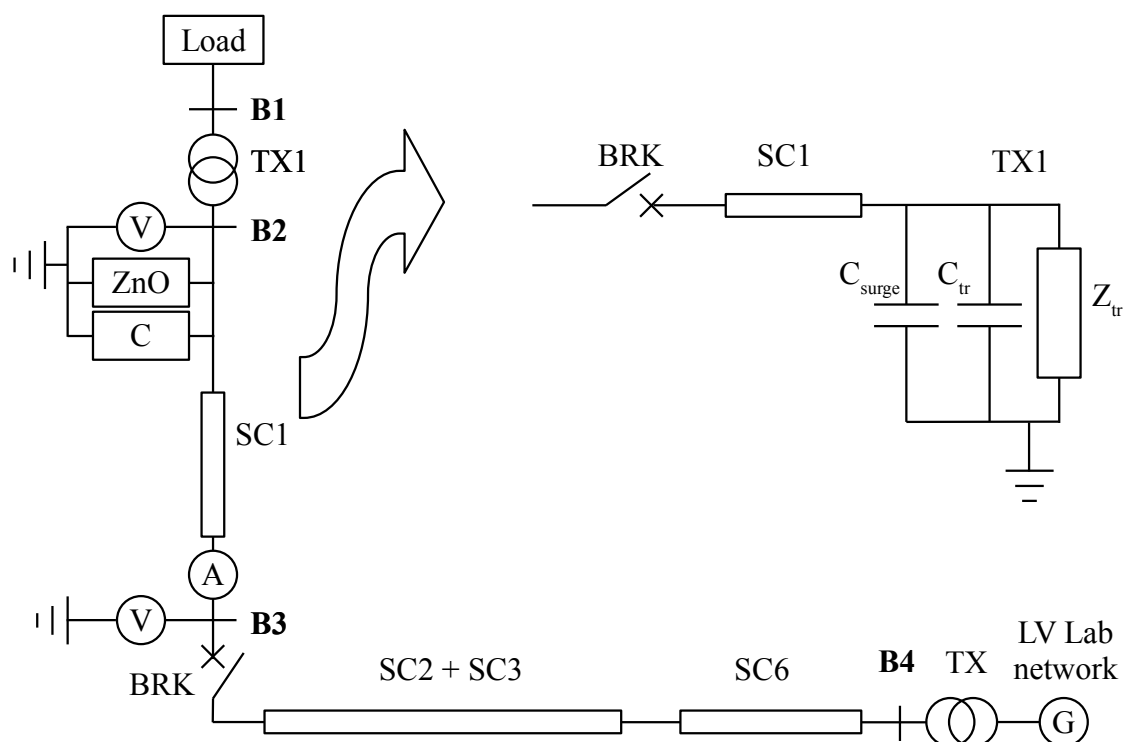


Figure 4.51: Capacitor at TX1

The purpose of having the surge capacitor is to slow down the surge front and the transient recovery voltage. The consequence of reducing the steepness of the voltage surge is that the rise time of the surge is brought into the limits defined by standards ($1.2\mu s$).

This is achieved by increasing the time constant of the transformer by adding additional capacitance as shown in Fig. 4.52.

The time constant of the surge is given by

$$\tau = Z_{cab} (C_{tr} + C_{surge}) \quad (4.9)$$

where C_{surge} is the capacitance of the surge capacitor.

In Fig. 4.53 the impact of the surge capacitor protection on the surge rise time is observed. The results obtained by the simulation agree with the analytical calculations presented with dotted lines. The oscillations of the voltage appearing in the plot are caused by the stray inductance of the capacitor leads and can be minimized when shorter leads are used. The value of the lead stray inductance is calculated according to the length and the cross section area of the surge capacitor leads.

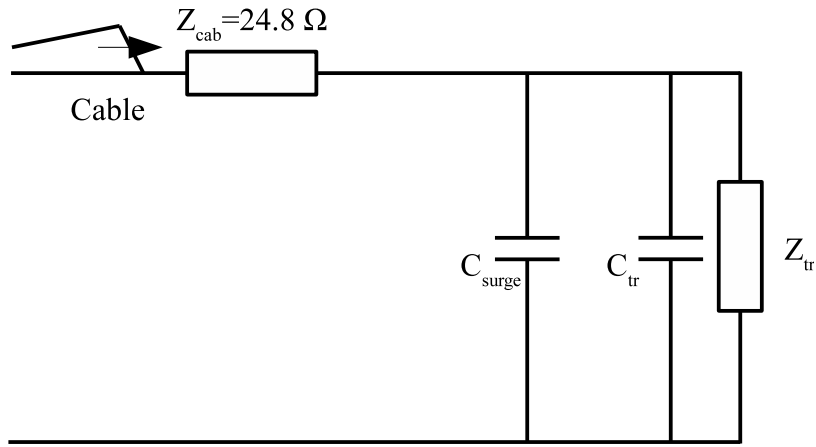


Figure 4.52: Surge capacitor protection - simplified circuit

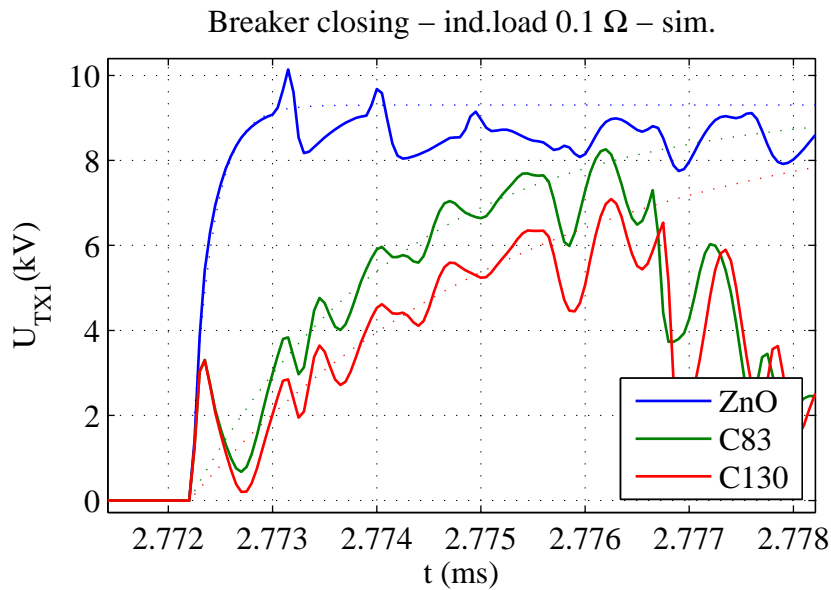


Figure 4.53: Voltage surge rise time without and with surge capacitor protection - simulation

The transient recovery voltage is also affected by the added capacitance in the system. The rate of rise of the transient recovery voltage is reduced leading to a lower number of reignitions. This can be observed in Fig. 4.54 where the transient recovery voltage is showed both with and without the surge capacitor added.

A stiffer voltage obtained by added capacitance in the system results in a significantly reduced magnitude of the voltage strikes during the opening of the breaker. This behavior is noted both for $C = 83nF$ and $C = 130nF$ surge capacitor protection and can be observed in Figs. 4.55 and 4.56.

As it can be noted from Figs. 4.55 and 4.55, the number of reignitions during the breaker opening operation is significantly reduced when surge capacitors are used. Moreover, the magnitude of the voltage strikes is reduced by a factor of two when the $130nF$ surge capacitors are installed.

However, the additional capacitance causes voltage oscillations during the energizing tran-

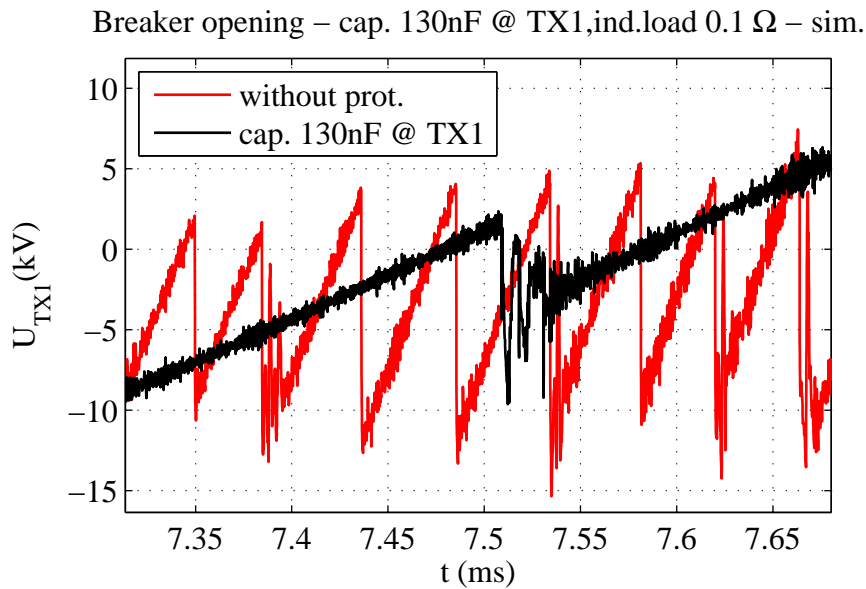


Figure 4.54: Rate of rise of transient recovery voltage - simulation

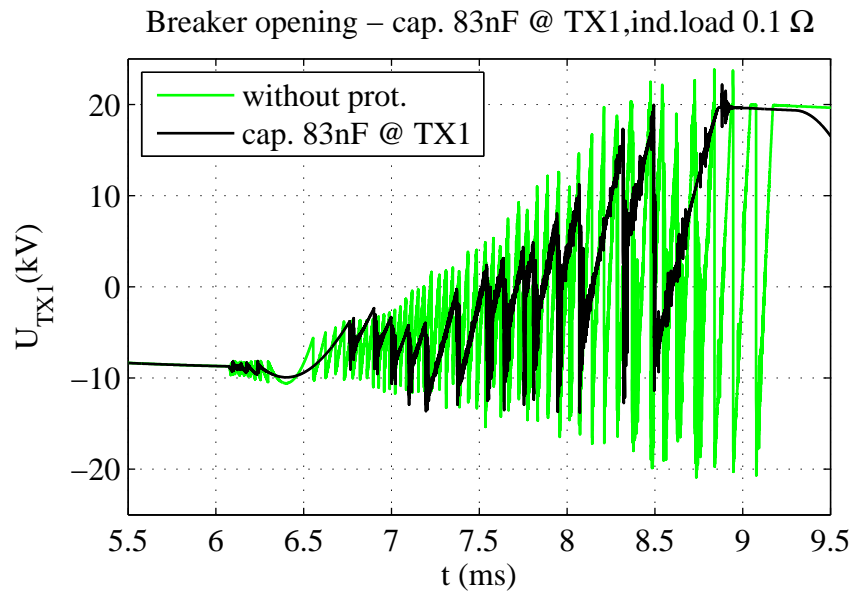
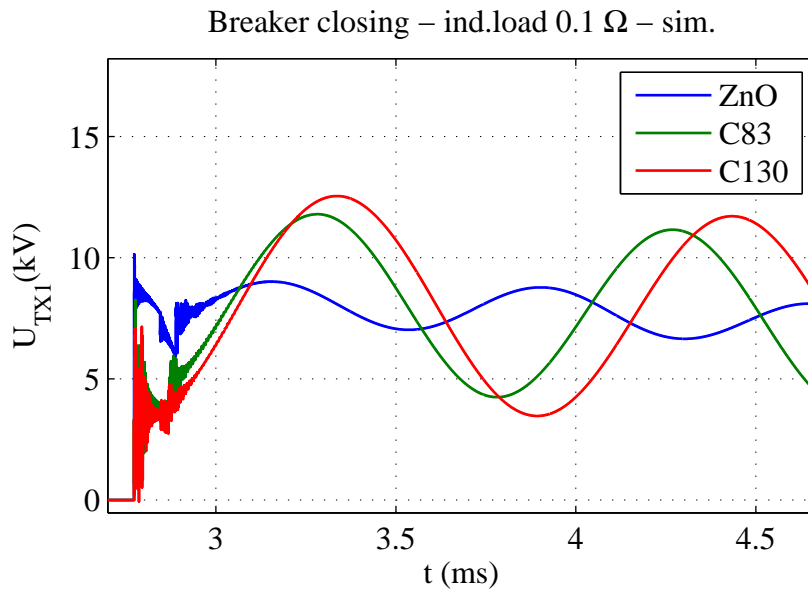
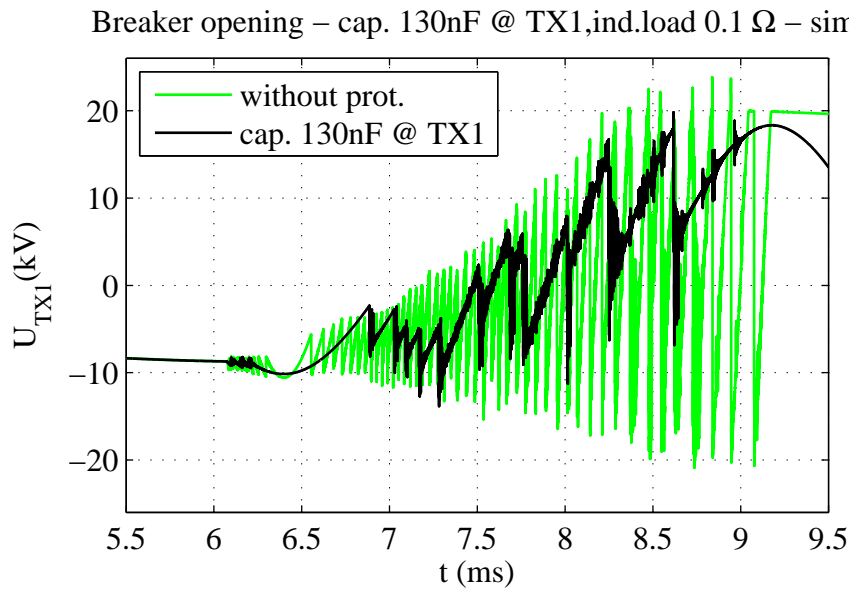


Figure 4.55: Impact of 83nF surge capacitor on transient voltage - simulation

sient. The comparison of these voltage oscillations for different values of surge capacitance is shown in Fig. 4.57.

The comparison of the simulation results shows very good agreement to the measurements. In general, comments of the analysis of the base case can be confirmed for the case with the surge capacitor protection. The negative impact of the simplified transformer model which does not include the damping added to stray capacitances is even more dominant. The added capacitance produces even more high frequency oscillations which are low damped.

The transient voltage during the opening operation of the breaker recorded during the measurements and simulations for the 83nF surge capacitor protection is shown in Figs. 4.58 and 4.59.



The time instant of the contact separation obtained during the measurement is far from the worst case and does not represent the perfect case for the simulation result verification. Moreover, the first reignition in the measurement result occurs in phase C (green), while in the simulation, phase A re-ignites first. This affected significantly the result comparison for this case. However, the same observations can be made when the scatter plot is observed showing the voltage strikes during the transient which is presented in Figs. 4.60 and 4.61.

Due to the specific time instant of the breaker operation during the measurements, voltage strikes with significantly higher magnitude are observed in Fig. 4.60. Two groups of strikes can be observed when the rise times of the strikes are compared. Although the surge capacitors increase the time constant of the voltage surge, the first group of strikes reach 0.2μs rise times. This is because of the stray inductance of the capacitor leads, which can

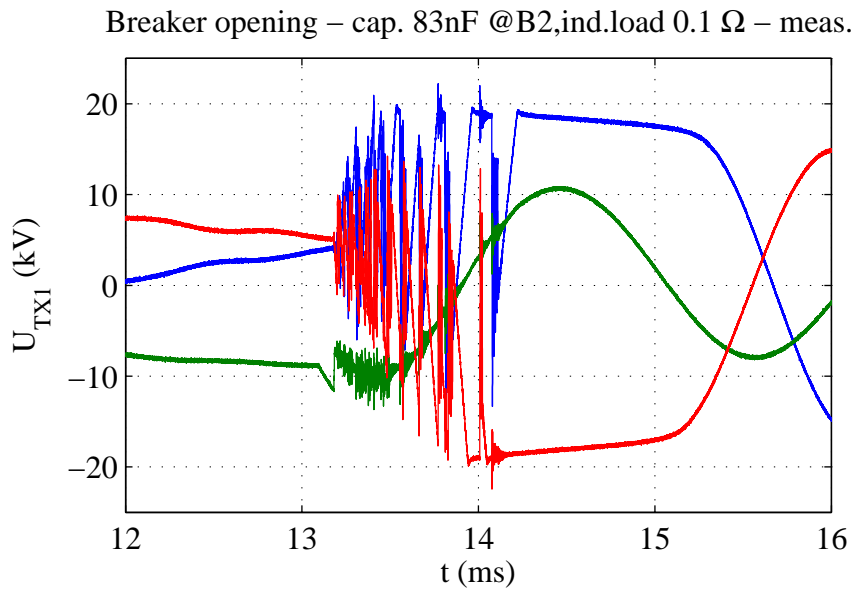


Figure 4.58: Transient voltage during opening - surge capacitor $83nF$ - measurement

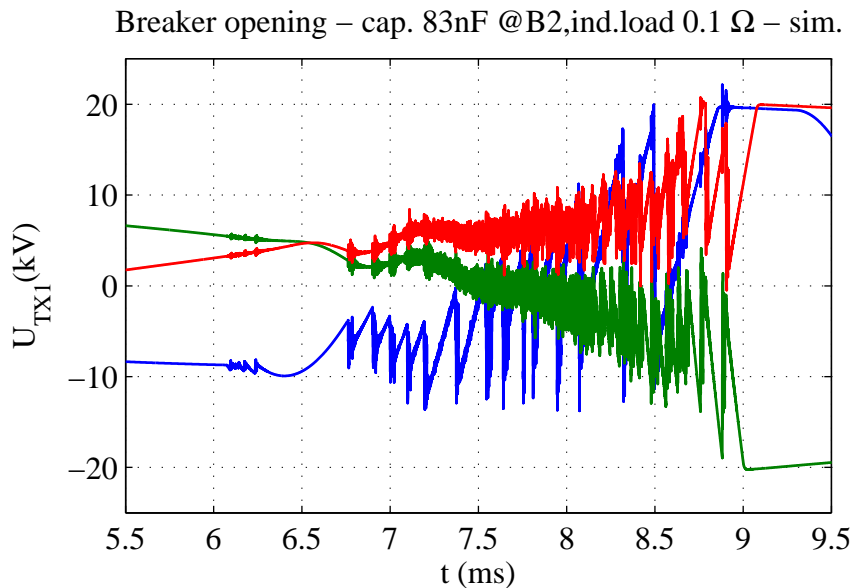


Figure 4.59: Transient voltage during opening - surge capacitor $83nF$ - simulation

be reduced by shortening its length.

The second group of voltage strikes present the strikes of the slope reduced up to $3 - 3.5\mu s$. The reduced rise time of these strikes is a direct influence of the installed surge capacitors. Both simulation and measurement show that the magnitude of the voltage strikes is significantly reduced when compared to the case with only surge arresters installed. The simulation shows the voltage surge magnitude decrease by more than 50% while for the measurement the resulting voltage surges are reduced about 30% in magnitude. This means that the surge capacitors in combination with surge arresters decrease the magnitude of the strikes below BIL.

For the case when a larger surge capacitor of $130nF$ is installed, the timing of the contact

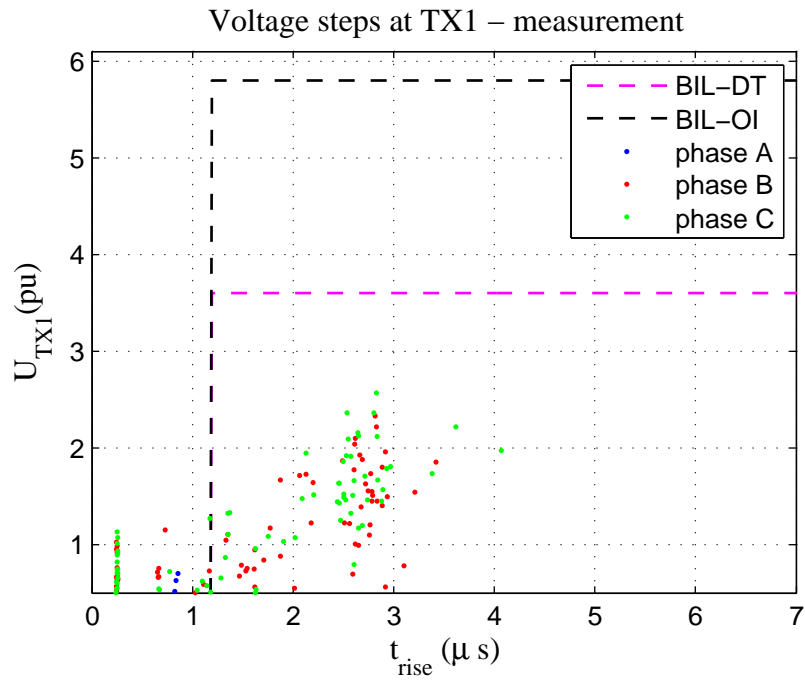


Figure 4.60: Strikes at TX1 during opening - surge capacitor 83nF - measurement

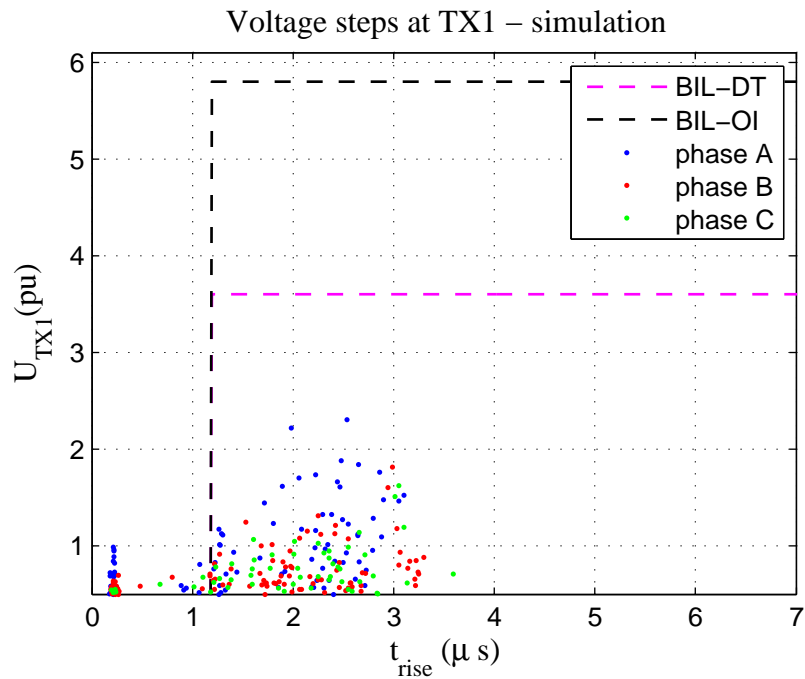


Figure 4.61: Strikes at TX1 during opening - surge capacitor 83nF - simulation

separation in the simulations matches closely the timing recorded in the measurement. Plots which show the transient voltage during the opening operation of the breaker when a 130nF surge capacitor is used, can be seen Figs. 4.62 and 4.63.

Observing the simulation and the measurement results in Figs. 4.62 and 4.63 it can be noted that the time instant of the start of the contact separation is in good agreement. Furthermore, the magnitude of the strikes and the rate of rise of the recovery voltage are

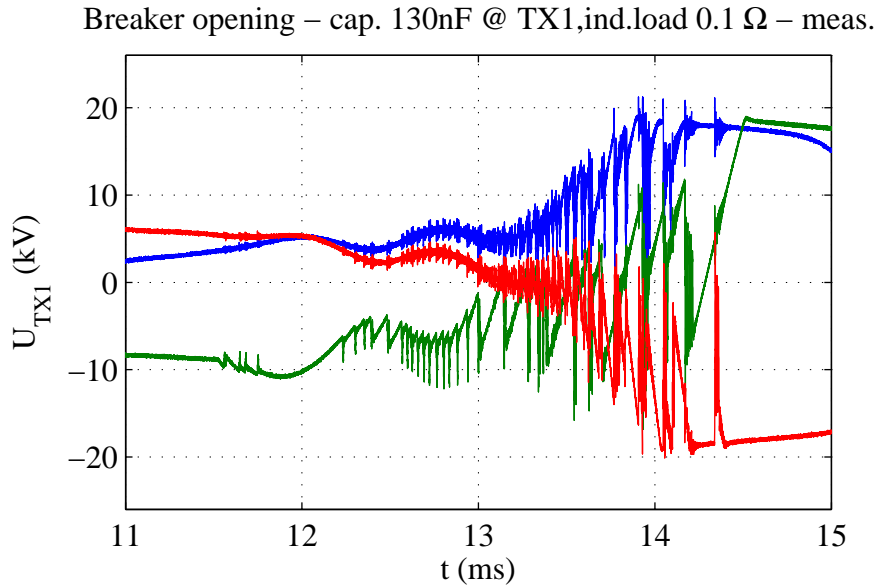


Figure 4.62: Transient voltage during opening - surge capacitor 130nF - measurement

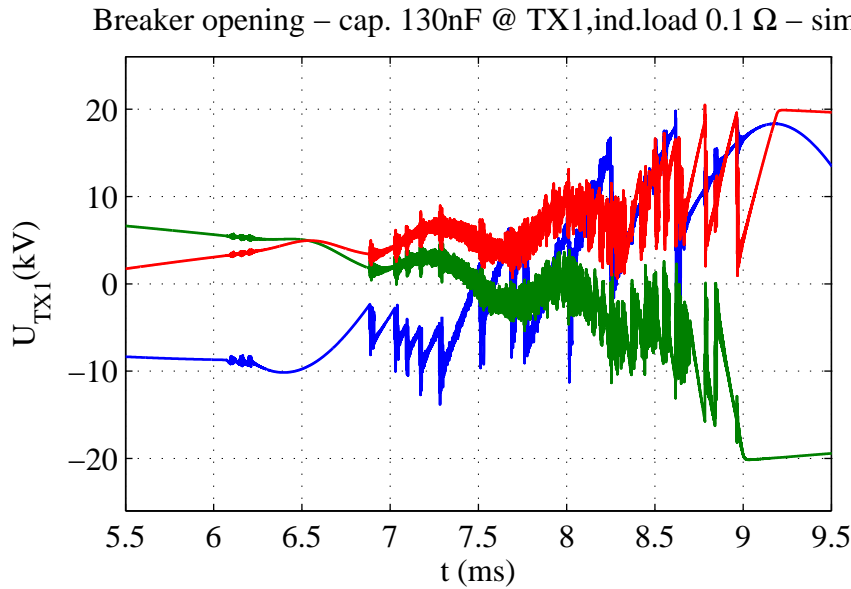


Figure 4.63: Transient voltage during opening - surge capacitor 130nF - simulation

simulated with good accuracy. However, since the damping of the high frequency oscillations at the transformer is very low, the capacitive coupling between phases is more evident in the simulation plot where some very strong high frequency oscillations can be seen after every strike.

Although the measurement show the presence of strikes with a rise time of almost $5\mu s$, in the simulations, the slowest strike has the rise time of $4\mu s$, good agreement is observed when the voltage strikes are compared. The agreement in the magnitude of the voltage strike is below 10%, while the comparison of the voltage surge rise times is within 20%. As in the case with a $83nF$ surge capacitor, surge magnitudes dropped significantly when compared to the base case and are kept below the $2pu$ limit. As expected, the result is improved even when compared to the $83nF$ surge capacitor protection case.

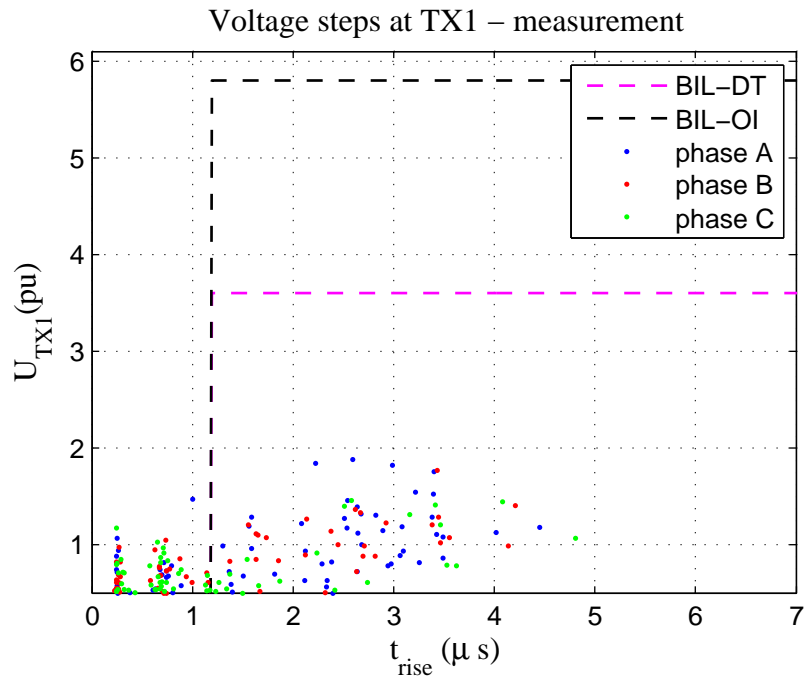


Figure 4.64: Strikes at TX1 during opening - surge capacitor 130nF - measurement

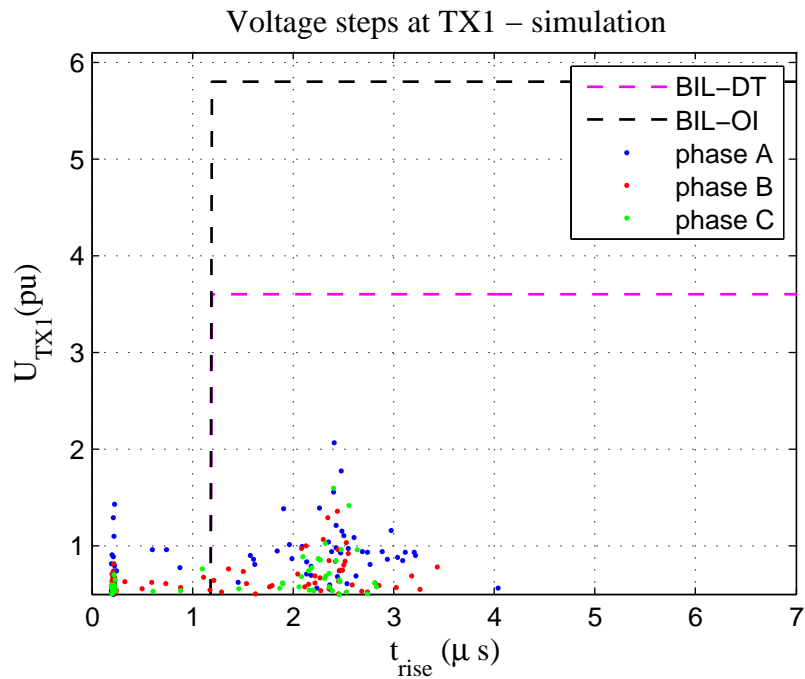


Figure 4.65: Strikes at TX1 during opening - surge capacitor 130nF - simulation

Yet another case with the surge capacitor protection is studied. In this case, the surge capacitor is not placed at the terminals of the protected device but instead at the terminals of the breaker at bus B3. This scheme is presented in Fig. 4.66.

As expected, the impact on the transient voltage in this case is very similar to the case when a 130nF capacitor was placed at transformer TX1. The rate of rise of the transient recovery voltage is significantly reduced when compared to the base case, which can be seen

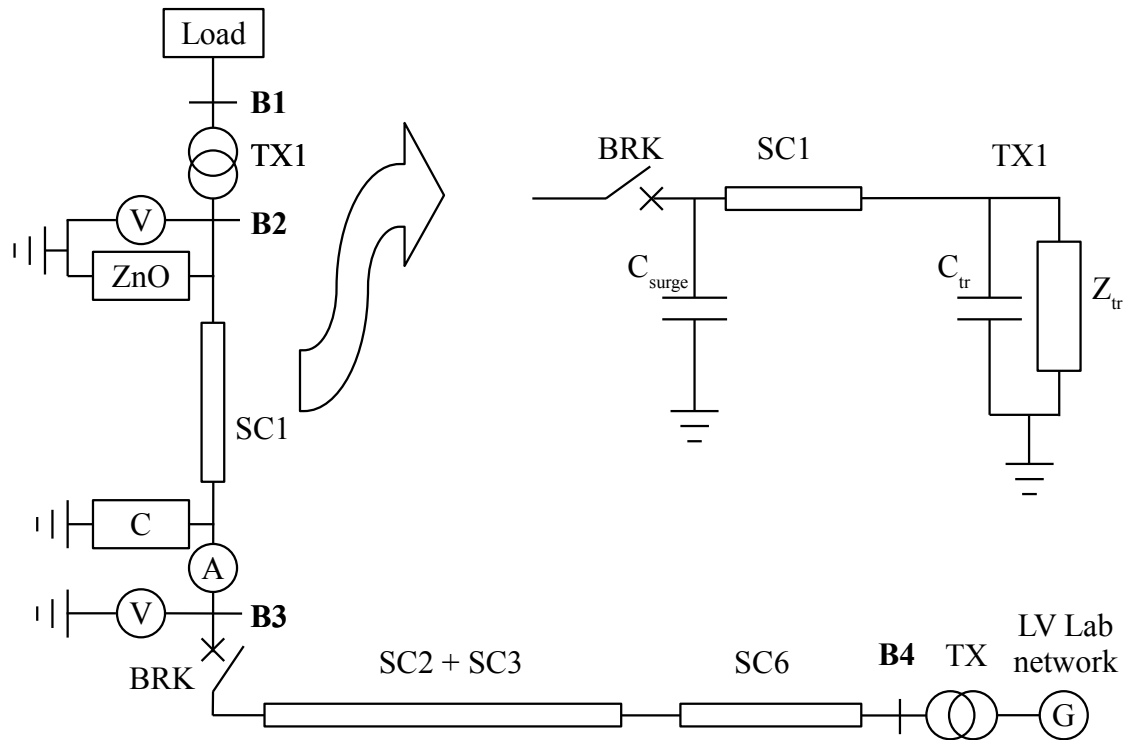


Figure 4.66: Capacitor at breaker

in Fig. 4.67

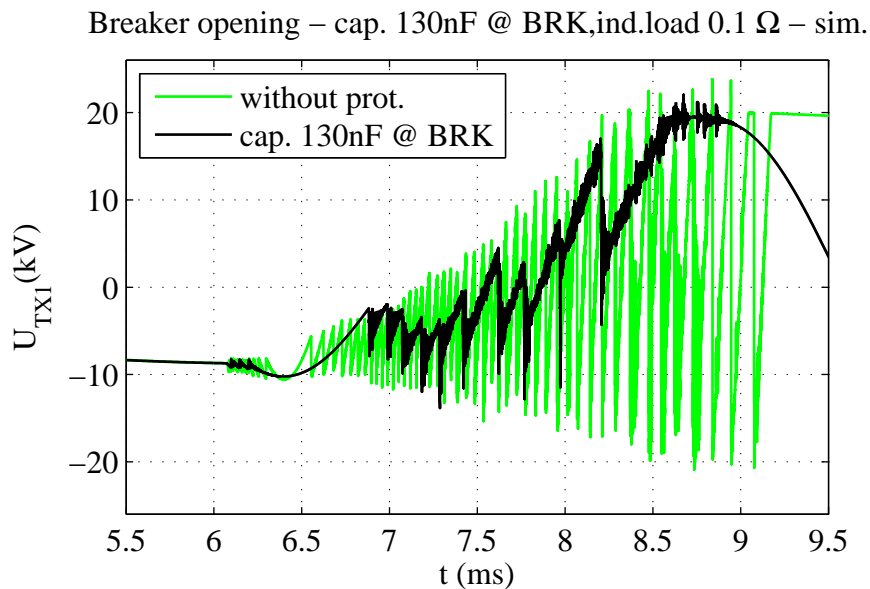


Figure 4.67: Impact of 130nF surge capacitor at breaker on transient voltage - simulation

Moving the surge capacitor moving to the other side of the cable changes behavior of the high frequency oscillations so the capacitive coupling of the phases is more evident in the

plots. This is because the current bursts which charge the the surge capacitor during the voltage surges, do not travel along the cable any more. Furthermore, the wave reflection is also affected by moving the surge capacitor to the breaker since the current waves coming from TX1 towards the breaker are almost completely reflected back. This results in an increase of the high frequency oscillations and can be seen in Figs. 4.67-4.69.

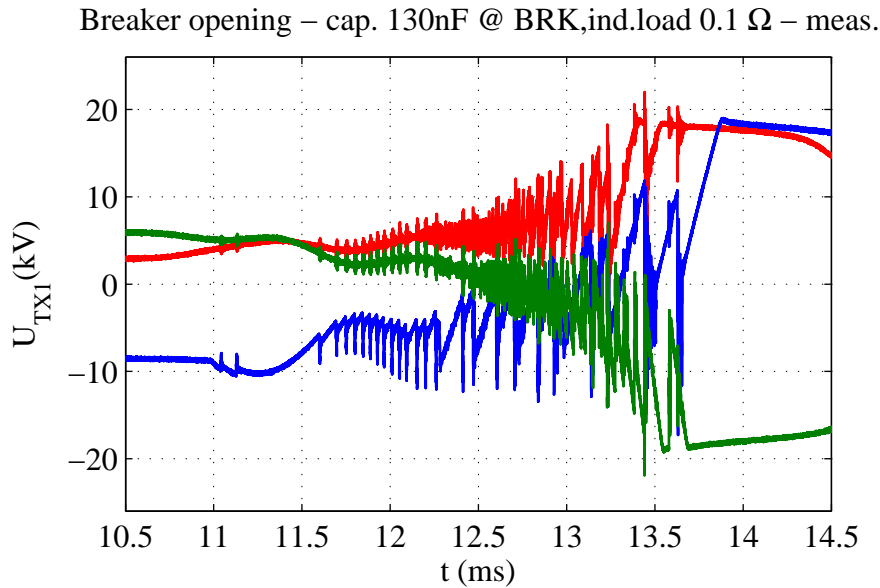


Figure 4.68: Transient voltage during opening - surge cap. 130nF at breaker - measurement

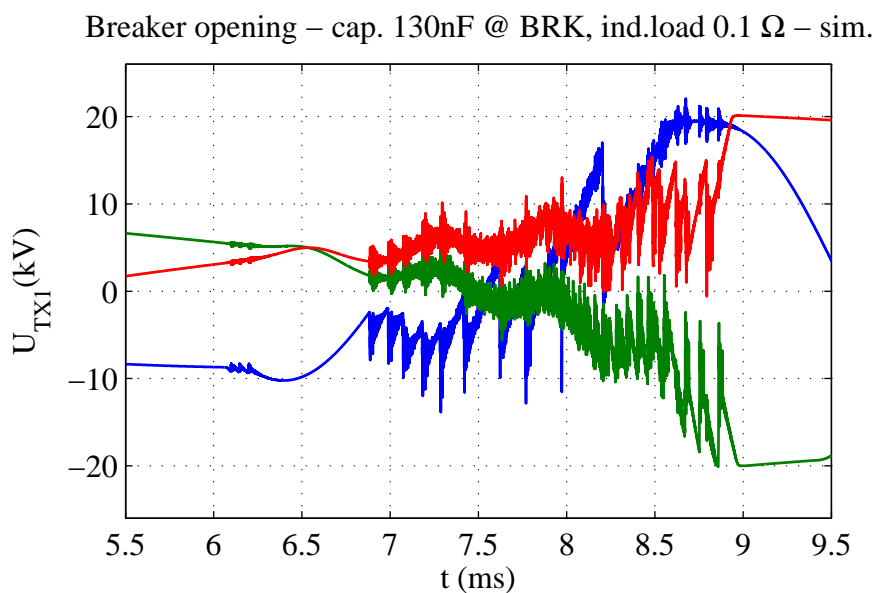


Figure 4.69: Transient voltage during opening - surge cap. 130nF at breaker - simulation

When the magnitudes and the rise times of the voltage surges recorded at transformer TX1 are compared, a good agreement between simulations and measurements is observed. Plots showing strikes during the opening of the breaker are shown in Figs. 4.70 and 4.71.

In Figs. 4.70 and 4.71 it can be seen that a very similar result compared to the other 130nF surge capacitor case is obtained. The magnitude and the rise times of highest recorded surges are almost identical. Furthermore, the reignitions are also observed as in other cases

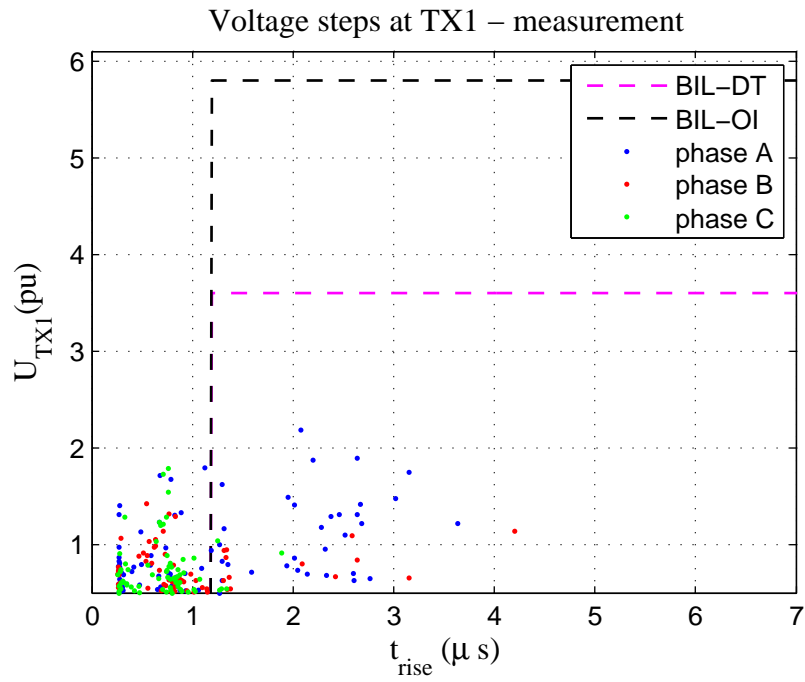


Figure 4.70: Strikes at TX1 during opening - surge cap. 130nF at breaker - measurement

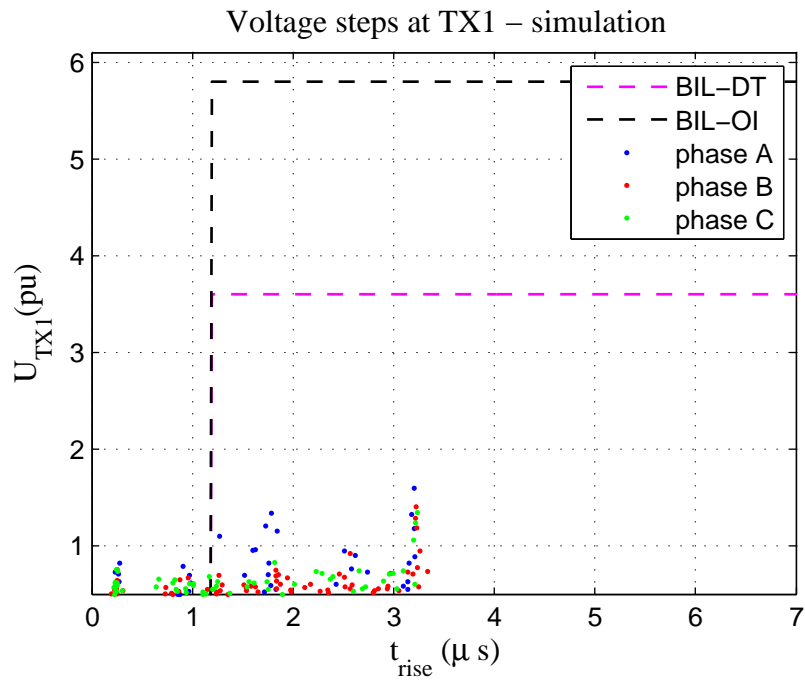


Figure 4.71: Strikes at TX1 during opening - surge cap. 130nF at breaker - simulation

when surge capacitors are used, but the number of reignitions is significantly lower when compared to the base case.

RC protection

The RC protection is used for mitigation of the high frequency transients and protection of transformers and induction motors [16], [64]. It is very effective and proved to reduce the number of reignitions [16]. The principle of an RC protection is very simple. The wave reflections which give the highest magnitude of transient overvoltages occur in the systems where the surge impedance of the transformer Z_{tr} is much higher than the cable surge impedance Z_{cab} . In order to prevent such reflections, a resistor with a capacitor is connected in parallel to the protected transformer. This is presented in Fig. 4.72.

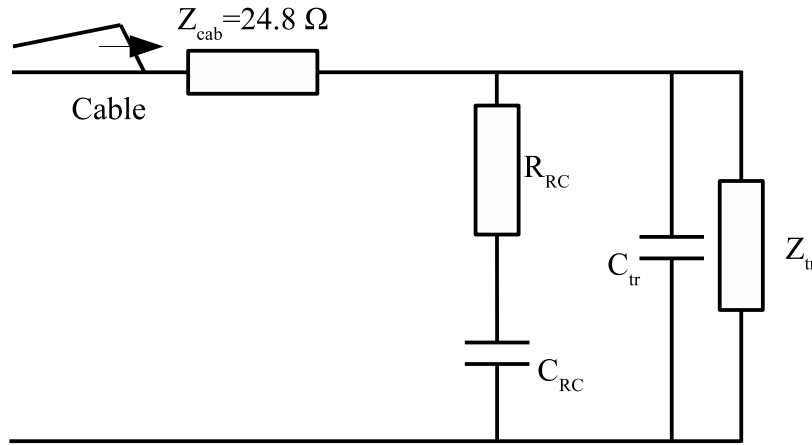


Figure 4.72: RC protection scheme

The resistance of the resistor is chosen so it matches the surge impedance of the cable Z_{cab} . By doing this, the wave reflections are avoided since the reflection coefficient is equal to zero

$$\alpha = \frac{R - Z_{cab}}{R + Z_{cab}} = 0. \quad (4.10)$$

Another way to explain the principle of the RC protections is to observe it as a special case of the surge capacitor protection. The surge capacitor used in the RC protection will act in the same way as when it is directly connected to the terminals of the protected transformer, which means that the rise time of the surge is increased. The resistor connected in series to it is used to damp the high frequency current which occurs after every strike. By damping the high frequency current superimposed to the power frequency current, the current zero crossing and thus the reignition is avoided if the power frequency current is very high. This method is shown to be very effective during the induction motor starts [16].

However, the generation of the reignition depends on other factors such as the rate of rise of the breaker dielectric withstand and the rate of rise of the transient recovery voltage. For this reason, the RC protection may not be sufficient to eliminate reignitions completely, but will definitely reduce the number of reignitions and the magnitude of the voltage strikes.

For the laboratory experiment, three cases are set and studied. For all of them, the scheme presented in Fig. 4.73 is used.

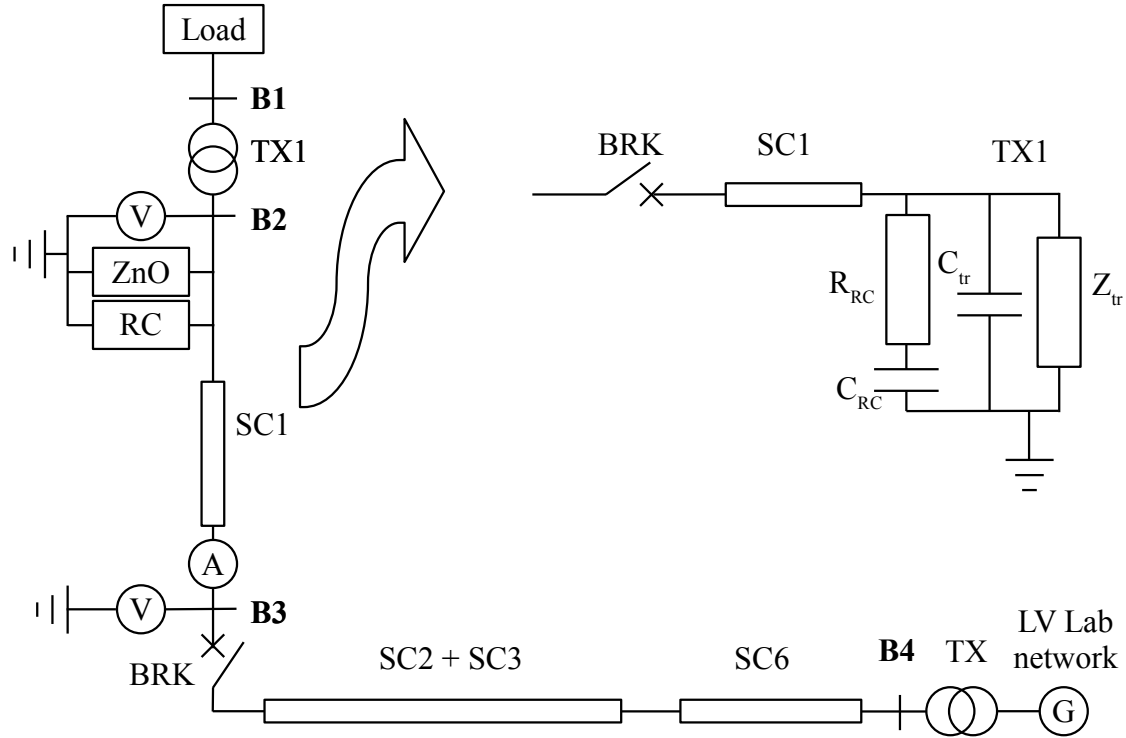


Figure 4.73: RC protection test setup

The first case is with the resistor of $R = 20\Omega$ and the capacitor with $C = 83nF$ capacitance. The second case is developed using the same resistor of $R = 20\Omega$ and the capacitor with higher capacitance of $C = 130nF$. For the final case, the resistance of the resistor is increased compared to the first case to 30Ω , while the capacitance of the surge capacitor is kept at $83nF$. The surge impedance of the cable is calculated to be 24.8Ω , and none of the aforementioned cases do not present a characteristic impedance termination. However, the resistance of the surge resistors is very close to this value and all these cases represent a good base for an RC protection study.

The effect of the RC protection on the voltage transient during the opening of the breaker recorded in simulations is shown in Fig. 4.74.

In Fig. 4.74 it can be seen that the RC protection did not stop the appearance of the reignitions. The reason for this is that the rate of rise of the transient recovery voltage is higher than the rate of rise of the breakers dielectric withstand. The impact is similar to the surge capacitor protection but with improved damping of the high frequency voltage oscillations caused by the high frequency current. For the second case with increased capacitance of the RC protection, the simulation results are presented in Fig. 4.75.

Although the transient recovery voltage is slowed down even further by increased capacitance of the system, it was not enough to prevent reignitions. In the very beginning of the transient, the rate of rise of the transient recovery voltage is high due to the current chopping, and the breakers dielectric withstand is still very slow with the initial speed of

Breaker opening – RC 20Ω&83nF @ TX1,ind.load 0.1 Ω – sim.

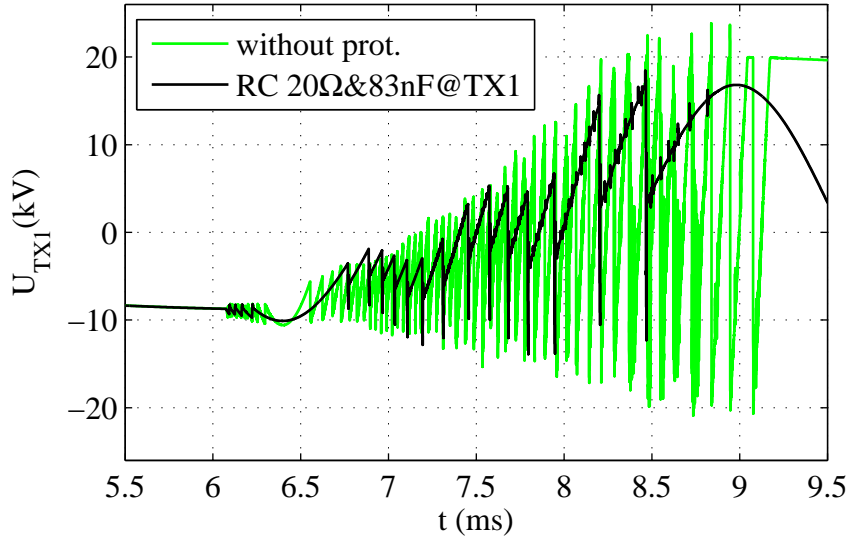


Figure 4.74: Impact of RC protection on transient voltage ($R20\Omega\&C83nF$) - simulation

Breaker opening – RC 20Ω&130nF @ TX1,ind.load 0.1 Ω – sim.

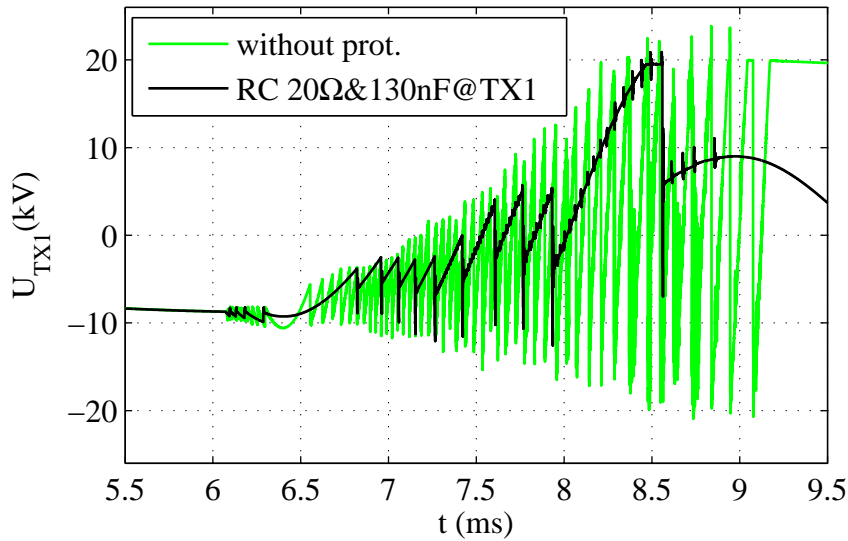


Figure 4.75: Impact of RC protection on transient voltage ($R20\Omega\&C130nF$) - simulation

5.5kV/ms.

The third case with a 30Ω resistor and a 83nF capacitor is presented in Fig. 4.76.

All these plots which are shown in Figs. 4.74-4.76 are very similar. It can be noted that there is no significant difference for the 20Ω and 30Ω resistor case. However, the only slight difference can be seen in the case with a 130nF capacitor, where the rate of rise of the transient recovery voltage is slower compared to the cases with a 83nF surge capacitor.

Compared to the measurements, all three cases show good agreement in the simulation and the measurement results. The result obtained by the measurement and the simulation for the first case is presented in Figs. 4.77 and 4.78.

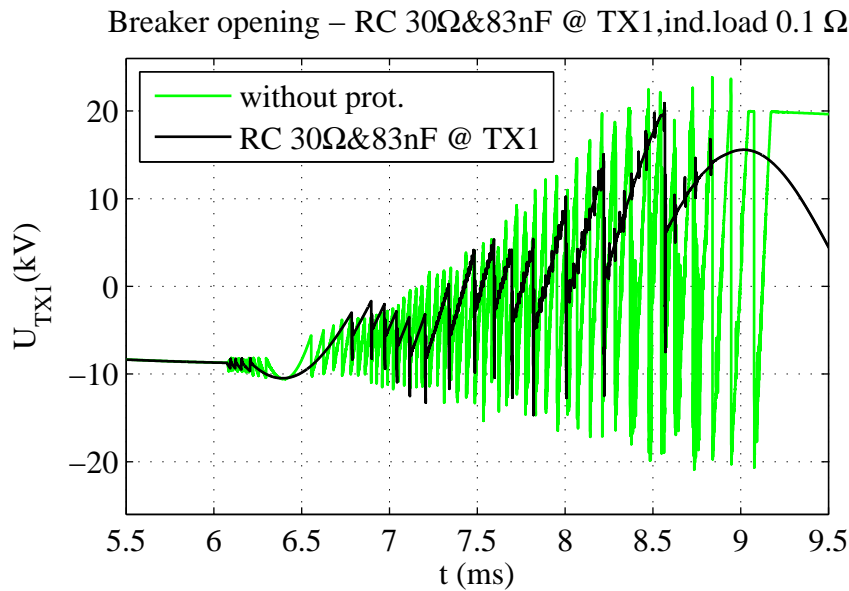


Figure 4.76: Impact of RC protection on transient voltage ($R30\Omega\&C83nF$) - simulation

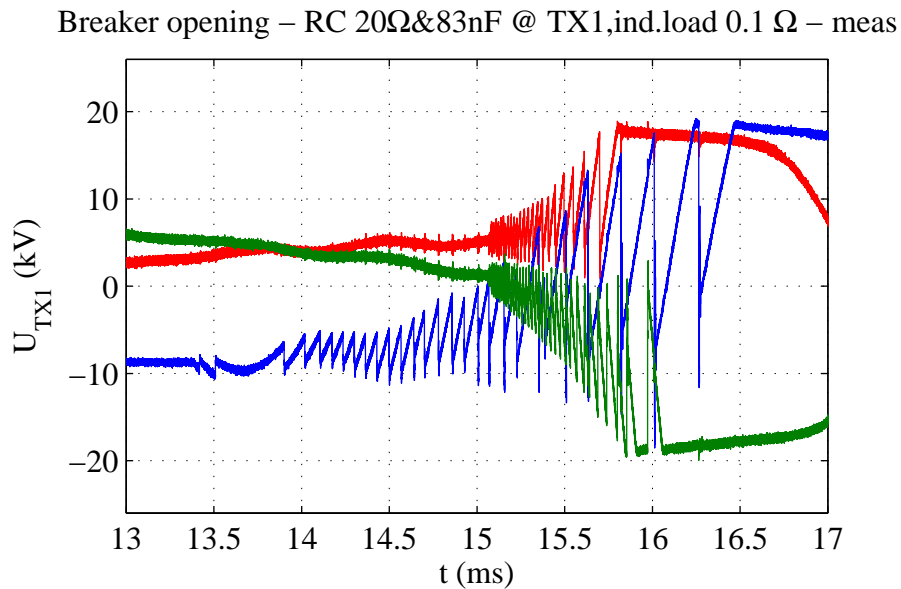


Figure 4.77: Transient voltage during opening - RC ($R20\Omega\&C83nF$) - measurement

The transient voltage response looks very similar when the simulation and the measurement are compared. The magnitudes of the recorded strikes in the simulation and the measurement are the same as well as the rise times. This can be observed in plot where a very narrow time interval of the voltage at transformer is shown. This can be seen in Fig. 4.79

The initial slope of the voltage surge is identical in the simulations and the measurements. In both cases, the high frequency oscillations are completely damped after 1 – 1.5 periods. This oscillation is caused by the wave reflection from the transformer TX2 and cannot be avoided. As mentioned before, the wave propagation speed is slightly higher in the simulations and the reflected wave arrives slightly before the wave recorded in measurements.

Breaker opening – RC 20Ω & $83nF$ @ TX1, ind. load 0.1Ω – sim.

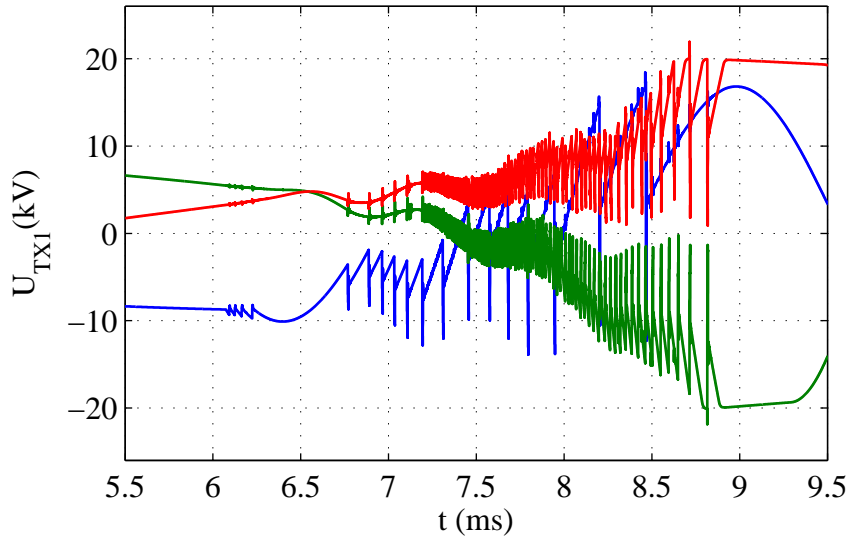


Figure 4.78: Transient voltage during opening - RC ($R20\Omega$ & $C83nF$) - simulation

RC 20Ω & $83nF$ @TX1 – comparison

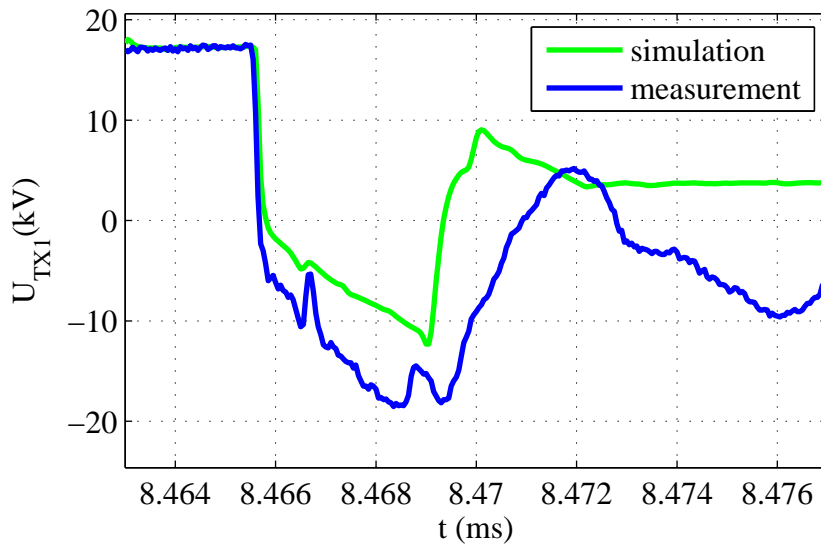


Figure 4.79: Simulation and measurement comparison ($R20\Omega$ & $C83nF$)

The scatter plot presented in Fig. 4.80 shows that most of the voltage strikes have the rise time of $2.5\mu s$ where the magnitude is kept below $2.6pu$.

This is a significant improvement over the base case, but a slightly better result is achieved when surge capacitors are used. However, all recorded surges are kept at the level well below BIL, both during the measurements and simulations.

For the case of an RC protection with an increased capacitance of $130nF$ it is expected that the rise time of the voltage strikes is increased even more. This is observed in Figs. 4.81 and 4.82.

A closer look at the voltage strike with the highest magnitude reveals that the simulated strike matches quite well to one recorded during the measurement, which can be seen in

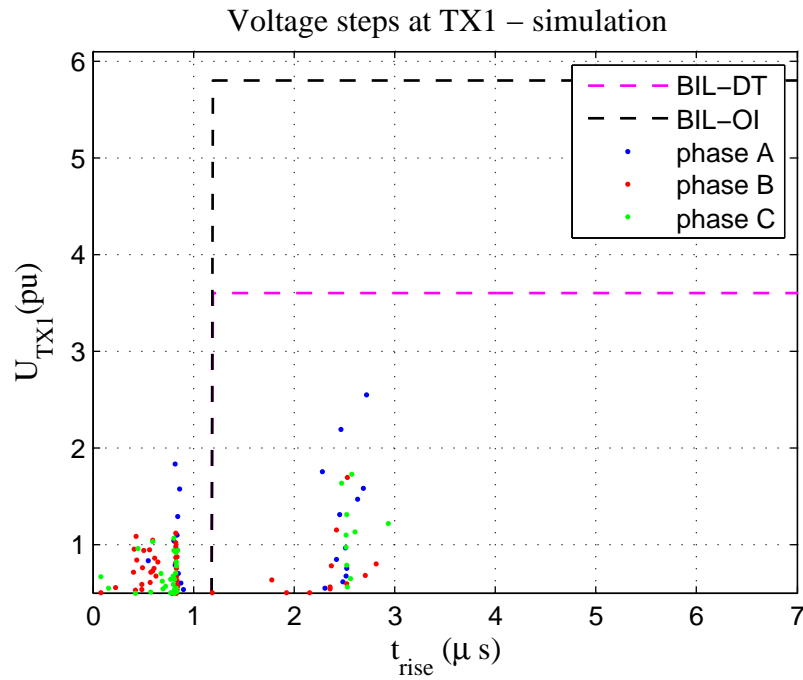


Figure 4.80: Voltage strikes $R20\Omega\&C83nF$ - simulation

Breaker opening – RC $20\Omega\&130nF$ @ TX1, ind. load $0.1\ \Omega$ – meas.

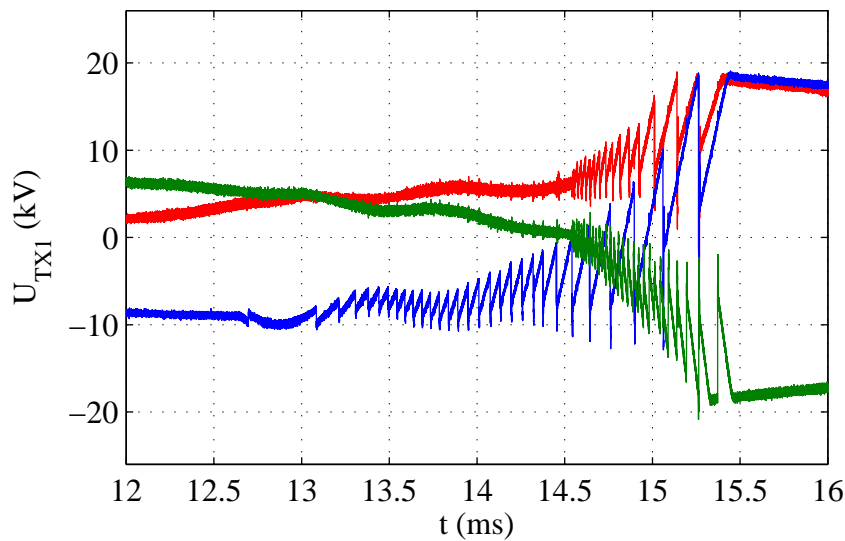


Figure 4.81: Transient voltage during opening - RC ($R20\Omega\&C130nF$) - measurement

Fig. 4.83. The high frequency oscillations seen in measurements do not show up in the simulations. These high frequency oscillations are caused by the voltage wave reflections from the bus where the breaker is connected and the transformer TX2.

A graph which shows the voltage strikes in a scatter plot is presented in Fig. 4.84. In this plot it can be seen that the magnitude of the voltage strikes is reduced while the rise time is kept on the same level as in the case with a $83nF$ capacitor. From the transient protection perspective, both cases are equally good since both manage to keep the magnitude of the voltage surges at the same level below BIL.

Breaker opening – RC 20Ω&130nF @ TX1,ind.load 0.1 Ω – sim.

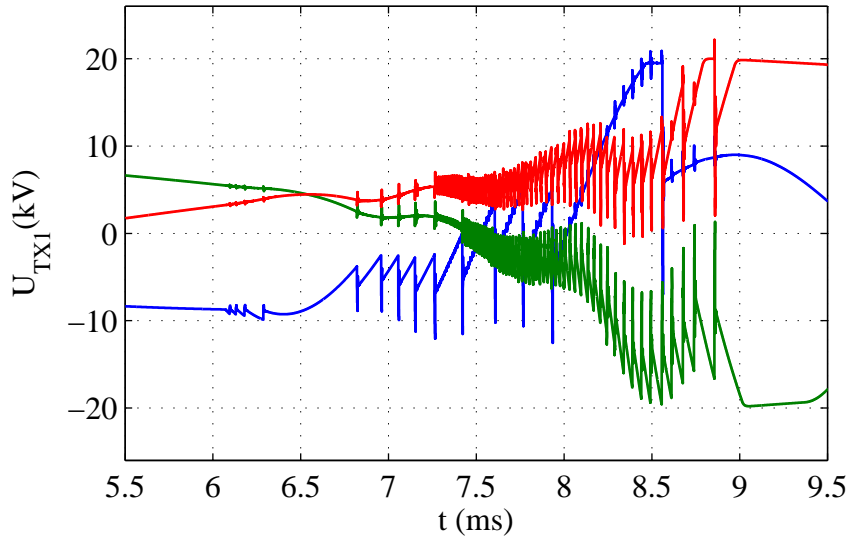


Figure 4.82: Transient voltage during opening - RC ($R20\Omega$ & $C130nF$) - simulation

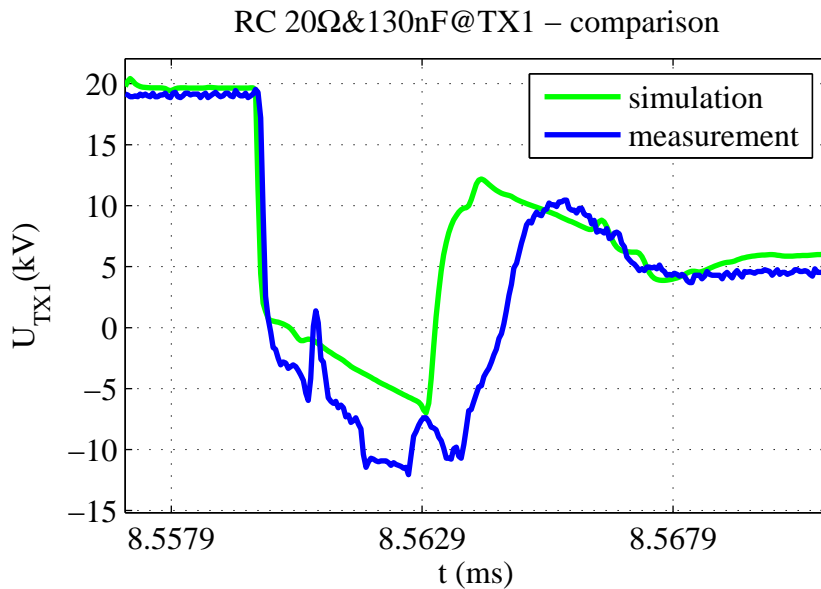


Figure 4.83: Simulation and measurement comparison ($R20\Omega$ & $C130nF$)

In the third case of the RC protection, the resistance is increased to 30Ω . This is not exactly the value of the cable surge impedance as two previous cases with RC protection, but it is expected that the damping in the system is improved due to presence of additional resistance.

The voltage transient recorded at transformer TX1 during the measurement and the simulation, is presented in Figs. 4.85 and 4.86.

A zoom of the transient where the simulation is compared to the measurement during a shorter time window where the surge of the highest magnitude is captured, is presented in Fig. 4.87.

In Fig. 4.87 it can be observed that stronger oscillations due to the voltage wave reflec-

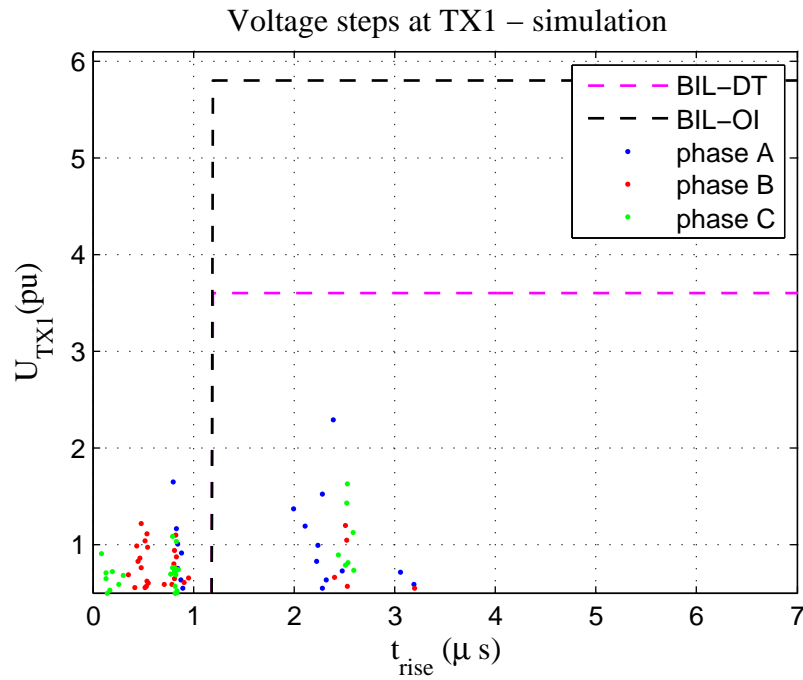


Figure 4.84: Voltage strikes $R20\Omega$ & $C130nF$ - simulation

Breaker opening – RC 30Ω & $83nF$ @ TX1, ind. load $0.1\ \Omega$ – meas.

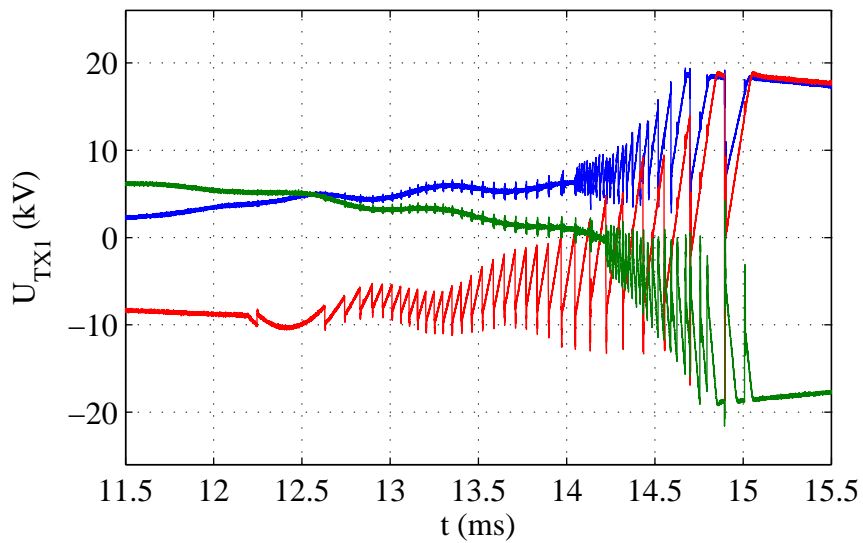


Figure 4.85: Transient voltage during opening - RC ($R30\Omega$ & $C83nF$) - measurement

tions are present both in the simulation and in the measurement, because the wave reflection coefficient is higher due to the higher resistance in this case.

The scatter plot reveals that the magnitude and the rise times of the strikes are similar to the case with a 20Ω resistor. This is presented in Fig. 4.88.

Although the magnitude of the reflected waves is increased in this case, the magnitude of the voltage surges is almost the same as in other cases of RC protection. The highest magnitude of the recorded surge is about $2.6pu$ with the rise time of $2.5\mu s$. This is well below the BIL set by standards for both dry-type and oil insulated transformers.

Breaker opening – RC 30Ω & $83nF$ @ TX1,ind.load $0.1\ \Omega$ – sim.

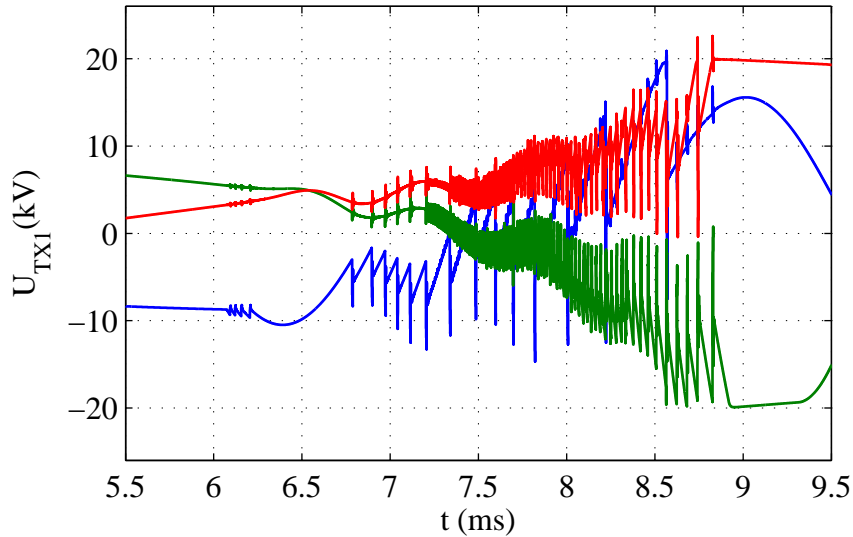


Figure 4.86: Transient voltage during opening - RC ($R30\Omega$ & $C83nF$) - simulation

RC 30Ω & $83nF$ @TX1 – comparison

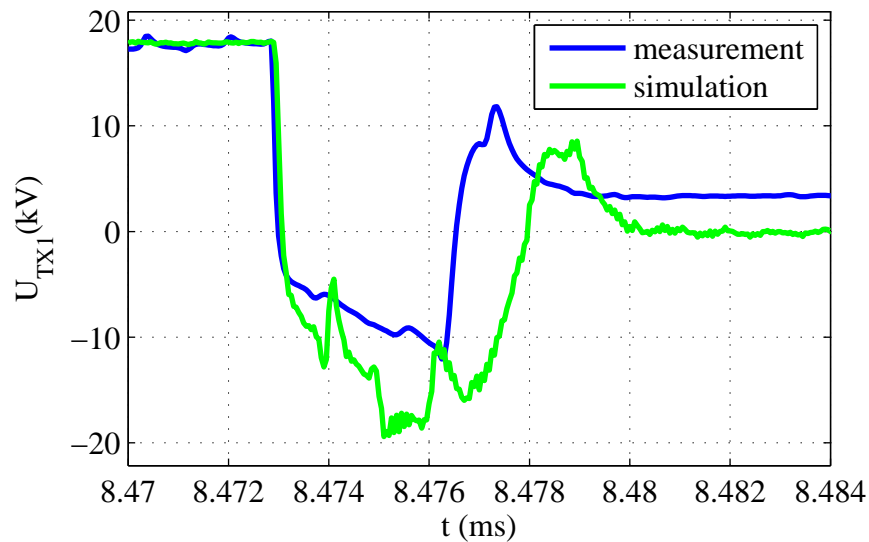


Figure 4.87: Simulation and measurement comparison ($R30\Omega$ & $C83nF$)

RC and surge capacitor protection

In order to decrease the magnitude of the voltage strikes even further and to protect transformer TX2, a $130nF$ surge capacitor is connected to the terminals of transformer TX2. Transformer TX1 is protected as in the first case of the RC protection with a 30Ω resistor and a $83nF$ capacitor. The aim is to even further slow down the transient recovery voltage and to reduce the rise time of the transients reflected from TX2 transformer. The scheme showing this setup is presented in Fig. 4.89

The simulation results showing the impact of the protection installed at two critical points is presented in Fig. 4.90.

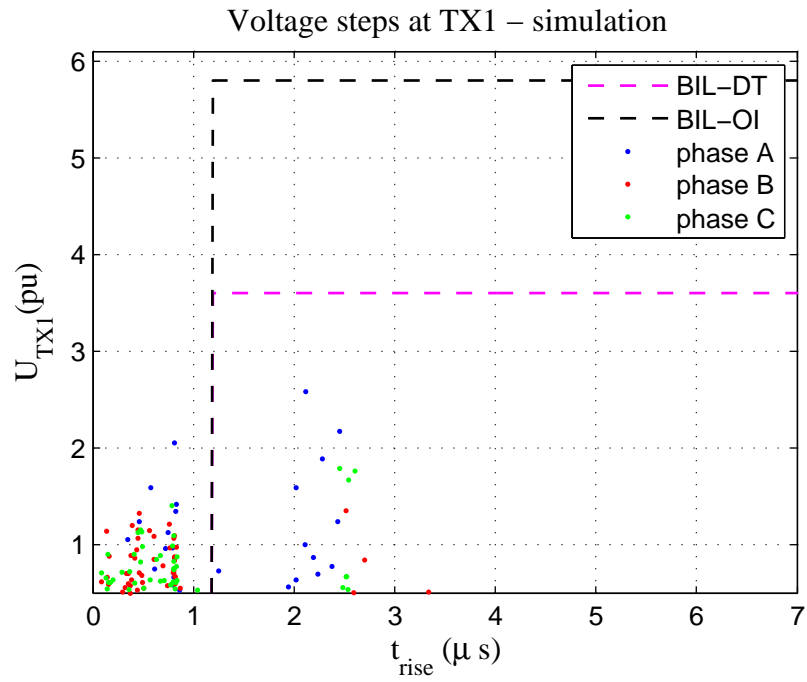


Figure 4.88: Voltage strikes $R30\Omega$ & $C83nF$ - simulation

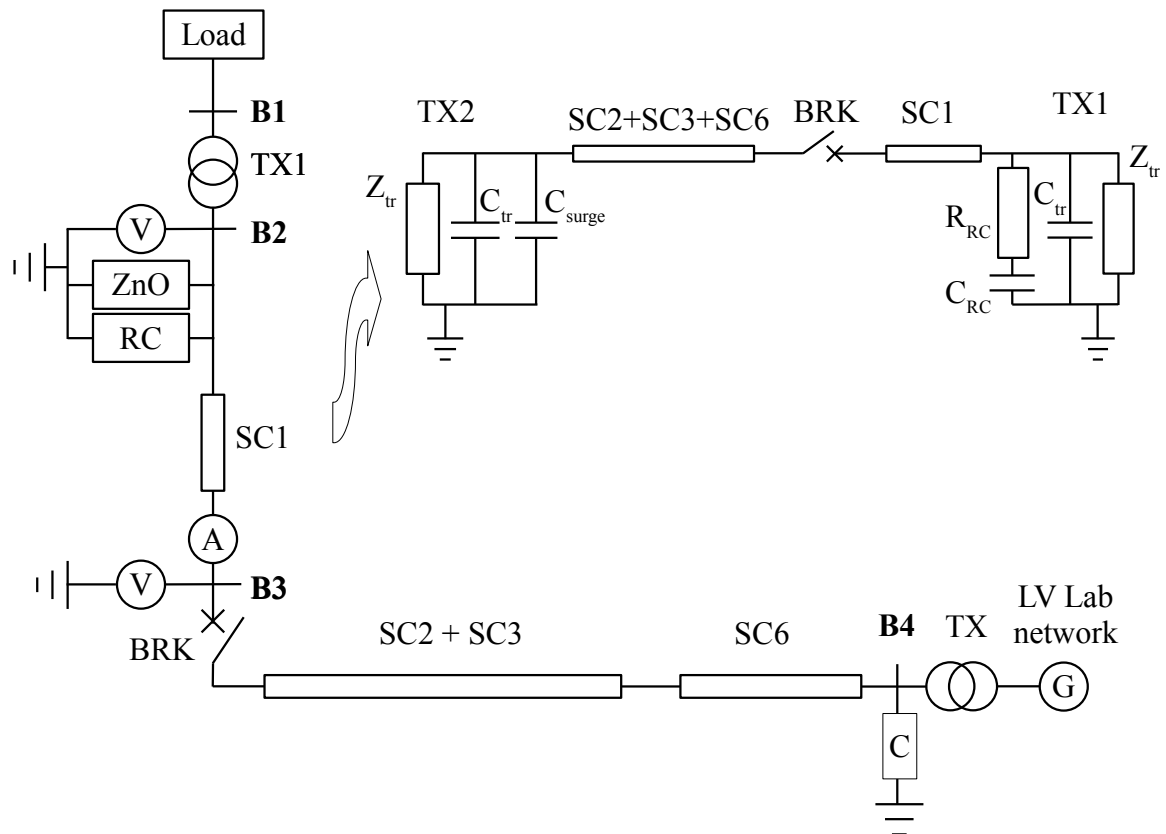


Figure 4.89: RC and surge capacitor protection

RC 30Ω & $83nF$ @TX1, cap. $130nF$ @TX2, ind.load $0.1\ \Omega$ – sim.

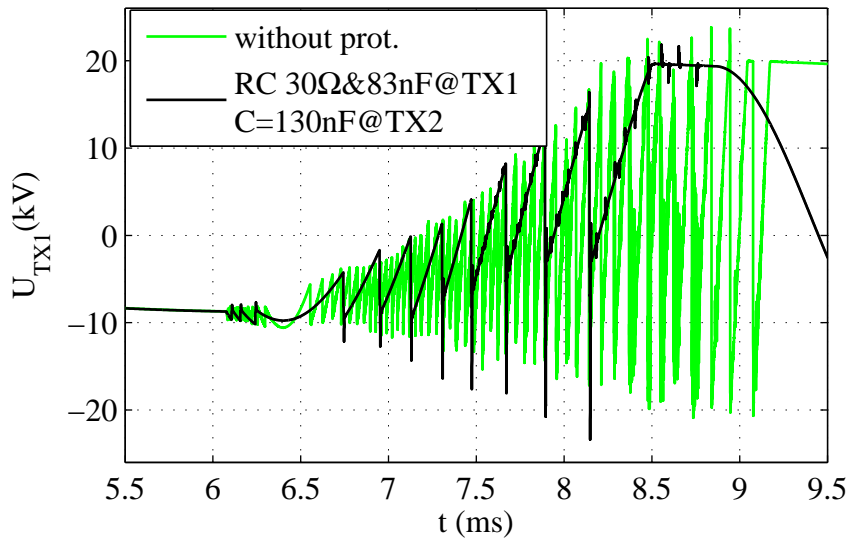


Figure 4.90: Impact of RC and surge capacitor protection ($R30\Omega$ & $C83nF$ $C130nF$) - simulation

Fig. 4.90 reveals that the magnitude of the strikes is increased when compared to the case when only RC protection is used. The explanation can be found when Fig. 4.91 is observed.

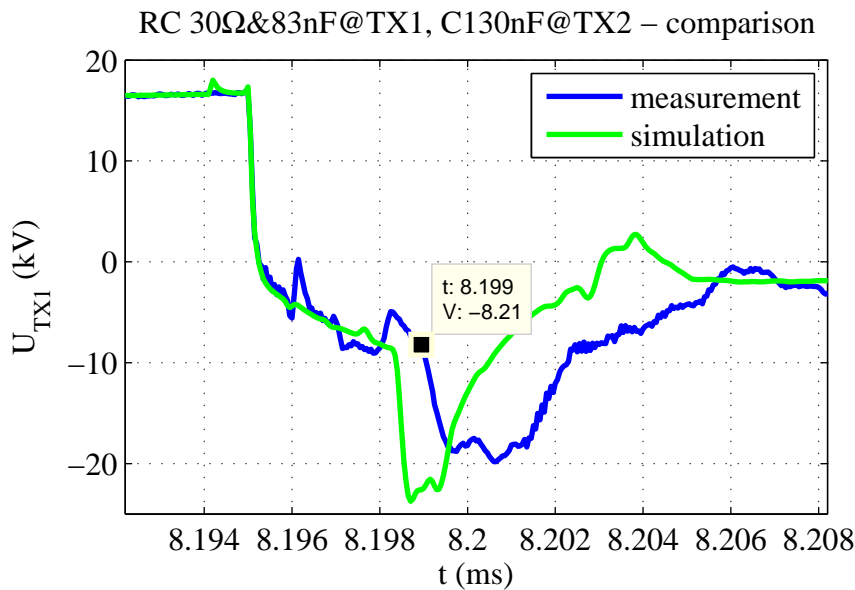


Figure 4.91: Simulation and measurement comparison $R30\Omega$ & $C83nF$ and $C130nF$

The reason for increased magnitude of surges is that at the time instant when the voltage strike is at its minimum, the reflected voltage from the TX2 transformer arrives to TX1 at $t = 8.199ms$ increasing the magnitude of the strike. The reflected voltage is inverted at TX2 due to the presence of the surge capacitor at terminals of transformer TX2. This phenomenon is avoided in the case with only RC protection at TX1 is used. This can be observed in Fig. 4.91.

The scatter plots show clearly the increase of the magnitude of the voltage strikes with

slightly increased rise times as seen in Fig. 4.92.

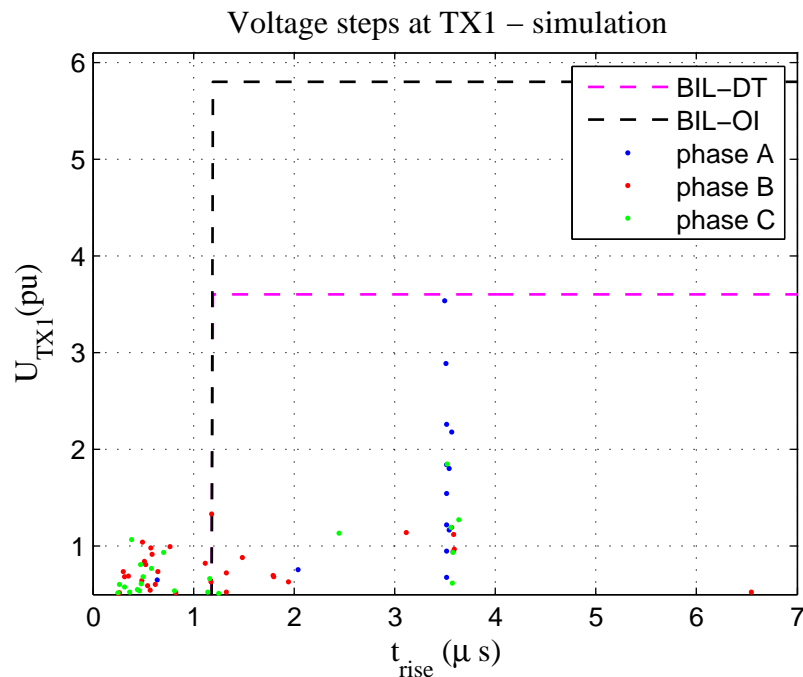


Figure 4.92: Voltage strikes $R30\Omega$ & $C83nF$ and $C130nF$ - simulation

In Fig. 4.92 it can be observed that the magnitudes of the surges almost reach the BIL defined by IEEE standards for the dry-type transformers. This means, that this protection scheme provides marginal protection of transformer TX1 because the wave reflected back from transformer TX2 arrives at TX1 producing high magnitude surges. This means that the length of the cables, and the wave propagation speed should be considered when a surge protection scheme is designed.

This case clearly shows that the high frequency mitigation protection should be carefully calculated and set up. When the additional protection is added to the system in order to improve the high frequency transient mitigation, the final result may be even worse when compared to a simple protection scheme.

Chapter 5

Conclusions and Future Work

In this thesis, the high frequency electromagnetic transient phenomenon is analyzed and studied. Modeling of various components needed for simulations such as transformers, cables and breakers for such a study is conducted. Furthermore, measurements of the high frequency transients are performed in the cable laboratory in ABB Corporate Research in Västerås, Sweden. The measurements are used for the parameter estimation of the models and for the simulation verification. Cases where surges of the magnitude and/or rise time above the basic lightning impulse voltage level appear are identified. Also, some transient protection schemes are studied and the performance of different transient mitigation devices is analyzed.

5.1 Conclusions

In this study, it is observed that:

- The frequency dependent cable model available in PSCAD/EMTDC provides a good basis for the high frequency transient phenomenon study if the electrical parameters of the insulation layers are recalculated to compensate for the semi-conducting layers. Since the cable geometry available in PSCAD/EMTDC does not allow for the modeling of the multi-pipe cables, the propagation speed of the surge is somewhat quicker when compared to the measurements;
- To obtain an accurate transformer model for frequencies up to a couple of kHz , the frequency dependency of resistances in the transformer have to be accounted. The existing transformer model in PSCAD/EMTDC based on the UMEC algorithm that accounts accurately for the core non-linearities with added Foster network of R and L components to model the frequency dependent resistance can be used for accurate simulations of transients in that frequency range;
- For the high-frequency transient analysis, stray capacitances are dominant in the transformer response and an accurate model can be obtained when stray capacitances of the transformer are accurately estimated and added to the existing PSCAD/EMTDC model. Such a model simulated the voltage surges with accurately calculated magnitudes and rise times. However, it shows a poor damping of the high frequency

oscillations caused by the capacitive coupling of the phases and needs to be improved for more accurate simulations;

- Simulation of the energizing transients show good agreement in the magnitude and the frequency of the transient voltages and currents;
- The high frequency transient simulations showed very good agreement with the measurements obtained in the cable lab. Differences are observed in the wave propagation speed due to the inability to model the multi-pipe cable in PSCAD/EMTDC. Furthermore, the use of the simplified transformer model showed a difference in damping of oscillations induced by the capacitive coupling. However, the magnitudes and the rise times of the critical surges are accurately simulated;
- During the simulations and the measurements, surges which exceed the BIL of dry-type transformers specified by IEEE standards, both in magnitude and rise time are recorded even when surge arresters are used;
- For the specific breaker used in the test, transient mitigation devices used in the tests did not prevent the appearance of repetitive surges and voltage escalations due to a low rate of rise of the dielectric withstand of the breaker. Among the mitigation methods tested in this study (Section 4.2), it is observed that surge capacitor protection coupled with surge arresters performed the best.

5.2 Future Work

Analysis showed that the existing models of the cable and the transformer can be improved. Therefore, the modeling of the cable can be improved using the cable model developed in FEM where frequency dependent impedance and admittance matrices of the cable are obtained. The estimation of the electric and magnetic properties of the insulating materials used in the cable can be obtained by measurements in order to obtain better accuracy. Furthermore, it would be of a great interest to obtain a more accurate transformer model of the dry-type transformer by modeling of the internal windings. Using such a model, internal transient overvoltages can be detected in the case of single and multiple surges. Also, other protection schemes with other transient mitigation devices can be tested and studied in order to obtain a good and cost effective transient mitigation solution.

Bibliography

- [1] Erik Persson, "Transient Effect in Application of PWM Inverters to Induction Motors," *IEEE Trans. Ind. Appl.*, vol. 28, no. 5, pp. 1095-1101, Sep./Oct. 1992.
- [2] S.M.Wong, L.A.Snider, E.W.C.Lo, "Overvoltages and reignition behavior of vacuum circuit breaker," *International Conference on Power Systems Transients - IPST 2003 in New Orleans, USA*, 2003.
- [3] P.Picot, "Vacuum switching," *Cahier technique Schneider Electric*, no. 198, pp. 4, March 2000.
- [4] D.J.Clare, "Failures of encapsulated transformers for converter winders at Oryx Mine," *Electron Magazine*, pp. 24-27, March. 1991.
- [5] D. Paul, "Failure Analysis of Dry-Type Power Transformer," *IEEE Transaction on Industry Applications*, Vol. 37 No. 3, May-June 2001
- [6] CIGRE working group A2-A3-B3.21, "Electrical Environment of Transformers; Impact of fast transients," *ELECTRA* 208, February 2005
- [7] W. H. Bartley, "An Analysis of Transformer Failures, Part 2 - Causes, Prevention and Maximum Service Life," *The Locomotive, The Full Story*, 1997
- [8] A. Mazur, I. Kerszenbaum, and J. Frank, "Maximum insulation stresses under transient voltages in the HV barrel type winding of distribution and power transformers," *IEEE Trans. Ind. Applicat.*, Vol. 24, pp. 427-433, May-June 1988.
- [9] W. Sweet, "Danish wind turbines take unfortunate turn," *Spectrum, IEEE*, vol. 41, Issue 11, pp. 30-34, Nov. 2004.
- [10] J.Larssen, H.Soerensen, E.Christiansen, S. Naef,P.Völund "Experiences from Middelgrunden 40 MW Offshore Wind Farm," *Copenhagen Offshore Wind* , 26-28 Oct. 2005.
- [11] B. K. Gupta, N. E. Nilsson, D. K. Sharma "Protection of Motors Against High Voltage Switching Surges," *IEEE Trans. on Energy Conversion*, Vol. 7 No. 1, March 1992
- [12] Turn Insulation Capability of Large AC Motors, EPRI Project RP 2307-1, *Final Report, EPRI EL-5862*, Vol. 1 and 2, July 1988
- [13] B. K. Gupta, B. A. Loyd, S. R. Campbell, D. K. Sharma, N. E. Nilsson "Turn Insulation Capability of Large AC Motors, Part 1/Surge Monitoring," *IEEE Trans. on Energy Conversion*, EC-2 No. 4, December 1987, pp 658-665.

- [14] B.K. Gupta, B.A.Lloyd, D.K. Sharma "Degradation of Turn Insulation in Motor coils Under Repetitive Surges," *IEEE Trans. on Energi Conv.*, Vol.5 No. 2, June 1990
- [15] G.C. Stone, R.G. Van Heeswijk, R. Bartnikas "Investigation of The Effect of Repetitive Voltage Surges on Epoxy Insulation," *IEEE Trans. on Energy Conv.*, Vol. 7 No. 4 December 1992
- [16] Eichenberg J.P, Hennenfent H., Ljiljestrand L., "Multiple Re-Strikes Phenomenon when Using Vacuum Circuit Breakers to Start Refiner Motors," *Pulp & Paper Canada* vol. 98, no. 7, pp. 32-36, July 1997.
- [17] M.P.Reece, "A review of the development of the vacuum interrupter," *Phil.Trans.R.Soc.Lond.A.* vol.275, no. 1248, pp. 121-129, Aug. 1973.
- [18] R. Kirkland Smith, "Vacuum Interrupters Have the Low Environmental Impact Required for Today's Medium Voltage Switching Applications," *IEEE PES Transmission and Distribution Conference and Exposition*, vol.1, pp. 588-592 , 2001
- [19] Paul G. Slade, "Growth of Vacuum Interrupter Application in Distribution Switchgear," *Trends in Distribution Switchgear*, Conference Publication no. 459, November 1998
- [20] Alexey M. Chaly, Alevtina T. Chalaya, Irina N. Poluyanova, Victor N. Poluyanov "The Features of 0.4 kV motor interruption by a vacuum contactor with different contact materials," *Discharges and Electrical Insulation in Vacuum, Proceedings ISDEIV. XVIIIth International Symposium*, vol. 2, pp. 435-438, Aug. 1998.
- [21] Smeets R.P.P., van der Wen W.J., Wartanabe K., "Vacuum Arc Lifetime extension at Small Gaplength: Beneficial for Low-Surge Circuit Interruption," *International Conference on Gas Discharges and Their Applications*, Tokyo, 1995.
- [22] Reininghaus U., "Schalverhalten Unterschiedlicher Kontaktwerkstoffe in Vacuum," Ph.D. Thesis, TU Braunschweig, 1983.
- [23] Smeets R.P.P., "Low current behavior and Current Chopping of Vacuum Arcs," Ph.D. Thesis, University of Eindhoven, 1987.
- [24] J. Helmer, M. Lindmayer "Mathematical Modeling of the High fiequency Behavior of Vacuum Interrupters and Comparison with Measured Transients in Power Systems," *XVIIth International Symposium on Discharges and Electrical Insulation in Vacuum*, pp. 1-9, July. 1996.
- [25] Popov M., "Switching Three-Phase Distributions Transformer With a Vacuum Circuit Breaker - Analysis of Overvoltages and the Protection Equipment," Ph.D. Thesis, Delft University of Technology, 2002.
- [26] M. Glinkowski, "Voltage Escalation and Reignition Behavior of Vacuum Generator Circuit Breakers During Load Shedding", *IEEE Trans. on Power Delivery*, Vol. 12, No. 1, pp.219-226, Jan. 1997.
- [27] S.M.Wong, L.A.Snider, and E.W.C.Lo Overvoltages and reignition behavior of vacuum circuit breaker, *6th International Conference on Advances in Power System Control, Operation and Management. Proceedings. APSCOM Hong-Kong*, pp.653-658, Nov. 2003.

- [28] Y.H. Fu. and G.C. Damstra , N.V. KEMA, Arnhem,
 "Switching Transients During Energizing Capacitive Load by a Vacuum Circuit Breaker," *IEEE Transactions on Electrical Insulation*, Vol. 28 No. 4, pp. 657-666, August 1993.
- [29] Lars Liljestr and, Ambra Sannino, Henrik Breder, Stefan Johansson Transients in Collection Grids of Large Offshore Wind Parks, *Nordic Wind Power Conference*, Espoo Finland, May, 2006.
- [30] J. A. Martinez, B. Gustavsen, and D. Durbak Parameter Determination for Modeling System Transients - Part I: Overhead Lines, *IEEE Trans. on Power Delivery*, Vol. 20 No. 3, pp. 2038-2044, July 2005.
- [31] Marti, L. "Simulation of transients in underground cables with frequency-dependent modal transformation matrices," *IEEE Trans. on Power Delivery*, Vol.3 No.3, pp. 1099-1110, July 1988.
- [32] Marti, J. R. "Accurate Modelling of Frequency-Dependent Transmission Lines in Electromagnetic Transient Calculations," *IEEE Transactions on Power Apparatus and Systems*, pp. 147-157, January 1982.
- [33] H.V. Nguyen, H.W. Dommel, J.R. Marti "Direct Phase-Domain Modelling of Frequency-Dependent Overhead Transmission lines," *IEEE Trans. on Power Delivery*, Vol. 12 No. 3 July 1997
- [34] Semlyen, A. Dabuleanu, A. "Fast and accurate switching transient calculations on transmission lines with ground return using recursive convolutions," *Power Apparatus and Systems, IEEE Transactions on*, Vol. 94 Issue 2 pp. 561- 571 March 1975
- [35] Gustavsen, B. Semlyen, A. "Rational approximation of frequency domain responses by vector fitting," *Power Delivery, IEEE Transactions on*, Vol.14 No.3 pp.1052-1061 July 1999
- [36] Gustavsen, B. Semlyen, A. "Simulation of transmission line transients using vector fitting and modal decomposition," *Power Delivery, IEEE Transactions on*, Vol.13 No.2 pp.605-614 April 1998
- [37] Fergestad, P.I. Henriksen, T. "Transient Oscillations in Multiwinding Transformers," *IEEE Transactions on Power Apparatus and Systems*, Vol.PAS-93 No.2 pp.500-509 March 1974
- [38] Guardado, J.L. Carrillo, V. Cornick, K.J. "Calculation of interturn voltages in machine windings during switching transients measured on terminals," *Energy Conversion, IEEE Transaction on*, Vol.10 No.1 pp.87-94 Mar 1995
- [39] Shibuya, Y. Fujita, S. Hosokawa, N. "Analysis of very fast transient overvoltage in transformer winding" *Generation, Transmission and Distribution, IEEE Proceedings-*, Vol.144 No.5 pp.461-468 Sep 1997
- [40] Soysal, O.A., "Voltage stresses in a distribution transformer under nonideal switching conditions," *Power Engineering Society 1999 Winter Meeting, IEEE*, Vol.2 No. pp. 1031-1035 Feb 1999

- [41] Alexander D. Podoltsev, K. G. Nilanga B. Abeywickrama, Yuriy V. Serdyuk, Stanislaw M. Gubanski "Multiscale Computations of Parameters of Power Transformer Windings at High Frequencies. Part I: Small-Scale Level," *IEEE Transactions on magnetics*, Vol. 43, No. 11, November 2007
- [42] Soysal, O. A. "A Method for Wide Frequency Range Modeling of Power Transformers and Rotating Machines," *IEEE Trans. on Power Delivery*, Vol. 8 No. 4 pp. 1802-1810 October 1993
- [43] P. T. M. Vaessen, "Transformer model for high frequencies" *IEEE Trans. Power Delivery*, Vol. 3, pp. 1761-1768, Oct. 1988
- [44] Q. Su, R. E. James, and D. Sutanto "A z-transform model of transformers for the study of electromagnetic transients in power systems," *IEEE Trans Power Systems*, Vol. 5, pp. 27-33, Feb. 1990
- [45] A. Morched, L. Marti, and J. Ottevangers "A high frequency transformer model for the EMTP," *IEEE Trans. on Power Delivery*, Vol. 8, pp. 1615-1626, July 1993
- [46] Gustavsen, B. "Wide band modeling of power transformers," *IEEE Trans. on Power Delivery*, Vol.19 No.1, pp. 414-422, Jan. 2004
- [47] Gustavsen, B. "Computer code for rational approximation of frequency dependent admittance matrices," *Power Delivery, IEEE Transactions on*, Vol. 17 No.4 pp. 1093-1098, Oct 2002
- [48] Gustavsen, B. Semlyen, A. "Application of vector fitting to state equation representation of transformers for simulation of electromagnetic transients," *Power Delivery, IEEE Transactions on*, Vol.13 No.3 pp.834-842, Jul 1998
- [49] Manitoba HVDC Research Centre Inc. *EMTDC User's Guide*, Manitoba HVDC Research Centre Inc. 2005
- [50] W. Enright, O.B. Nayak, G.D. Irwin, A. Arrillaga "An Electromagnetic Transients Model of Multi-Limb Transformer Using Normalized Core Concept," *IPST'97 - International Conference on Power System Transients*, pp.93-98 June 1997
- [51] W. Enright, N. Waston and O.B. Nayak, "Three Phase five-Limb Unified Magnetic Equivalent Circuit Transformer Models for PSCAD V3," *IPST'99 - International Conference on Power System Transients*, pp.462-467 July, 1999
- [52] J. Arrillaga, W. Enright, N. Watson and A. Wood, "Improved Simulation of HVDC Converter Transformers in Electromagnetic Transient Programs," *IEEE Proc. - Generation, Transmission and Distribution*, Vol. 144 No.2 pp.100-106. March 1997
- [53] Das, J.C. "Surges transferred through transformers," *Pulp and Paper Industry Technical Conference, 2002. Conference Record of the 2002 Annual*, No. pp.139-147, 2002
- [54] L. Liljestr and, A. Sannino, H. Breder, S. Thorburn "Transients in collection grids of large offshore wind parks," *Wind Energy*, Vol. 11 No. 1 pp.45-61, 2008
- [55] R. B. Lastra, M. Barbieri, "Fast Transients in the Operation of an Induction Motor with Vacuum Switches," *Int. Conf. on Power Systems Transients IPST'2001*, 24-28 June 2001, Rio de Janeiro (Brasil), paper 063

- [56] P. Chowdhuri, *Electromagnetics Transients in Power Systems*, Research Studies Press, England, 1996.
- [57] A. Greenwood, *Electrical Transients in Power Systems*, Wiley, New York, 1991
- [58] J. H. Harlow *Electric Power Transformer Engineering*, CRC Press, 2004.
- [59] "IEEE standard test code for dry-type distribution and power transformers," *IEEE Std C57.12.91-2001*, 2001
- [60] "IEEE Standard Requirements for Liquid-Immersed Distribution Substation Transformers," *IEEE Std C57.12.36-2007*, pp.c1-29, March, 2008
- [61] Muhamad Reza, Henrik Breder *Cable System Transient Study - Vindforsk V-110. - Experiments with switching transients and their mitigation in a windpower collection grid scale model*, Vindforsk, Sweden, January, 2009
- [62] R. L. Doughty, F. Heredos, "Cost effective motor surge capability," *in Proc. Petroleum and Chemical Industry Conference, 1995. Record of Conference Papers., Industry Applications Society 42nd Annual*, pp.91-103.
- [63] D. C. Bacvarov, D. W. Jackson, C. L. Lee, "Effect of Surge Capacitor Lead Length on Protection of Motors from Steep Switching Surges," *IEEE Transactions on Power Apparatus and Systems*, vol.PAS-103, no.7, pp.1879-1882, July 1984.
- [64] Popov, M.; van der Sluis, L.; Paap, G.C., "A simplified transformer model for the simulation of fast surges and adequate protection measures," *Power Engineering Society Winter Meeting, 2001. IEEE*, vol.1, no., pp.323-328 vol.1, 28 Jan-1 Feb 2001.